





Ex LIBRIS  
UNIVERSITATIS  
ALBERTAENSIS











Digitized by the Internet Archive  
in 2022 with funding from  
University of Alberta Libraries

<https://archive.org/details/Jurak1972>



THE UNIVERSITY OF ALBERTA

FACULTY OF GRADUATE STUDIES AND RESEARCH

COAXIAL PLASMA ACCELERATOR STUDY

by



KAREL JURAK

A THESIS

SUBMITTED TO THE FACULTY OF GRADUATE STUDIES AND RESEARCH  
IN PARTIAL FULFILMENT OF THE REQUIREMENTS FOR THE DEGREE  
OF DOCTOR OF PHILOSOPHY

DEPARTMENT OF ELECTRICAL ENGINEERING

EDMONTON, ALBERTA

FALL, 1972





Thesis

72F-51D

THE UNIVERSITY OF ALBERTA  
FACULTY OF GRADUATE STUDIES AND RESEARCH

The undersigned certify that they have read, and recommend to the Faculty of Graduate Studies and Research, for acceptance, a thesis entitled "Coaxial Plasma Accelerator Study" submitted by Karel Jurak in partial fulfilment of the requirements for the degree of Doctor of Philosophy.



## COAXIAL PLASMA ACCELERATOR STUDY

## ABSTRACT

This study gives an up-to-date review of the coaxial plasma accelerator - introducing regimes, models of regimes, and types of accelerators. The theoretical investigation is devoted to the axisymmetric-steady-shock-tube model and related numerical procedures are developed and verified. The experimental effort is in the accelerator with a teflon dielectric. Circuitry for an original version of a unipolar pulsed plasma accelerator has been developed as a part of this study.





## ACKNOWLEDGEMENTS

The author wishes to express his appreciation to Professors A.A. Offenberger, G.J. Pert, and P.R. Smy for their guidance in this research. In addition to the above, the author would like to thank Mr. D. Way-Nee for his assistance with the infrared diagnostics.

The author is indebted to the National Research Council of Canada and the University of Alberta for financial support.



## TABLE OF CONTENTS

ABSTRACT

ACKNOWLEDGEMENTS

TABLE OF CONTENTS

LIST OF ILLUSTRATIONS

CHAPTER I	INTRODUCTION	1
CHAPTER II	COAXIAL PLASMA ACCELERATOR (CPA)	6
2.1	TYPICAL CPA REGIMES	6
2.1.1	Discharge-initiation Regime	6
2.1.2	Shock-tube Regime	7
2.1.3	Plasmoid-acceleration Regime	8
2.1.4	Fast-plasmoid-creation Regime	8
2.1.5	Plasma-ejection Regime	9
2.1.6	Dense-plasma-focus Regime	9
2.1.7	Inertial-plasmoid-focus Regime	10
2.2	MODELS OF SOME CPA REGIMES	10
2.2.1	Discharge-initiation Model	10
2.2.2	Shock-tube Models	11
2.2.3	Plasmoid-acceleration Model	15
2.2.4	Current-sheet Model	20





2.3	BASIC PULSED-PLASMA-ACCELERATOR TYPES	23
2.3.1	Pulsed-gas Type	24
2.3.2	Dielectric-erosion Type	25
2.3.3	Electrode-erosion Type	25
2.3.4	Shock-tube Type	25
2.3.5	Static-gas-pressure Type	26
2.4	OTHER PHYSICAL PROCESSES	26
2.5	CONCLUSIONS	30
CHAPTER III	THEORETICAL DESCRIPTION OF THE SHOCK-TUBE REGIME	32
3.1	FORMULATION OF THE STEADY SHOCK-TUBE MODEL	32
3.2	EQUILIBRIUM CONDITIONS BEHIND A STEADY SHOCK WAVE	37
3.2.1	Calorically Ideal Gas	38
3.2.2	Monatomic Gas	39
3.3	TWO-DIMENSIONAL MODEL	42
3.4	QUASI-ONE-DIMENSIONAL MODEL	45
CHAPTER IV	NUMERICAL SOLUTION	48
4.1	LEAST-SQUARES SOLUTION OF THE TWO-DIMENSIONAL MODEL	50
4.1.1	Variational Formulation	53
4.1.2	Minimization to the Function of N-Variables	55
4.1.3	Results and Comparison	56
4.2	RUNGE-KUTTA SOLUTION TO THE QUASI-ONE-DIMENSIONAL MODEL	58
4.2.1	Initial Conditions	60
4.2.2	Results and Comparison	61



CHAPTER V	APPARATUS	69
5.1	MECHANICAL DESIGN OF THE ACCELERATOR	71
5.2	ELECTRICAL DESIGN OF THE ACCELERATOR	73
5.2.1	Circuit Analysis	74
5.2.2	Experimental Results	75
5.3	DIAGNOSTICS	78
5.3.1	Current and Voltage of the Discharge	78
5.3.2	Luminosity	79
5.3.3.	Current Distribution	81
5.3.4	Infrared Diagnostics	82
5.3.5	Spot-track-pattern	86
CHAPTER VI	RESULTS OF THE MEASUREMENTS	88
6.1	DISCHARGE-INITIATION REGIME	88
6.2	ACCELERATOR WITH INSULATOR I	90
6.2.1	Current Distribution	91
6.2.2	Current-front Position	93
6.2.3	Electron Density and Temperature	93
6.3	ACCELERATOR WITH INSULATOR II	96
6.3.1	Electrode Erosion	97
6.3.2	Current Distribution	100
6.3.3	Current-front Position	101
CHAPTER VII	RESUME AND CONCLUSIONS	102
LIST OF REFERENCES		104





## LIST OF ILLUSTRATIONS

Fig. 1.1	Coaxial plasma accelerator.	2
Fig. 2.1	Sketch of the linearized CPA.	17
Fig. 2.2	Types of solutions to plasmoid-acceleration model.	17
Fig. 2.3	Diagram of current sheet motion.	22
Fig. 2.4	Sketch of insulator ablation model.	22
Fig. 3.1	Sketch of part of a long CPA with the control volume.	34
Fig. 3.2	The control volume of steady shocked layer model.	34
Fig. 3.3	Sketch of the boundaries.	36
Fig. 3.4	Calculated number densities $n$ , $n_1$ , and $n_2$ behind a plane shock wave of velocity $v_0$ in helium of 1 Torr pressure.	36
Fig. 3.5	Calculated electron number density versus shock velocity.	40
Fig. 3.6	Calculated equilibrium temperature versus shock velocity.	40
Fig. 3.7	Diagram of the axisymmetric flow system showing the variables and notation used.	43
Fig. 4.1	Comparison of $u(s,y)$ calculated by LS-method with those calculated by Belotserkovskii <i>et al.</i> (1966).	43
Fig. 4.2	Comparison of $-v(s,y)$ calculated by LS-method with those calculated by Belotserkovskii <i>et al.</i> (1966).	43
Fig. 4.3	Comparison of $p(s,y)$ calculated by LS-method with those calculated by Belotserkovskii <i>et al.</i> (1966).	44
Fig. 4.4	Initial condition calculation; $\Delta(r_0 + \delta r)$ versus driving current.	57
Fig. 4.5	Ideal steady-state current sheet velocity versus driving current.	57



Fig. 4.6	Iterative improvement of the guess value.	62
Fig. 4.7	Calculated number density $n = n_{\text{He}} + n_{\text{He}^+} + n_{\text{He}^{++}}$ versus radius.	62
Fig. 4.8	Calculated number density $n_1 = n_{\text{He}^+}$ versus radius.	63
Fig. 4.9	Calculated number density $n_2 = n_{\text{He}^{++}}$ versus radius.	63
Fig. 4.10	Calculated equilibrium temperature $T$ versus radius.	64
Fig. 4.11	Calculated $z$ coordinate of the middle of the shocked layer versus radius.	64
Fig. 4.12	Calculated incidence angle $\theta$ of the middle of the shocked layer versus radius.	65
Fig. 4.13	Calculated shocked layer thickness versus radius.	65
Fig. 4.14	Calculated gas velocity along the current layer versus radius.	66
Fig. 4.15	Calculated and experimental electron densities.	67
Fig. 4.16	Calculated and experimental equilibrium temperature.	68
Fig. 5.1	Schematic layout of the CPA apparatus.	69
Fig. 5.2	Sketch of the mechanical set-up.	71
Fig. 5.3	Three versions of the CPA.	72
Fig. 5.4	Circuit diagram of the pulse generator for a unipolar pulsed plasma accelerator.	74
Fig. 5.5	Calculated $I_1$ and $U_{10}$ .	76
Fig. 5.6	Variation of currents $I_{M1}$ , $I_{M2}$ , and $I_{M3}$ with $Z_0/R_2$ .	77
Fig. 5.7	Oscillogram of the current $I_1$ and the voltage $U_{10}$ .	77
Fig. 5.8	Oscillogram of the currents $I_1$ and $I_{11}$ .	78
Fig. 5.9	Schematic and typical oscillogram of the current and high-voltage probe.	79





Fig. 5.10	Luminous layer position measurement.	80
Fig. 5.11	Luminous layer velocity measurement.	80
Fig. 5.12	Current sheet velocity measurement.	81
Fig. 5.13	Schematic and typical oscillograms of the differential magnetic probe.	82
Fig. 5.14	Mach-Zehnder interferometer arrangement.	84
Fig. 5.15	Evaluation of the interferogram for a linear electron density change.	84
Fig. 5.16	Schematic diagram of the Ge-Au detector.	84
Fig. 6.1	Schematic diagram of the apparatus for initial breakdown.	89
Fig. 6.2	Verification of the preionization circuit.	89
Fig. 6.3	Current distribution for CPA with Insulator I.	92
Fig. 6.4	Typical time development of the discharge current inside CPA with Insulator I.	92
Fig. 6.5	Current front position for CPA with Insulator I.	92
Fig. 6.6	Typical traces of the local current and fringe beats and electron density.	94
Fig. 6.7	Current and voltage measurements.	94
Fig. 6.8	Oscillograms of local current, detected ir continuum, and calculated electron temperature.	96
Fig. 6.9	Region definition sketch for static photography of the spot-tracks on the central electrode.	97
Fig. 6.10	Photographs of anode-spot tracks.	98
Fig. 6.11	Photographs of cathode-spot tracks.	98
Fig. 6.12	Current sheet distribution for CPA with Insulator II.	100
Fig. 6.13	Current front position of CPA with Insulator II.	101



## CHAPTER I INTRODUCTION

A coaxial plasma accelerator (CPA in the following text) illustrated in a very simplified version by Fig. 1.1 is one member of a large family of electromagnetic plasma accelerators. In those devices the acceleration of a body of ionized gas occurs by the interaction of currents driven through the gas with magnetic fields established either by those currents or by external means. For a more complete picture we may refer to Table 1 taken from Jahn and von Jaskowsky (1968). The subject investigated here is marked in the table, namely, we are going to deal with pulsed CPA having: static filling of helium, no external magnetic field, internal ionization (with small preionization), capacitor-bank type current source, direct coupling of discharge to circuit, pure gas and vaporized solid as the working fluid, coaxial channel geometry, and with external switch (see Fig. 1.1). From Table 1 it is also clear that many conclusions related to a CPA are correct also for a parallel rail plasma accelerator, and pinch devices, and vice versa. However, generalizations of this nature may be misleading.

Apart from the fact that accelerator phenomena are intrinsically interesting, there are some very practical reasons for studying them. First, in propulsion applications, this electromagnetic mechanism holds promise for providing a combination of high exhaust velocities with high mass flows, in comparison with pure electrothermal and electrostatic mechanisms. For example, a pulsed thruster is used for station-keeping in the LES-6



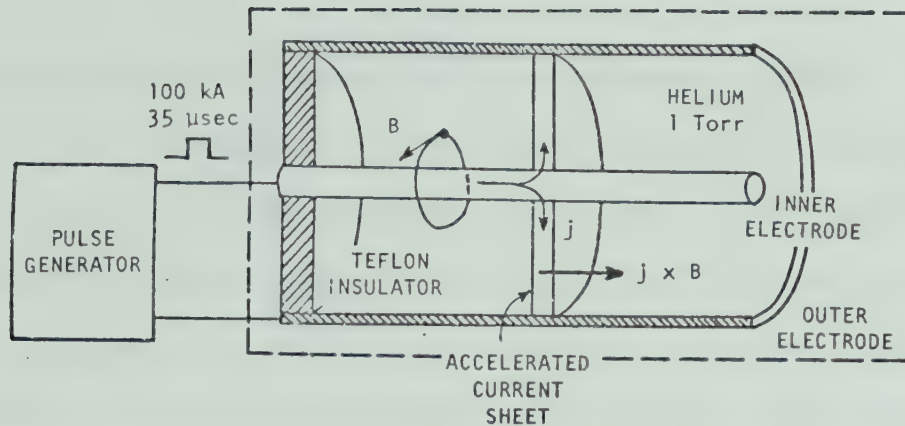


Fig.1.1 Coaxial plasma accelerator.

Table 1 Classification of electromagnetic accelerators

TIME SCALE OF INTERACTION	STEADY		PULSED		TRAVELING WAVE
SOURCE OF MAGNETIC FIELD	EXTERNAL COILS OR MAGNETS	SELF-INDUCED	SELF-INDUCED		COIL SEQUENCE OR TRANSMISSION LINE
IONIZATION	EXTERNAL	INTERNAL	INTERNAL		EXTERNAL OR INTERNAL
PRIMARY CURRENT SOURCE	DIRECT CURRENT SUPPLY		CAPACITOR BANK OR INDUCTIVE COILS		RADIO-FREQUENCY SUPPLY
DISCHARGE COUPLING TO CIRCUIT	DIRECT		DIRECT	INDUCTIVE	INDUCTIVE
WORKING FLUID	PURE OR SEEDED GAS		PURE GAS; VAPORIZED LIQUID OR SOLID	PURE GAS	PURE GAS
CHANNEL GEOMETRY	RECTANGULAR OR COAXIAL; CONSTANT OR VARIABLE CROSS-SECTION		COAXIAL, PINCH, PARALLEL RAIL, ABLATING PLUG	THETA PINCH, CONICAL PINCH, LOOP INDUCTOR	RECTANGULAR, CYLINDRICAL, COAXIAL; CONSTANT OR VARIABLE CROSS-SECTION
OTHER DISTINGUISHING FEATURES	LORENTZ OR HALL MODE		INTERNAL OR EXTERNAL SWITCH		CONSTANT OR VARIABLE PHASE VELOCITY





satellite (Vondra *et al.* 1970). These thrusters use an arc discharge across a teflon surface; the ablated molecules are then ionized and exhausted at 3000 m/s.

The second application area of CPA is in plasma injectors, that is production of fast and dense plasmoids. For such purposes the purity of the gas to be ionized and accelerated is important. This requires investigation of: gas-conditions in the experimental chamber, residual gas, fast gas valve operation, gas desorption from the walls and decomposition of heavy particles of oil vapors penetrating from the vacuum pumps, etc. (Gryzinski, 1968).

The third application area of CPA or rail plasma accelerators is in production of electromagnetically driven shock waves. Here, we require the arc to be in the form of a thin impermeable current sheet and to act as a magnetic piston preceded by a shock wave. The associated relaxation phenomena behind such shocks are studied from a chemical kinetic point of view (Chang, 1970). In this way we can obtain much faster shocks than with the classical diaphragm version of shock tubes. The incomplete knowledge of physical processes involved in these experiments necessarily curtails evaluations, especially in this highly promising third area.

Another application of CPA is the acceleration of small projectiles ( $\approx 100\mu\text{m}$ ) to meteor velocities ( $\approx 20\text{ km/s}$ ) by exposing them to a stream of high density, fast moving plasma (Utah R.D. Co., 1970). A suitable insulator between the CPA electrodes could be the source of projectiles.

These experiments are of current interest, yielding better results than "classical" electrostatic accelerators of heavy particles.

A better understanding of the nature of CPA would be invaluable in the designing of such devices. An appreciable amount of experimental data and a number of theoretical models are available, but a basis on which to



design a particular device having the required operational parameters is not available, and each device requires thorough operational testing (Sadowski *et al.* 1968).

In comparison with pure electrothermal and electrostatic mechanisms, electromagnetic interactions are both technologically and theoretically more complex. The situation becomes even more difficult because of the transient erosion of the insulator and electrodes. The problem of the electron-emission mechanism in an "ordinary" steady arc has still not been satisfactorily solved (Hoyaux, 1968). Here we are dealing with transient arcs ( $\sim$  microseconds), moving reasonably fast ( $\sim$  cm/ $\mu$ s) and carrying heavy currents ( $\sim$  100 kA). Such arcs under certain conditions create a narrow current sheet. Few reliable experimental data exist describing the time between application of voltage and beginning of sheet motion.

This study furnishes an improved model of steady gas flow between the current sheet and preceding shock wave (here called the shocked layer model). Also, the numerical solution of this model is given for an axisymmetric case (ideal gas only), and for a quasi-one-dimensional case (helium with two degrees of ionization). It should be pointed out, however, that any model describing one particular mode of acceleration is highly limited in use.

Experimental efforts have been concentrated on two shapes of the teflon insulator and two related modes of acceleration have been examined.

A few comments about the chapter contents are in order. Chapter 2 is devoted to a description and discussion of physical processes of a real but simplified CPA. Chapter 3 discusses the more mathematical treatment of shocked layer models and the simplifications necessary for numerical solution of those. Some of the difficulties of related numerical



calculations are explained in Chapter 4. Calculations in two spatial variables are compared with calculations in the literature, and the quasi-one-dimensional solution is compared with available experimental data. Details of the apparatus (accelerator and diagnostics) are described in Chapter 5, which includes an original version of a unipolar pulse generator (100 kA, 35  $\mu$ sec) with circuit analysis and experimental verification. Two completely different modes of acceleration for two teflon insulator shapes are described in Chapter 6. Finally, Chapter 7 gives conclusions and the author's perspective on the problem.





## CHAPTER II COAXIAL PLASMA ACCELERATOR

An incomplete state-of-the-art of CPA is given in this chapter. Literature on this subject is extensive and written from various points of view although at present, it is impossible to write a unifying theory of a CPA. On the other hand, the amount of accumulated information is sufficient to give a brief outline of certain typical kinds of behaviour (here called regimes) and certain basic types of CPA.

A review of CPA is arranged in the following manner:

TYPICAL REGIMES (2.1). A regime is a certain "simple" kind of behaviour occurring during a small part of the complete process.

MODELS OF REGIMES (2.2). A model is usually a set of mathematical relations and conditions, and related sets of solutions. These models are based on further simplification of physical processes.

BASIC TYPES OF CPA (2.3). Using the terminology developed in the section dealing with regimes, we can give a few basic types of CPA. This section is written more generally for pulsed plasma accelerators.

OTHER PHYSICAL PROCESSES (2.4). This section covers some important processes not discussed before.

The last Section 2.5 gives conclusions regarding our possible work in this study.

### 2.1 TYPICAL CPA REGIMES

Each particular accelerator should undergo two or more regimes from



the following list. Unfortunately, a real accelerator will perform some mixture of these modes and the experimentalist must carefully distinguish the importance of each mode involved. This again means that in describing these modes, we are dealing with a simplified, idealized accelerator.

### 2.1.1 Discharge-initiation Regime

During this stage the total discharge current should grow from zero to, say, one tenth of the maximum value. First, the working medium is prepared and ionized. There are three basic arrangements for the discharge initiation: (a) A small amount of gas is introduced by a fast-acting valve into the evacuated barrel, and ionized. (b) A surface discharge is initiated on a nonrefractory insulator, and the ablation product becomes a suitable medium. (c) A metallic foil is clamped between the inner and the outer electrode and the interelectrode space is evacuated. The main current pulse first melts and evaporates this foil to produce a suitable working medium.

In all cases a localized discharge is required. Case A is simply realized by means of holes for the gas inlet. Case B is improved by a suitable ignition electrode. In some cases such triggering is performed by a "small" plasma gun.

The first phase has received very little attention from experimentalists. It is an accepted fact that this stage leaves the accelerating gap full of unknown preionization, precursors, etc. It is essential to understand that this results in serious uncertainty of some parameters in all the following regimes.

Occasionally a bell-shaped distribution of current density several



millimeters thick is generated. This process depends on the kind of working medium used. Another very important parameter is the current rise-time, given by the external circuit design.

There are no quantitative theories and only rarely are experiments devoted specifically to investigation of the resulting current spreading.

### 2.1.2 Shock-tube Regime

Here, we assume that an impermeable thin current sheet has already been generated. The situation is much easier if we also assume that the current layer is of infinite conductivity. Then the magnetic field ( $B$ ) is non-zero only behind the sheet and its effect can be accounted for by the magnetic pressure term,  $(B^2/2\mu)$ . In other words we have a moving magnetic piston. What kind of disturbance will be created is now dependent on the piston velocity and the gas medium in front of the piston. Usually a dissociating and/or ionizing shock wave is created which is separated from the driving layer.

### 2.1.3 Plasmoid-acceleration Regime

For this regime one usually assumes that there is no gas in front of or behind the plasmoid. The plasmoid itself is created by the rather broad current layer moving along the CPA electrodes. In some models the motion is described for the plasmoid center of gravity and the thicker current layer is assumed to be localized at the same place, i.e., one dimensional models are considered.





#### 2.1.4 Fast-plasmoid-creation Regime

It is known that an important characteristic of the accelerator operation is in the gas-pressure distribution along the system, which governs the slow (Section 2.1.3) and fast regimes of accelerator operation. The slow regime is characterized by a current sheet of velocity  $10^7$  m/s and by gas combustion. In the fast regime, most of the plasma acceleration ( $10^8$  m/s) occurs in the density gradient where intense polarisation oscillations are produced (Kalmykov *et al.* 1971 and Khizhnyak, 1970).

This topic will not be described further here although much work remains to be done.

#### 2.1.5 Plasma-ejection Regime

This phase is a transition between the movement inside the channel wherein the plasma is created and accelerated, and the ordered streaming motion of the gas (plasmoid) outside the accelerator barrel. This regime is theoretically very difficult. Experimental effort has been primarily concentrated on one special version of this regime, the dense plasma focus which is described in the following section.

#### 2.1.6 Dense-plasma-focus Regime

In some cases, during the plasma ejection from the end of a CPA, part of the stored magnetic energy in the accelerator and external circuit is rapidly converted to plasma energy. This process occurs during the sheet's



brief collapse toward the axis.

Typical parameters of the phenomenon are: plasma densities  $\sim 10^{19} \text{ cm}^{-3}$ , temperatures of a few keV, life-time of 100 nsec, spatial dimensions of a few mm<sup>3</sup>. An excellent review is given by Loveberg and Griem (1971).

### 2.1.7 Inertial-plasmoid-motion Regime

Here we assume that a localized amount of plasma (plasmoid) is moving, but no external force from any external energy source acts on the plasma. During the ejection phase, many "long" extended current loops have been established and now these loops are broken. Internal vortex loops may still be expected in the plasmoid.

This regime is usually obtained outside the accelerator barrel and is considerably less complex than those regimes dealing with the space inside. For the above reason, this phase has received most experimental and theoretical effort, primarily because of the plasma-injector applications.

Let us note that if the current pulse is short and the accelerator barrel is long, then such a regime could still be attained inside the barrel.

## 2.2 MODELS OF SOME CPA REGIMES

The regimes introduced in Section 2.1 cover a certain important time during the acceleration development. We should realize that the real physical processes are sometimes more complex. Furthermore, the transition from one "simple" regime to another is difficult to study both from the



theoretical and experimental point of view. On the other hand, these separate regimes are relatively easy to describe using simple models.

### 2.2.1 Discharge-initiation Model

The discharge-initiation regime has been described in Section 2.1.1 with the conclusion being that there are no suitable quantitative theories available. For the static-gas-pressure type with the perfectly refractory insulator, Jahn and von Jaskowsky (1968) give a simple, skin-effect-like explanation for a one-dimensional discharge. One can envisage the breakdown process beginning with a short-lived uniform glow discharge over the entire channel. As the current density rapidly rises, driving the discharge through an abnormal glow towards an arc, the associated distribution in the time derivative of the magnetic field induces a new component of interior electric field, opposing the applied potential and preferentially discouraging current flow across the portions of channel farthest removed from the external circuit. The current thus intensifies most rapidly near the channel entrance.

### 2.2.2 Shock-tube Models

Referring to Section 2.1.2, we know that a current layer acts as a magnetic piston, and that a shock wave is driven by this piston. Some models of this piston-shock situation are available, and others may be created by the extension of some special shock wave models (current sheet is then placed on the contact surface position), or by extension of current layer models. A short list of such models with brief explanations





will follow. GAS-KINETIC MODEL covers such situations where individual electron, ion and neutral trajectories may be examined under the prevailing circumstances of Hall parameters, gyro radii and mean free paths. It is known that this approach is very difficult even for only a normal plane ionizing shock without current layer and magnetic field (Zel'dovich and Raizer, 1966). Collision processes and relaxation-layer discussions also belong in this group.

MULTI-FLUID MODEL in comparison to the previous case is macroscopic as to chemical equilibrium in the region between the driving layer and the shock wave. Thermodynamic functions are used to include changes due to dissociation, ionization, and excitation of the gas. The presence of a magnetic field in this calculated region, depends on the assumed current sheet conductivity, or an external field may be assumed.

SINGLE-FLUID MODEL with given finite conductivity neglects the multi fluid behaviour and chooses a set of equations to represent a single-fluid acted on by some source of force.

GAS-DYNAMIC MODEL treats a current sheet as an impermeable piston driving a gas dynamic shock ahead of it (at a somewhat higher velocity) into the undisturbed gas. The shock wave is followed by a uniform region of hot gas which is bounded by the current sheet. Ordinary Rankine-Hugoniot relations for constant specific heat ratio  $\gamma$  (in Section 3.2 called simply shock relations) can be used. The real gas effect is expressed by using some effective value of  $\gamma$  close to 1.0.

SNOW-PLOW MODEL is very common in the literature and we may define such a model simply as a special case of the previous gas-dynamic model with the effective specific ratio being  $\gamma = 1.0$ . From the detached shock



wave theory we know that this assumption leads to a zero shock-piston distance. It is a well known fact that the mass of the accelerated layer is accumulated from some "initial-breakdown" value. This model will appear again in Section 2.2.3 as a limiting case.

SLUG MODEL is also a special case of the aforementioned gas-dynamic model. Here, the gas density in front of the layer is assumed to be zero, i.e., no shock wave is created, and no mass accumulation occurs. This means that the layer (plasmoid) of constant mass is accelerated along the electrodes. This model does not really belong under the heading of shock-tube models, but it is the last simplification of these models.

The previous models could be treated as stationary cases or as time-dependent models, in one, quasi-one, or two spatial dimensions. By the quasi-one-dimensional model we mean that instead of dependent variables  $Y(r,z)$ , say, we will use variables  $Y(r,z(r)) = Y^*(r)$ . In other words, we will get a set of ordinary differential equations instead of a set of partial differential equations.

Let us give a few bibliographical notes for those models. An excellent review of shock-wave phenomena, time dependent one dimensional shock-piston models, relaxation effects behind a shock wave including radiation, is given by Zel'dovich and Raizer (1966). The problems of establishing local thermal equilibrium in a helium plasma created inside the CPA at pressures of .5 to 1 Torr, and related relaxation effects are discussed by Lie *et al.* (1967). They conclude that the collisional and the radiative processes which determine the population densities of He III, and the various bound states of He II and He I are of such a nature that the local thermal equilibrium assumption is in fact a satisfactory approx-



imation for the conditions of their experiment. This work has been extended in a later paper (Lie *et al.* 1970) in which the temperature was measured spectroscopically as well as by laser scattering, where the assumption of local thermal equilibrium is not required, and the results are in agreement with their previous work.

The multi-fluid approach with equilibrium chemistry in hydrogen in an electromagnetic field is discussed by Taussig (1966). In his calculations, no assumption is made concerning that of the contact surface being driven by the piston. His results show that solutions including chemical reactions are similar to the ideal gas (normal) ionizing shock wave solutions.

The single-fluid model of MHD shock tubes is given by Hoffman (1967). His concern was with a diffusing current sheet driving a shock wave, and he found that under many conditions, separation is more likely to be achieved with a decrease, rather than an increase, in current sheet speed. The gas-dynamic model in one dimension and in time is given by Morse (1962). The energy source consists of one charged capacitor and a constant specific heat ratio is assumed. Approximate closed-form solutions, for "small" and "long" time, are also given.

A quasi-one-dimensional, stationary, gas-dynamic model of the CPA has been developed by Pert (1968). He also gives some analytical solutions to this problem. The same author (Pert, 1969) extended his previous model for real gas effects in hydrogen when equilibrium single ionization is included in the energy equation. Butler *et al.* (1969) give a model similar to Pert (1969) but use only a threshold approximation for a "general" single ionization.





Two-dimensional time dependent gas dynamic (ideal gas) calculations are also described by Butler *et al.* (1969). The snow-plow model is very simple and still found to be adequate for some shock-tube investigations (Chang and Kofoed, 1968). The "old" slug model remains in use too. Vondra *et al.* (1970) discussed the teflon pulsed thruster by using this model. It will be shown in this study that in such cases the current is distributed along the electrodes, and that the existence of a slug of a plasma is unlikely.

### 2.2.3 Plasmoid-acceleration Model

Following is a description of the time dependent linearized model of the CPA. Such an accelerator consists, for example, of parallel-plate electrodes with inductance  $L_1$  per unit length, and a capacitor  $C_0$  charged to voltage  $V_0$  (see Fig. 2.1). A very narrow current layer of mass  $m_0$  is created at position  $x = 0$  and time  $t = 0$ . The layer (plasmoid) is ideally conducting and is accelerated by the electrodynamic force  $F_{ed}$  and decelerated by the drag force  $F_{drag}$ . The insulator is assumed to be perfectly refractory, i.e., no ablation products and hence no currents near this insulator for  $t > 0$ .

The momentum conservation law and two circuit equations are usually written in the following form (Artsimovich, 1963):

$$\frac{dmv}{dt} = F_{ed} - F_{drag}, \quad (2.1)$$

$$I = -C_0 \frac{dV}{dt}, \quad (2.2)$$



$$\frac{dLI}{dt} + RI - V - V_{\text{plas}} = 0 \quad (2.3)$$

where  $v = dx/dt$  is the plasmoid velocity,  $L = L_0 + L_1 x$  is total inductance of the circuit and  $V_{\text{plas}}$  represents some plasmoid voltage drop.

The model description starts from the electrodynamic force  $F_{\text{ed}}$  created by the magnetic pressure  $B^2/2\mu$  ( $\mu$  is permeability), acting on the left-hand-side plasmoid surface of area  $bd$ , i.e.,

$$F_{\text{ed}} = bd B^2/2\mu. \quad (2.4)$$

Assuming that  $b \gg d$ , using (ITT Co., 1969), one can write the following equations for the magnetic field,  $B$ , which is inside the accelerator:

$$B = \mu I/2 \quad (2.5)$$

and the following for the inductance per unit length,

$$L_1 = \mu db, \quad (2.6)$$

and finally from Eqs. (2.4), (2.5) and (2.6) the electrodynamic force is

$$F_{\text{ed}} = \frac{1}{2} L_1 I^2 \quad (2.7)$$

Some basic assumptions regarding the mass rate processes must be included:



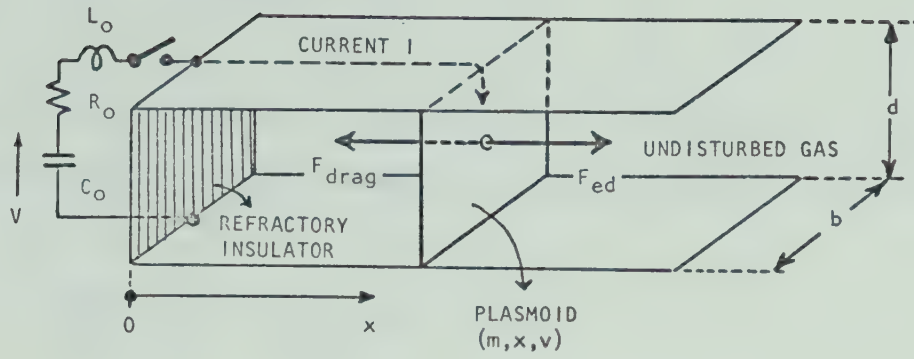


Fig.2.1 Sketch of the linearized CPA.

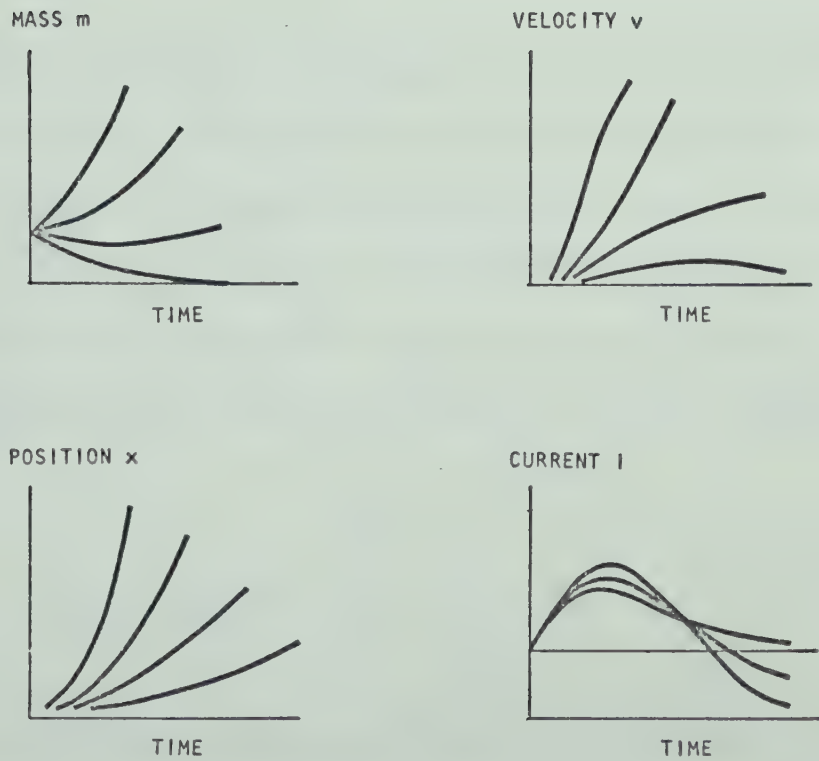


Fig.2.2 Types of solutions to plasmoid-acceleration model.





$$\frac{dm}{dt} = S(t, x, v, I, \dots) \quad (2.8)$$

as well as those concerned with the nature of the drag force  $F_{\text{drag}}$ . For the simplest version, the SLUG MODEL, one obtains the following equations

$$\frac{dm}{dt} = 0, \quad F_{\text{drag}} = 0. \quad (2.9)$$

Some mass accumulation is contained in the SNOW-PLOW MODEL, with the following assumption:

$$m = m_0 + b\rho x, \text{ or } dm/dt = b\rho v \quad (2.10)$$

$$F_{\text{drag}} = 0.$$

As previously mentioned, the hypersonic current layer drives a shock wave, with the gas in the layer-shock region (shocked layer) being very hot. Hence, the gas is ionized and dissociated, with an effective specific heat ratio  $\gamma = 1.0$ . Some authors (for example, Kolesnikov and Stolovich, 1970; K-S henceforth) neglect this type of mass accumulation.

The undisturbed gas effect is partially covered by the drag-force term

$$F_{\text{drag}} = b\rho v^2 \quad (2.11)$$

This is simply a dynamic pressure  $\rho v^2$  times the plasmoid surface  $bd$ . On the other hand, combining Eqs. (2.1) and (2.10) one gets



$$(m_0 + b d \rho x) \frac{d^2 x}{dt^2} = F_{ed} - b d \rho v^2, \quad (2.12)$$

i.e., one has derived an effective drag term and with the addition due to K-S, the mass accumulation is included.

More sophisticated mechanisms of the mass rate processes and drag forces have been developed during the 1962-1972 period, and are summarized by K-S:

$$\frac{dm}{dt} = -a_1 m - a_2 m^2 + a_3 |I| + a_4 I^2, \quad (2.13)$$

$$F_{\text{drag}} = b_1 v + b_2 v m + b_3 |I| v. \quad (2.14)$$

The  $a_1 m$  term accounts for particle diffusion, charge-exchange and electron attachment; the  $a_2 m^2$  term describes mass decrease due to particle recombination; the  $a_3 |I|$  and  $a_4 I^2$  terms respectively describe erosion mass addition due to ion bombardment, and electrode melting due to Joule heating. The drag force terms denote the following:  $b_1 v$  represents friction between the moving plasma and electrodes and  $b_2 v m + b_3 |I| v$  expresses friction due to mass transfer. The coefficients  $a_3, b_3$  are purely empirical, others could be estimated from simplified mechanisms (K-S).

The usual manner of solving Eqs. (2.1) to (2.3) is to transform those equations into some dimensionless form, to choose initial conditions and typical parameters, and then to solve that set of ordinary differential equations. Figure 2.2 exhibits such solutions. For details see K-S and many other authors.



An important conclusion from these figures is that the resulting solution  $[m(t), v(t), x(t), I(t)]$  is an extremely complicated function of the parameters  $(a_1, \dots, b_3, \rho, V_0, C_0, \dots)$  with the theoretical estimations at best being very rough. Parameter estimation from experimental measurement is difficult and is more dependent on the assumptions than on the true physical picture. For example, Sarah (1969) using the snow-plow model assumes only electrode erosion. Similarly, different experimental conditions dictate a variety of explanations for limited plasmoid velocities.

#### 2.2.4 Current-sheet Models

The present topic is concerned with a different approach to plasmoid acceleration, which has had an equally long history. These more sophisticated models make experimental verification more difficult. The problem is sketched in Fig. 2.3.

Before proceeding further let us introduce some classifications of the idealized situation. The regions #1 and #2 of Fig. 2.3, are represented by corresponding gas density  $\rho_i$ , gas velocity  $v_i$ , gas pressure  $p_i$ , magnetic field  $B_i$ , electric field  $E_i$ , and electric conductivity  $\sigma_i$ . The following classification of Burton (1968) shown in Table 2 is not generally accepted, but on the other hand, such a classification clarifies other papers in this field.

Models of this type are available in MHD single and two-fluid approximations, for collision dominated electron motion, and for ionization through the current sheet. A critical review of those models is given by





Pert (1970 a,b).

Leaving out mathematical details of the above models, let us give the resulting description of the sheet acceleration with the collision dominated electron motion (Khiznyak and Kalmykov, 1967). One assumes that the current sheet is already created. The electrodynamic force  $j \times B$  acts directly on the electron component and accelerates the current front along the electrodes. Neutral gas of region #1 is ionized by the current front and increases the plasmoid mass. The ions, dragged by the established polarization front attain one half the velocity of the polarization front, with most of the plasma being dragged behind the current front. The polarization front creates longitudinal electrostatic waves in the plasma concentrating the plasma in potential wells. Since the axial electric field has an oscillatory character, the current forms a series of closed loops within the plasma. The total discharge current  $I$  is equal only to the current flowing in the front and tail of the plasmoid. Electrodynamic acceleration (Section 2.2.3) occurs only when the energy of these electrostatic oscillations is small in comparison to the energy of the directed plasmoid motion. These electrostatic oscillations are intensified by driving the current sheet through the gas density gradient (Khizhnyak, 1970). The latter case results in creation of a fast moving plasmoid.

This model does not forecast any mass accumulation in front of the fast current layer. Conclusions of other models (Hoffman, 1967) are similar. In recent papers such separations have been experimentally observed, and a missing mass-accumulation mechanism has been determined: resonant charge-exchange collisions of neutrals with ions (Pert, 1970c and Val'kov *et al.* 1970).

A rather simplified, but very common description of the current sheet



Table 2 Classification of steady MHD discontinuities.

TYPE OF DISCONTINUITY	$B_1$	$\sigma_1$	$\sigma_2$
MHD SHOCK	$>0$	$>0$	$>0$
IONIZING SHOCK	$>0$	$=0$	$>0$
CURRENT SHEET	$=0$	$=0$	$=0$
CURRENT SHEET WITH PRECURSORS	$=0$	$>0$	$=0$

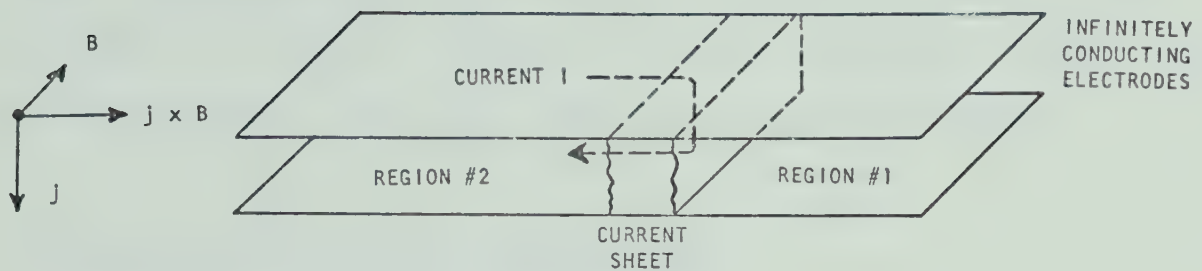


Fig.2.3 Diagram of current sheet motion.

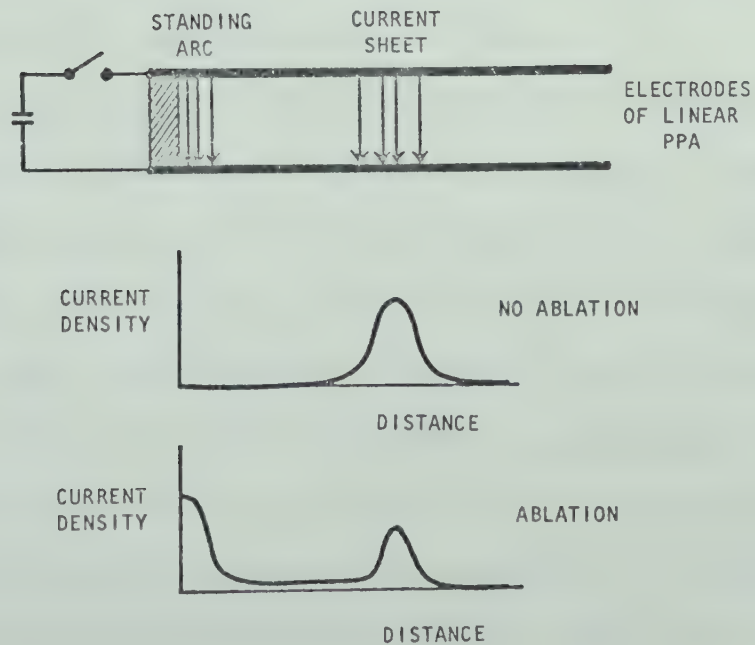


Fig.2.4 Sketch of insulator ablation model for one time instant.



assumes that ionization occurs at the front of the sheet. Then the electron Hall parameter  $\omega_e \tau_e \gg 1$  and the ion Hall parameter  $\omega_i \tau_i \leq 1$ , whereby, all current is carried by electrons. Thus

$$j_e = e n_e \frac{E}{B} , \quad (2.15)$$

i.e., the electron current density  $j_e$  is due to the  $E \times B$  drift of the electrons in the crossed polarization field  $E$  and magnetic field  $B$  (Jahn and von Jaskowsky, 1968; Pert, 1970c; and Valkov *et al.* 1970).

### 2.3 BASIC PULSED-PLASMA-ACCELERATOR TYPES

As has been noted in the introduction, some basic features are common for several pulsed plasma accelerators (PPA in the following text). This means that after introducing the typical regimes and related models, we can more easily describe some basic types of PPA.

It is useful to roughly divide these types into two groups. The first covers those used to supply a gas or plasma with energy or momentum in a relatively short time, and the inertial-plasmoid motion regime is then established. This group includes the various forms of T-tubes, and of conical, theta, and Z pinch devices. The second group is comprised of those systems in which the accelerated plasma is continuously supplied with energy and momentum so that a steady state can be achieved with the right kind of energy storage (current pulse generator). Typical members of the second group are the CPA and the parallel accelerator, sometimes called coaxial and rail gun respectively. The first group is reviewed by





Muntenbruch (1969). This study is concentrated on the second group. One could mention that the division of the PPA in these two groups is not the best, because the same short CPA, for example, belongs to the second group for the plasmoid acceleration regime, but it belongs to the first group for the inertial-plasmoid-motion regime.

### 2.3.1 Pulsed-gas Type

Here, the space between relatively long (coaxial) electrodes is evacuated. Then a puff of gas is introduced by a fast-acting valve into the barrel space, through the holes in the central electrode near the insulator. The gas has approximately  $100\mu\text{sec}$  to spread out. Now the pulse of current is introduced, i.e., the discharge initiation regime is performed and a current layer is created in the neighbourhood of the admitting holes. The remaining gas forms an ionized gas cloud and the current layer drives a shock wave through this cloud, i.e., the shock-tube regime is obtained. When the current layer, or better the current front, reaches the end of the cloud the plasmoid acceleration and ejection regimes should follow.

The most common example of this type is the plasma injector, designed for generation of hot plasma for thermonuclear research. Different modifications of the CPA are used for this purpose. One advanced form has the outer and inner electrodes made from rods, i.e., these electrodes are "transparent" for the particles rotating in the magnetic field. The technical difficulties connected with the construction of such a device are explained by Gryzinski *et al.* (1968).



### 2.3.2 Dielectric-erosion Type

There are many known geometrical versions of this type. The feature in common is a nonrefractory dielectric placed between two metallic electrodes. An auxiliary ignition electrode starts a surface breakdown followed by a rapidly increased insulator erosion (ablation). This is caused by surface arc discharges, supplied from the external current pulse generator. This is known as a dielectric-erosion kind of the discharge-initiation regime of a PPA.

The next step depends on the current pulse shape, on the energy supply generator, and on the shape of the metallic electrodes. For example, 10 cm long rail plate electrodes are used for pulsed solid thrusters (Vondra *et al.* 1970).

### 2.3.3 Electrode-erosion Type

The PPA of this kind is also called the end type PPA, because plasma is formed from the eroded material from the ends of the two metallic electrodes, which are separated by a heat-resistant dielectric. The erosion mechanisms are of current interest (Khizhnyak *et al.* 1971).

### 2.3.4 Shock-tube Type

Basically, for this we assume that the accelerator has two long electrodes, the space between is filled by a certain gas of known pressure and the current layer (magnetic piston) is created during some suitable discharge-initiation regime. The required current pulse is long and unipolar, if possible. Now, the conditions should be such that a well



separated shock wave is driven at a constant speed by the current layer. In the literature, the electromagnetic (electric, magnetic) shock tube is a device where the inertially moving plasmoid drives a shock wave outside of the accelerator.

### 2.3.5 Static-gas-pressure Type

We can easily show that this type is similar to one or more of the previous types depending on electrode geometry, insulator type, gas pressure, and current pulse shape. This name has been introduced because this type is very common in experimental research of the PPA.

## 2.4 OTHER PHYSICAL PROCESSES

In the previous part of Chapter 2 we introduced some regimes in CPA behaviour and described a few current models for those regimes. Later, we introduced basic types of PPA. Further details of the physical processes involved follow below.

PRECURSOR MECHANISMS. In a realistic model of PPA the effect of precursors should be taken into account. From this point of view, the experimental results and theoretical conclusions for classical pressure driven shock waves, given by Weyman (1969), are of interest. For one set of conditions he found that electron diffusion is the major factor in the production of precursors. After improving the vacuum conditions, photo-ionization was the dominant factor in precursor production.

Lubin (1966) studied the precursor waves in an electromagnetic T-tube





(hydrogen and argon, 1 Torr); his conclusions were in close agreement with the nonlinear ionizing electromagnetic wave model. The same author regards the following mechanisms as unimportant: electron diffusion from the main shock wave or from the discharge region, soft X-rays from electron bombardment of the anode, the ionizing shock waves. Many authors report experimental results with photo excitation and ionization as the most possible explanation (Fearn, 1968).

RELAXATION EFFECTS. In many models of electromagnetic accelerators, the relaxation effects are neglected. Lie *et al.* (1970) calculated ionization relaxation times in a homogeneous, transient plasma. Since collisional ionization occurs mainly via intermediate excited states, the ionization relaxation time is determined by the slowest process in the excitation chain. For single ionization of helium initially at a pressure of 1 Torr, they observed a relaxation time of  $10^{-8}$  to  $10^{-7}$  sec. For double ionization they observed  $3 \times 10^{-7}$  sec for  $n_e \geq 10^{17} \text{ cm}^{-3}$  to several microseconds for  $n_e \approx 5 \times 10^{16} \text{ cm}^{-3}$ . Comparing these times with plasma lifetime ( $10^{-6}$  sec) the second case is quite high. Relaxation behind strong shock waves in a monatomic gas and in multi-atomic gases is discussed by Drawin (1971). Ionization by precursors and by initial breakdown of the "undisturbed" gas in the accelerator is highly important, but usually unknown. When unspecified impurity atoms are present, the ionization process may change. Argyropoulos *et al.* (1969) made a study of the coupled distribution of current density, electron temperature, and plasma composition in non-equilibrium plasma flows, and how these depend on relaxation effects arising from finite reaction rates and electron-energy convection.

DISCHARGE PINCHING. The spatially periodic structure of a heavy



surface coating, by adsorbed gas or different oxides, will be stabilized by those preliminary discharges. The fact that a boundary, which exists between the plasma and electrodes, weakens present theories is generally accepted (Hoyaux, 1968).

Conditioning of the glass insulator plate for the vacuum spark gap is described by Mather in Lovberg and Griem (1971) as the formation of numerous metallic sites none of which overlap on the glass surface. These metallic sites disperse uniformly over the surface and form a microscopically graded insulator, which can sustain large electric fields without breakdown. Conditioning mechanism in the CPA may be similar.

PLASMA FLOW BEHIND THE CURRENT SHEET. Toroidal paravortices are formed in the wake of a moving current sheet in a coaxial plasma gun. The axial Hall electric field, proportional to the axial driving force, falls off as  $r^{-2}$  from the central electrode. The vector sum of this Hall field, and a radial electric field which falls off as  $r^{-1}$ , gives rise to a net electric field of over-increasing tilt as a function of radius. The electric particle drift caused by this field pattern produces the necessary swirl in the wake. That is, considerations of conservation of mass and momentum flow in the CPA make it apparent that plasma vortices are produced behind the current sheet. The above conclusions of vortices measurements are due to Bostick *et al.* (1965). A similar current vortex structure, behind the current sheet in a parallel plate rail gun, is reported by Pert (1970c). This vortex must be distinguished from the gas flow "bubbles", which are periodically formed and detached from the discharge in the rail and coaxial guns. For the rail gun, this latter phenomenon is limited to a narrow pressure region (Pert, 1970d). Drift



velocity of the plasma, behind the current sheet and the vortices is given by the relation

$$\vec{U}_d = \frac{\vec{E} \times \vec{B}}{B^2} \quad (2.16)$$

where  $\vec{E}$  is the radial electric field and  $\vec{B}$  is the azimuthal magnetic field. This velocity, for a short part of the discharge current duration, may be either in opposite direction to the current sheet velocity (Zolototrubov *et al.* 1965), or in the same direction and of a greater magnitude than the current sheet velocity (thus called a fast plasma component). The motion of a single charged particle inside a CPA with static electric and magnetic fields,  $E$  and  $B$ , is considered more generally by Kulinski (1966). Some of his conclusions may be used for certain cases of flow behind the current sheet.

INSULATOR ABLATION. Theoretical investigation of this effect on the performance of magnetic piston shock tubes is given by Workman (1965). A related model is sketched in Fig. 2.4. A simple correlation-parameter model of Workman involves the magnetic field, undisturbed gas density, and ionization energy of the insulator vapor. The above model permits determination of the loss in a given experiment.

Lie (1970), reporting results related to refractory and non-refractory insulators, claims Workman's theory is insufficient because the electrode-radius-ratio is not taken into account. Still no improved version of the insulator-ablation model is available.

## 2.5 CONCLUSIONS

Regimes and types of the pulsed CPA have been given in Chapter 2.





Study of the CPA is more than ten years old, yet this quick and incomplete review shows us that the experimental and theoretical investigation of the CPA is far from being satisfactory. In the experimental field, the dielectric erosion type of accelerator is of increased interest, so two shapes of teflon insulator are investigated in this study.



## CHAPTER III THEORETICAL DESCRIPTION OF THE SHOCK-TUBE REGIME

Previous investigators have studied the shock tube in various approximations of physical processes involved, from gas-kinetic to snow-plow models. Different numbers of independent variables have been used, from the simple time dependent model in one space variable,  $Y(z(t))$ , to the time dependent model in two space variables,  $Y(r,z,t)$ . The object of this chapter is to analyze the steady (stationary) gas flow in the region between the idealized curved driving current sheet and the shock wave.

The problem, formulated in Section 3.1, gives the conservation laws in integral form. Such a form can be attacked via different levels of numerical approximation. The form also allows both gas dynamic and chemical-equilibrium expressions for some dependent variables.

Equilibrium conditions, for one special case behind the plane shock wave, are given in Section 3.2. Two axisymmetric versions of the resulting model are then developed. The two-dimensional, and the quasi-one-dimensional models are described in Section 3.4.

### 3.1 FORMULATION OF THE STEADY SHOCK-TUBE MODEL

Consider the plasma acceleration between two coaxial electrodes with inner radius  $r_0$  and outer radius  $\gg r_0$ . To carry out the analysis, we further make the following assumptions, not strictly rigorously formulated.



The situation is illustrated in Fig. 3.1.

AS1. The current sheet is thin, ideally conducting, already created, stable and axially symmetrical, and moving at a constant speed  $v_0$  in the  $-z$  axis direction.

AS2. The current sheet acts as an impermeable (magnetic) piston driving a (detached) shock wave into the undisturbed gas. The gas in front of this shock wave is not preheated (not ionized) and the gas behind the shock wave is in some specified equilibrium. The relaxation layer between those two states can be neglected.

AS3. The conductivity of the gas in the region between the current sheet and the shock front (shocked gas, or shocked layer) is high enough to ensure that the driving current  $I$  is confined within this thin sheet.

AS4. The layers adjacent to the electrodes are thin in comparison with the distance between the electrodes and the effect of these layers can be ignored.

AS5. An external generator provides a current pulse such that the current  $I$  confined within the current sheet is constant during the time of investigation.

AS6. The magnetic field,  $B$ , behind the current sheet is

$$B(r) = \mu I / 2\pi r \quad (3.1)$$

where  $\mu$  is the permeability,  $I$  the driving current, and  $r$  the radius (independent variable). Because the current sheet is ideally conducting and thin, the effect of this magnetic field can be reduced to some magnetic pressure  $p_{\text{mag}}$ , acting on the sheet:









$$p_{\text{mag}} = B^2/2\mu = \mu I^2/8\pi^2 r^2 \quad (3.2)$$

AS7. The density of the shocked gas is sufficiently high that the following integral form of the conservation of mass, momentum and energy can be used for any control volume inside a shocked layer (Becker, 1968):

$$\begin{aligned} \int_S \rho v_n dS &= 0 , \\ \int_S (\vec{v} \rho v_n + \vec{n} p) dS &= 0 , \\ \int_S \rho (h + \frac{1}{2} v^2) v_n dS &= 0 . \end{aligned} \quad (3.3)$$

The examples of the control volume are shown in Figs. 3.1 and 3.2. In Eq. (3.3),  $S$  is the control volume surface,  $\vec{v}$  is the velocity,  $\vec{n}$  is the outward normal unit vector,  $v_n = \vec{v} \cdot \vec{n}$  is the normal component of the velocity,  $\rho$  is the mass density,  $p$  is the pressure, and  $h$  is the enthalpy per unit mass.

AS8. Two state equations are provided, for example, in the form:

$$\begin{aligned} p &= p(\rho, T) , \\ h &= h(\rho, T) . \end{aligned} \quad (3.4)$$

where  $T$  is the equilibrium temperature of the gas.

AS9. The problem is axisymmetrical and using Fig. 3.3, the boundary conditions are chosen:



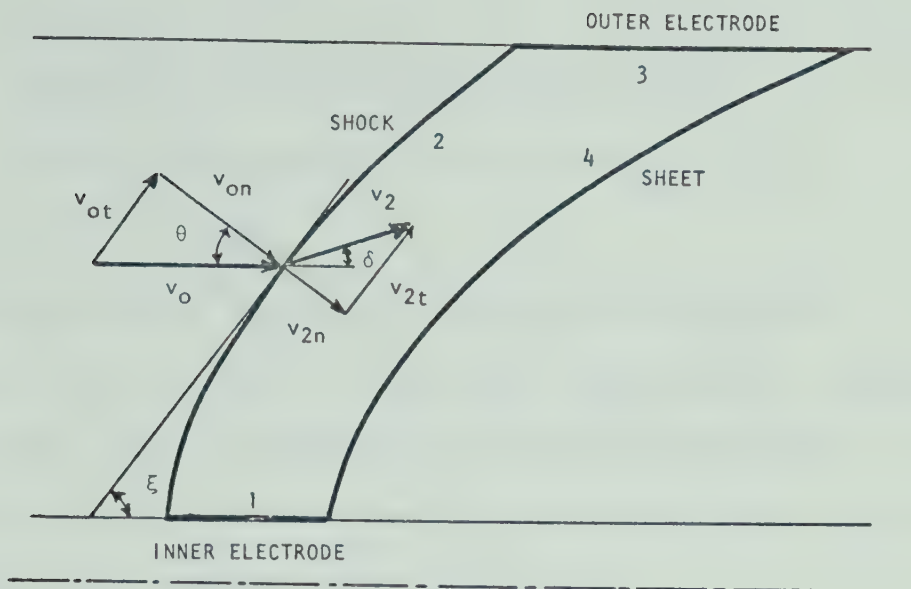


Fig.3.3 Sketch of the boundaries.

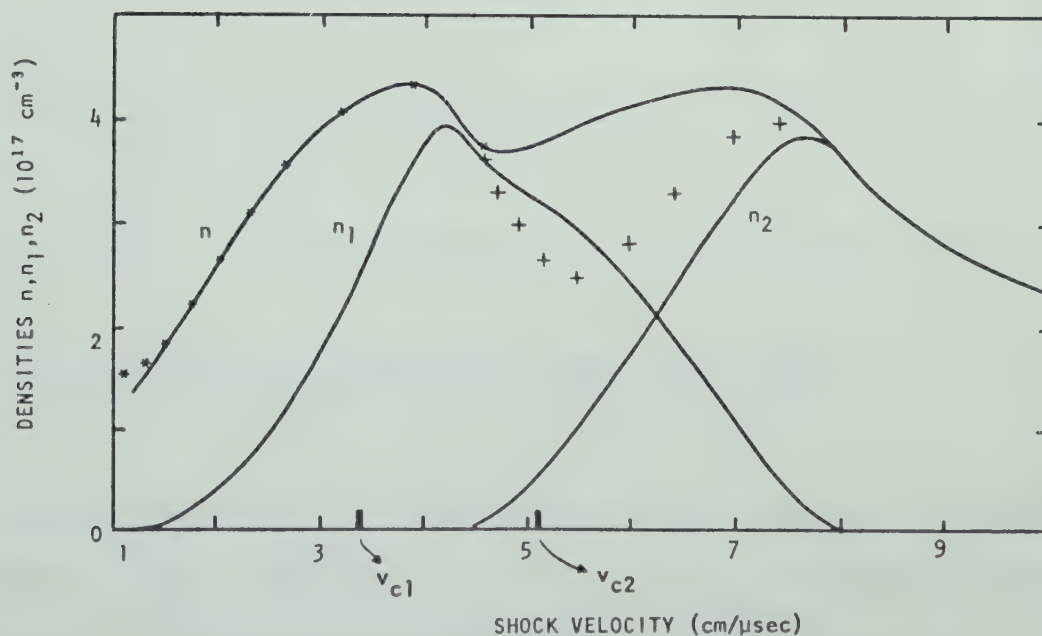


Fig.3.4 Calculated number densities  $n$ ,  $n_1$ , and  $n_2$  behind a plane shock wave of velocity  $v_0$  in helium of 1 Torr pressure. The critical velocities  $v_{c1}$  and  $v_{c2}$  were introduced by Butler et al. (1969). \*, values of  $n$  calculated by Horton and Menard (1969), all excitation levels included. +, values of  $n$  calculated by Fucks and Artmann (1963); wrong algorithm.



- #1:  $v_n = 0$
- #2: oblique shock relation (local approximation)
- #3: arbitrary (transparent outer electrode) (3.5)
- #4:  $v_n = 0, p = p_{\text{mag}}$

The oblique shock relations are discussed in Section 3.2.

AS10. The effect of viscosity and thermal conductivity is neglected. The form of Eq. (3.3) can be rewritten in an approximate form. With reference to Fig. 3.2, the surface  $S$  of the control volume consists of six elements  $\delta S_i$ . Now, the approximate form is

$$\sum_{i=1,6} \rho_i v_{ni} \delta S_i = 0 ,$$

$$\sum_{i=1,6} (\vec{v}_i \rho_i v_{ni} + n_i p_i) \delta S_i = 0 , \quad (3.6)$$

$$\sum_{i=1,6} \rho_i (h_i + \frac{1}{2} v_i^2) v_{ni} \delta S_i = 0$$

where the subscript  $i$  means average value over the surface element  $\delta S_i$ .

### 3.2 EQUILIBRIUM CONDITIONS BEHIND A STEADY SHOCK WAVE

Boundary conditions for the shock wave can be obtained by choosing a suitable control volume (see Fig. 3.2), placing the boundary between the surfaces 2 and 4, and then limiting the thickness  $\Delta$  to zero.

Assuming that the total control volume surface  $S = \sum \delta S_i$  is small then the resulting relations are common oblique shock relations (Becker, 1968):





$$v_{ot} = v_{2t} ,$$

$$\rho_o v_{on} = \rho_2 v_{2n} ,$$

$$\rho_o v_{on}^2 + p_o = \rho_2 v_{2n}^2 + p_2 , \quad (3.7)$$

$$h_o + \frac{1}{2} v_o^2 = h_2 + \frac{1}{2} v_2^2 = h_{tot} = \frac{1}{2} v_M^2$$

where  $h_{tot}$  is the total (stagnation) enthalpy and  $v_M$  is the maximum velocity for expansion into vacuum. The last two values are used for normalization in some dimensionless models.

### 3.2.1 Calorically Ideal Gas

Assuming that the gas is calorically ideal then the specific heat ratio is usually 1.67, 1.40 and 1.33 for monatomic, diatomic, and polyatomic gas respectively. The velocity of sound,  $a = (\gamma p / \rho)^{1/2}$ , defines the Mach number

$$M = v/a \quad \text{or} \quad M_o = v_o/a_o \quad (3.8)$$

Finally, the equations of state are

$$p = \frac{R}{m} \rho T, \quad h = \frac{\gamma}{\gamma-1} \frac{p}{\rho} \quad (3.9)$$

where  $R = 0.8313 \times 10^4 \text{ m}^2 \text{ sec}^{-1} \text{ } ^\circ\text{K}^{-1}$  is the universal gas constant and  $m$



is the dimensionless molecular weight. Now, the boundary conditions, Eq. (3.7), can be rewritten in this form

$$\begin{aligned}\rho_2/\rho_0 &= f_1(\gamma, M_0, \xi) , \\ p_2/p_0 &= f_2(\gamma, M_0, \xi) , \\ \delta &= f_3(\gamma, M_0, \xi) .\end{aligned}\tag{3.10}$$

Details are readily available in Becker (1968).

### 3.2.2 Monatomic Gas

Equations (3.4) have a special form for equilibrium ionization of a monatomic gas. An excellent review of the equilibrium and nonequilibrium plasmas, including an equilibrium-condition discussion is due to Drawin (1971). Only those relations used for further calculations are presented in the following work.

Assuming the down-stream gas satisfies local thermal equilibrium conditions, then for a monatomic gas the so-called mass action law has a familiar Saha form:

$$\frac{n_{r+1} n_e}{n_r} = S_r^{r+1}(T, n_e) = \frac{2p_{r+1}^{int}(T) \cdot (2\pi m_e kT)^{3/2}}{p_r^{int}(T) h^3} \exp\left(-\frac{E_{r,r+1} - \Delta E_{r,r+1}}{kT}\right)\tag{3.11}$$

where subscripts or superscripts  $r$  and  $(r+1)$  are related to ionization stages  $r$  and  $(r+1)$ ,  $p^{int}$  is partition function,  $E_{r,r+1}$  is the ideal



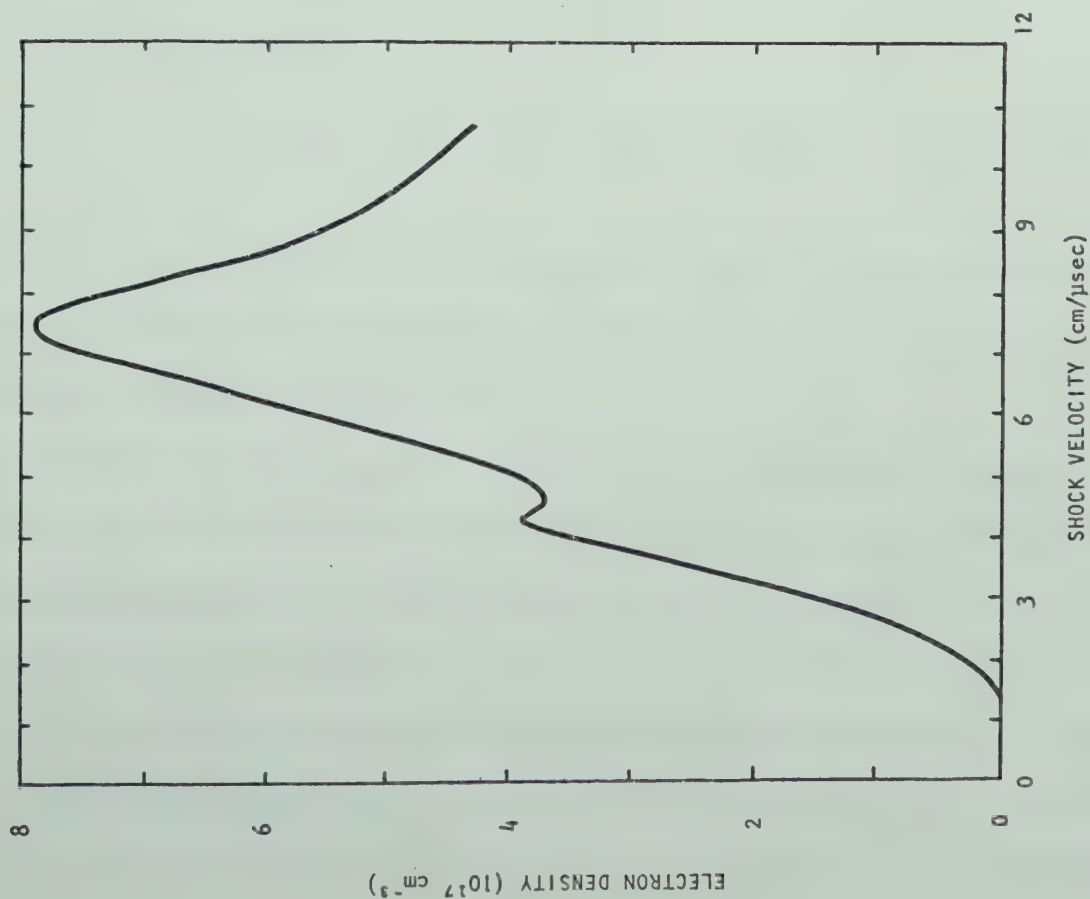


Fig. 3.5 Calculated electron number density versus shock velocity; normal shock wave, helium,  $P_0 = 1 \text{ Torr}$ ,  $T_0 = 293 \text{ }^\circ\text{K}$ .

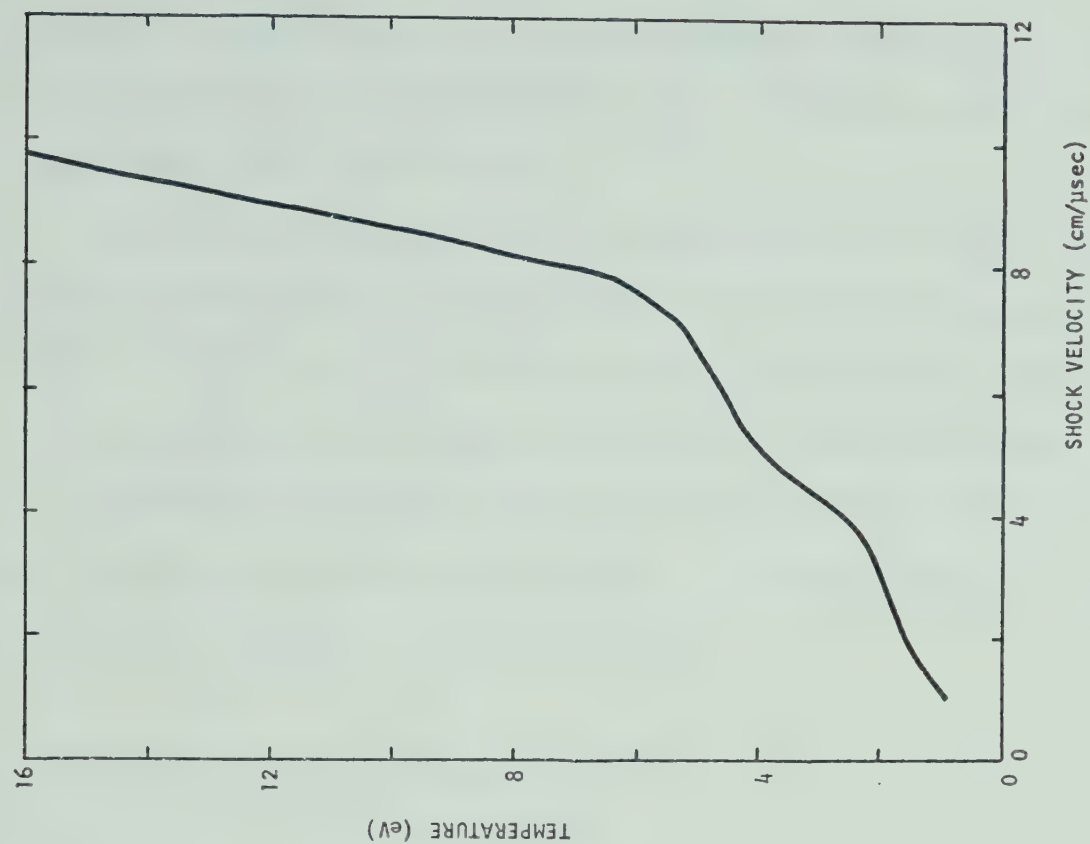


Fig. 3.6 Calculated equilibrium temperature versus shock velocity; normal shock wave, helium,  $P_0 = 1 \text{ Torr}$ ,  $T_0 = 293 \text{ }^\circ\text{K}$ .



ionization energy of the particle in ionization stage  $r$ ,  $\Delta E_{r,r+1} \sim \rho_D^{-1}$  is the lowering of ionization energy,  $\rho_D$  is the Debye radius, and other symbols have their usual meanings.

Reference to Fig. 3.4, where our calculations for helium are presented, makes clear that the differences between the simplified approach ( $p_{0,1}^{int} = 1$ ,  $p_{1,2}^{int} = 2$ ,  $p_{2,3}^{int} = 1$ ) and the more sophisticated (all excitation levels included) is not of basic importance in the calculation.

Introducing the number density of heavy particles:  $n = n_0 + n_1 + n_2 + \dots$  and the average mass of heavy particles  $m$ , the mass density  $\rho$ , pressure  $p$ , and specific enthalpy  $h$  are now given by:

$$\rho = \sum_r m_r n_r \approx mn$$

$$p = kT \sum_r n_r \approx kT(n + n_e)$$

$$h = \frac{1}{\rho} \left[ \frac{5}{2} kT(n + n_e) + n_1 E_{0,1} + n_2 (E_{0,1} + E_{1,2}) + \dots \right] \quad (3.12)$$

where  $r = (e, 0, 1, 2, \dots)$  is the summation index. In the enthalpy relation, the corrections due to excited states are usually neglected (Fucks and Artmann, 1963; F-A hereafter).

Now, having the required equations for pressure and enthalpy, Eqs. (3.12), we can combine then with Eqs. (3.7) and (3.11), and the problem of determination of the local thermal equilibrium behind a (locally) oblique shock wave can be solved.

The solution of the above equations has been perfected for the case of a normal plane shock wave in helium at pressures of 0.1 to 10 Torr. Figures 3.4 to 3.5 show results of the numerical solution for the case close to the





experimental situation studied here. The numerical constants are those of F-A, but the results are different (see Fig. 3.4). The reason for the discrepancies is found in the numerical solution of F-A (Artmann, 1963). Other authors have also discussed difficulties of this kind (Taussig, 1966; Lapworth, 1969). The main numerical problem is placed in the transition region between the first and second ionization. Solutions of this problem are available for many gases (Horton *et al.* 1969) but only for a limited shock velocity region; and in helium only for single ionization.

The second purpose of the calculation illustrated in Figs. 3.4 to 3.6 was to have a simple and verified subroutine for the equilibrium condition calculation. Such a subroutine can be used for the two- and quasi-one-dimensional model solutions.

### 3.3 TWO DIMENSIONAL MODEL

The problem formulated in Section 3.1 is known as a blunt body problem with given distribution of the pressure on the body (in this case the current sheet). Equations (3.6) and (3.4) are one version of the two-dimensional model. The form of Eqs. (3.4) depend on the assumptions regarding the gas. The form of Eqs. (3.6), however, is closely related to the method of solution. The integral form is best only for some numerical algorithms (Richtmyer, 1968). Usually, suitable curvilinear coordinates are introduced and Eqs. (3.6) are transformed into a set of (partial) differential equations. The transformation is done by choosing a coordinate oriented control volume in the limit of zero volume.



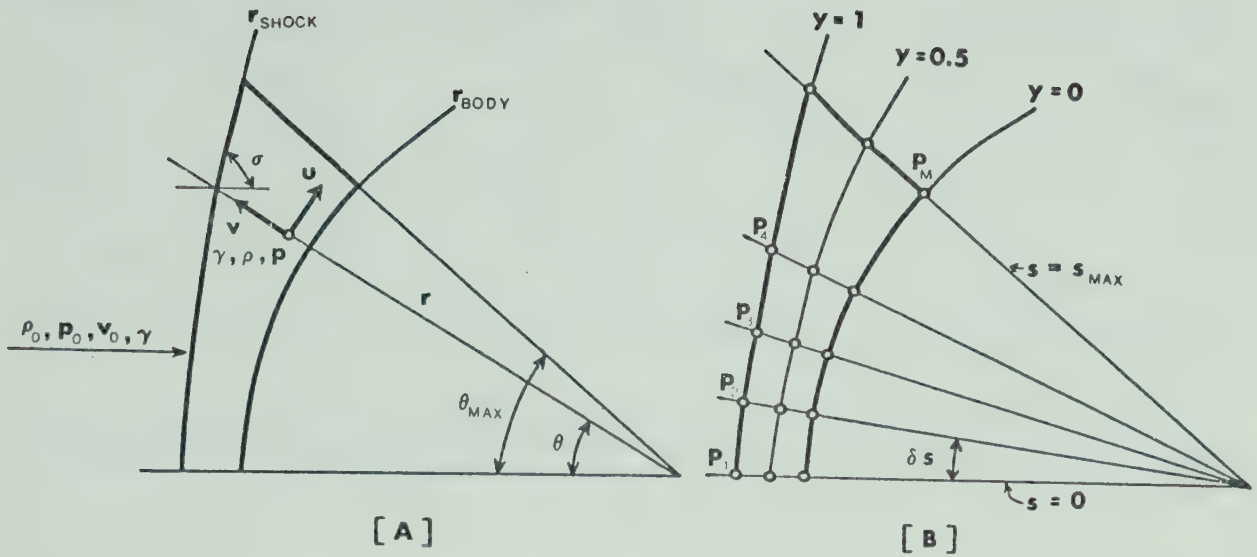


Fig.3.7 Diagram of the axisymmetric flow system showing the variables and notation used. In (B), the variables  $(r, \theta)$  are replaced by variables  $(y, s)$ . The region of interest is represented by points  $P_1, \dots, P_M$ .

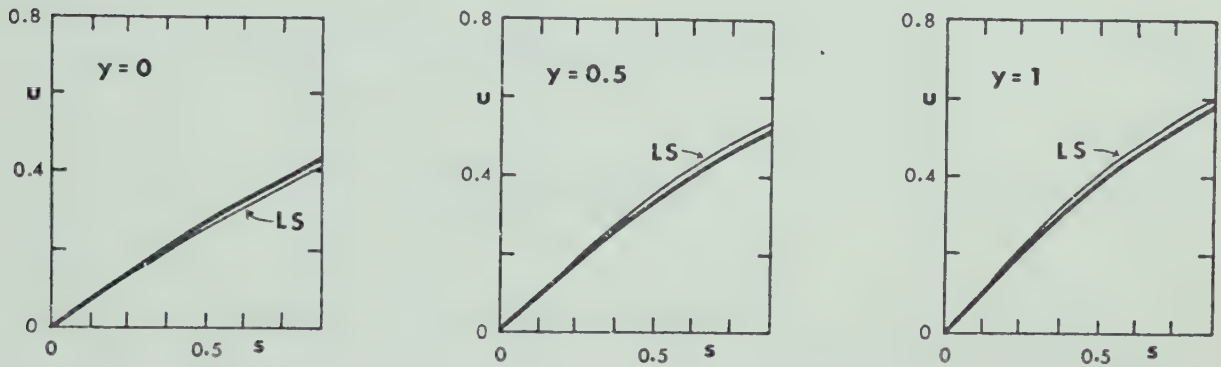


Fig.4.1 Comparison of  $u(s, y)$  calculated by LS-method with those calculated by Belotserkovskii et al. (1966); sphere, ideal gas,  $M_0 = 10$ ,  $\gamma = 1.4$ .

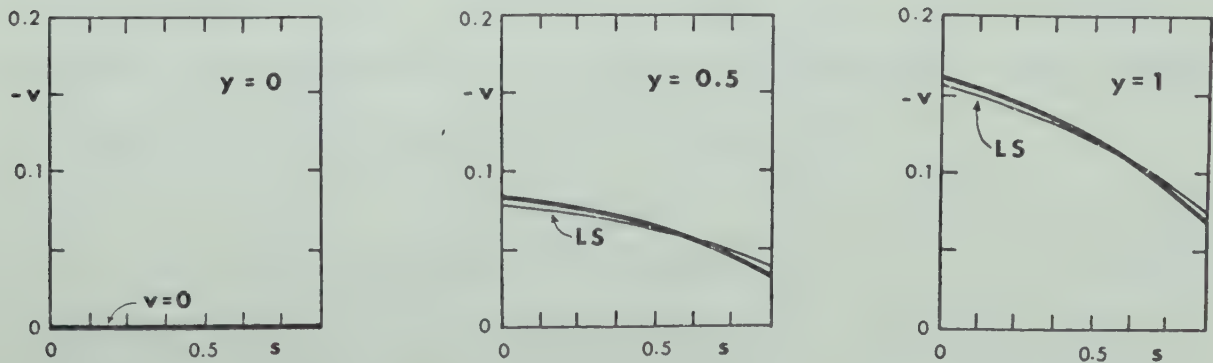


Fig.4.2 Comparison of  $-v(s, y)$  calculated by LS-method with those calculated by Belotserkovskii et al. (1966); sphere, ideal gas,  $M_0 = 10$ ,  $\gamma = 1.4$ .



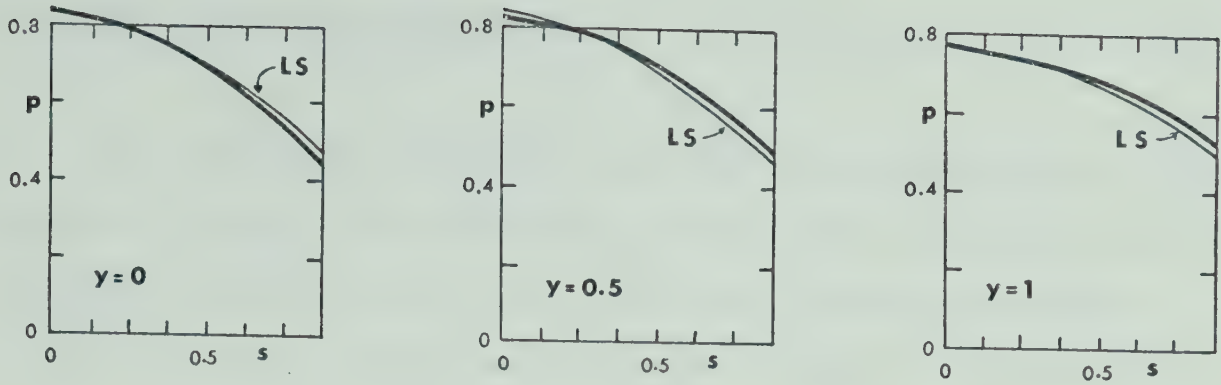


Fig.4.3 Comparison of  $p(s,y)$  calculated by LS-method with those calculated by Belotserkovskii et al. (1966); sphere, ideal gas,  $M_0 = 10$ ,  $\gamma = 1.4$ .

For spherical coordinates, the results of this transformation are found to be (Bird *et al.* 1960):

$$\frac{1}{r^2} \frac{\partial}{\partial r}(\rho r^2 v) + \frac{1}{r \sin \theta} \frac{\partial}{\partial \theta}(\rho v \sin \theta) = 0 ,$$

$$\rho \left( v \frac{\partial v}{\partial r} + \frac{u}{r} \frac{\partial v}{\partial \theta} - \frac{u^2}{r} \right) + \frac{\partial p}{\partial r} = 0 , \quad (3.13)$$

$$\rho \left( v \frac{\partial u}{\partial r} + \frac{u}{r} \frac{\partial u}{\partial \theta} + \frac{vu}{r} \right) + \frac{1}{r} \frac{\partial p}{\partial \theta} = 0$$

where  $v$  and  $u$  are now the components of the velocity in the  $r$  and  $\theta$  directions, see Fig. 3.7. These equations do not contain the transformation of the energy equation. The reason for this is that, using an appropriate assumption, one can replace the differential equation by a known integral, for example, by the Bernoulli equation (Pert, 1969):

$$h_{\text{tot}} = h + \frac{1}{2}(u^2 + v^2) = \text{const} \quad (3.14)$$

Details of the numerical solution are discussed in Section 4.1.





### 3.4 QUASI-ONE-DIMENSIONAL MODEL

The previous two-dimensional model will be shown to require a lengthy numerical solution. To simplify the problem, we will assume that all dependent variables of the shocked layer are functions of one space variable,  $r$ , say. In other words, the shocked layer is assumed to be thin. Referring to Fig. 3.1 where the cylindrical coordinates  $(r, z, \theta)$  are used, this also means that the control volumes of Fig. 3.2 has the surface element  $\delta S_4$  on the current sheet and  $\delta S_2$  on the shock wave.

One can imagine a simple algorithm, solving numerically Eqs. (3.4) and (3.6) for a series of points placed in the middle of the control volumes between the sheet and shock. More common, however, are methods for solution of ordinary differential equations. Using a procedure similar to that in Section 3.3, one can write Eqs. (3.6) for the control volume of Figs. 3.1 and 3.2, and in the limit of  $\delta r \rightarrow 0$ , the following set of ordinary differential equations is obtained:

$$\rho_0 v_0 = \frac{1}{r} \frac{d}{dr} (\rho v r \Delta), \quad (3.15)$$

$$\rho_0 v_0^2 \cos \theta - \frac{p_{\text{mag}}}{\cos \theta} = \rho v^2 \Delta \frac{d\theta}{dr}, \quad (3.16)$$

$$\rho_0 v_0^2 \sin \theta = \frac{1}{r} \frac{d}{dr} (\rho v^2 r \Delta) + \Delta \frac{dp}{dr}, \quad (3.17)$$

$$\rho_0 \left( h_0 + \frac{1}{2} v_0^2 \right) v_0 = \frac{1}{r} \frac{d}{dr} \left[ \rho \left( h + \frac{1}{2} v^2 \right) v r \Delta \right], \quad (3.18)$$

where the subscript  $o$  refers to undisturbed gas,  $\rho = nm$  is gas density,  $v$  is gas velocity,  $\Delta$  is shocked layer thickness,  $h$  is specific enthalpy,



$(r, \theta)$  are coordinates defined by Fig. 3.1,  $p$  is pressure,  $p_{\text{mag}}$  is magnetic pressure, and  $m$  is the mass of heavy particles.

Using the assumptions that  $v(r_0) = 0$  (stagnation line near electrode) and that  $h_0 \ll \frac{1}{2}v_0^2$ , the mass and energy conservation laws can be integrated to give

$$\rho v r \Delta = \frac{1}{2} \rho_0 v_0 (r^2 - r_0^2) \quad (3.19)$$

$$h = \frac{1}{2} (v_0^2 - v^2)$$

Note that the last equation is again the Bernoulli equation (3.14) in changed notation.

The  $z$  coordinate of the middle of the shocked layer can be related to the  $(r, \theta)$  coordinates (see Fig. 3.1) by the relation

$$\frac{dz}{dr} = \tan \theta \quad (3.20)$$

Now, our model contains Eqs. (3.16), (3.17), (3.19), and (3.20). The equilibrium conditions of the gas should be added, i.e., for the ideal-gas by Eqs. (3.9), or for equilibrium ionization of a monatomic gas by Eqs. (3.11) and (3.12).

Unfortunately, the model is still incomplete (more unknowns than relations) due to the quasi-one-dimensional assumption. This can be overcome, however, by making an additional assumption concerning the solution. Accordingly, the closing relation is taken to be that used by Butler *et al.* (1969):



$$p = \frac{1}{2} (\rho_0 v_0^2 \cos^2 \theta + p_{\text{mag}}) \quad (3.21)$$

Here, the magnetic pressure  $p_{\text{mag}}$  is given by Eq. (3.1). In other words, the pressure in the layer is approximated by an average of dynamic pressure on the front and magnetic pressure on the back.

Numerical solution of Eqs. (3.11), (3.12), (3.16), (3.17) and (3.19) to (3.21) is discussed in Section 4.2.



## CHAPTER IV NUMERICAL TECHNIQUES

The steady shock-tube models, described in the previous chapter, involve some specific problems investigated in this chapter. General formulation of the model transformed our problem into a numerically difficult group of problems, called the blunt body problem (Hayes and Probstein, 1968).

Calculation of supersonic compressible fluid flow around blunt bodies has received considerable attention in recent years. Several successful numerical calculations have been made using techniques like:

- (i) Finite difference method (Gentry *et al.* 1966; Amsden, 1966)
- (ii) Method of integral relations (Belotserkovskii, 1966).
- (iii) Pade's expansion method (Van Tuyl, 1970)

A common feature of those methods is that they are very complicated and sensitive to variation of some parameters. For example, to make the method of finite differences stable, one has to use certain "artificial diffusion", introduced only for such a reason (Van Leer, 1969).

In Section 4.1 is described a variational method, the discrete non-linear least squares (NLS) method, applied to this problem. Such an approach has not appeared in the literature, to the author's knowledge.

The NLS method in our modification is written with two independent variables and involves a two level minimization procedure. Two level minimization places strict requirements on the convergence of the method. In the case discussed here it is done by a two level non-linear least





squares procedure. Non-linear approaches are based on a "sensible" first guess to the solution, followed by iterative improvements of the weighting coefficients or functions (in the case of more than one condition/equation) to obtain the "exact" solution. A general description of the variational approach may be found in Mikhlin (1971).

The advantages of this method are:

- a) In the case of trans-sonic flow the method is stable through the sonic line; the discontinuity at this point is a problem in many Eulerian or Lagrangian techniques, but may also be overcome by using a mixed coordinate system such as the P.I.C code (Amsden, 1966).
- b) The solution of the problem for the entire flow region is described by a small number of parameters (10 to 50), so that the method has only small memory requirements.
- c) Any known physical properties of the solution may be easily included in the form of the approximating functions, e.g. if the functions are even or odd.
- d) The problem can be easily inverted (e.g. given shock wave, pressure distribution etc., calculate shape of body etc).

In Section 4.2, the same problem is simplified by using a quasi-one-dimensional assumption, i.e., the set of ordinary differential equations is to be solved subject to the initial conditions. The Runge-Kutta method (R-K) is used in combination with the solution of a simultaneous set of nonlinear equations (equilibrium conditions).

Initial conditions have to be found by using a suitable assumption and then replacing the differential equation by an auxiliary set of additional nonlinear equations. Solution of the extended set gives the required initial conditions. The last procedure physically means that the flow has a stagnation line near the central electrode and, to find the gas parameters



and the shock-sheet distance, we need to make an assumption regarding the resulting flow in the region near the stagnation line.

The NLS solution is done only for very simplified cases and compared with known solutions. The R-K solution is compared with existing experimental results in the literature.

#### 4.1 LEAST-SQUARES SOLUTION TO THE TWO-DIMENSIONAL MODEL

In this section, one numerical experiment is described attempting to solve the steady shocked layer model in two spational variables. It is assumed: (i) the current sheet is spherical and the central electrode radius is zero, (ii) gas has constant specific heat ratio  $\gamma$ .

A variational method, the NLS method is applied to this problem. The objective of this particular numerical experiment is to provide "adjustable" simplification to fluid-dynamic programs of some laboratories (say, of Los Alamos; Butler, 1969).

The basic idea of a variational approach is the transformation of a boundary value problem into a problem of finding the minimum of certain functionals. The previous assumptions transformed our problem into hypersonic flow around a sphere, whose solution is known (Belotserkovskii, 1966).

The model consists of Eqs. (3.9), (3.13), and (3.14), for example. These equations can be rewritten in the form of three differential equations for unknowns  $Y(u,v,p)$  with independent variables  $x = (r,\theta)$ :



$$f_1(x,Y) \equiv r(\rho v)_r + (\rho u)_\theta + \rho(2v + u \cot \theta) = 0$$

$$f_2(x,Y) = r p_r / \rho + r v v_r + u v_\theta - u^2 = 0$$

$$f_3(x,Y) = p_\theta / \rho + u u_\theta + r v u_r + u v = 0 \quad (4.1)$$

where partial derivatives are denoted by subscripts and where

$$\rho = \frac{\gamma}{\gamma-1} \frac{p}{h}, \quad h_{\text{tot}} = h + \frac{u^2 + v^2}{2} = \frac{1}{2} \quad (4.2)$$

The quantities  $u$ ,  $v$ ,  $p$ ,  $\rho$  and  $h$  are two components of velocity, pressure, mass density and enthalpy respectively, normalized to  $v_{\text{max}}$ ,  $v_{\text{max}}$ ,  $\rho_0 v_{\text{max}}^2/2$ ,  $\rho_0$  and  $v_{\text{max}}^2$  respectively. The subscript  $o$  is related to free stream values, velocity  $v_{\text{max}}$  is related to total enthalpy  $h_{\text{tot}}$ . Functions  $f_1$ ,  $f_2$ ,  $f_3$  have been introduced for further use in the variational reformulation of the problem.

The sketch of the flow system and notation used is in Fig. 3.7. Polar coordinates  $(r, \theta)$  are replaced by the "body-shaped" coordinates  $(y, s)$  according to the relations:

$$y = (r - r_{\text{BODY}}) / (r_{\text{shock}} - r_{\text{BODY}})$$

$$s = \int_0^\theta (r_{\text{BODY}}^2 + (dr_{\text{BODY}}/d\theta)^2)^{1/2} d\theta \quad (4.3)$$

where  $s$  is the length of the  $r_{\text{BODY}}(\theta)$  curve. Assuming that  $r_{\text{BODY}} = 1$ ,





in our case, the latter equation is reduced to  $s \equiv \theta$ . The purpose of this transformation is that the approximate functions in the next section are simpler in  $(y, s)$  variables.

The boundary conditions, Eqs. (3.5), can be rewritten into the following form:

$$v = 0 \text{ for } r = r_{\text{BODY}}, \quad u = 0 \text{ for } \theta = 0 \quad (4.4)$$

and

$$Y_{\text{SHOCK}} = Y_{\text{SHOCK}}(p_0, h_0, v_0, \sigma) \text{ for } r = r_{\text{SHOCK}} - \delta r \quad (4.5)$$

where  $Y_{\text{SHOCK}}$  denotes the value just behind the shock wave, the angle  $\sigma$  is shown in Fig. 3.7. Note that it is not possible in this particular case to write the boundary conditions for  $\theta = \theta_{\text{max}}$ , which are required if the finite difference approach is to be employed.

A great deal of theoretical work has been done on the problem of finding sufficiently wide classes of functions in order that some functionals actually attain their minimum (Mikhlin, 1971). This section presents two basic modifications of that "theoretical" approach:

i) The class of problems considered will be the one for which the approximate form of the solution,  $\tilde{Y}(x, A) = (\tilde{y}_1, \tilde{y}_2, \tilde{y}_3)$ , is known.

For example, let

$$\begin{aligned} u \approx \tilde{y}_1 &= A_1 \theta + A_2 \theta^3 + A_3 \theta^5 + (A_4 \theta + A_5 \theta^3 + A_6 \theta^5)y + (A_7 \theta + A_8 \theta^3 + A_9 \theta^5)y^2 \\ v \approx \tilde{y}_2 &= A_{10} + A_{11} \theta^2 + A_{12} \theta^4 + (A_{13} + A_{14} \theta^2 + A_{15} \theta^4)y + (A_{16} + A_{17} \theta^2 \\ &\quad + A_{18} \theta^4)y^2 \end{aligned}$$



$$p \approx \tilde{y}_3 = A_{19} + A_{20}\theta^2 + A_{21}\theta^4 + (A_{22} + A_{23}\theta^2 + A_{24}\theta^4)y + (A_{25} + A_{26}\theta^2 + A_{27}\theta^4)y^2$$

$$r_{\text{shock}} \approx A_1^* + A_2^*\theta^2 + A_3^*\theta^4 \quad (4.6)$$

ii) In this analysis of the detached shock wave problem, the position and shape of one part of the boundary (shock wave) is given implicitly by the Hugoniot relation, Eqs. (4.5).

We have already mentioned the method of integral relations, which has three versions (Scheme I, II, III). Our proposed method differs from the third version in the form of the functions given by Eqs. (4.6) and in the method by which the coefficients  $A$  and  $A^*$  are determined.

#### 4.1.1 Variational Formulation

Let  $A^*$  and the points  $x$  be given. The solution of the boundary value problem, Eqs. (4.1) to (4.5), is given by the set  $A$  for which the functional given by

$$F(A) = \sum_{\substack{k=1,3 \\ i=1,M}} w_k^2 \cdot f_k^2(x_i, \tilde{y}) \quad (4.7)$$

is minimal. The determination of weighting factors  $w_k$  will be discussed later.

A second functional

$$F^*(A^*) = F(A(A^*)) \quad (4.8)$$



is introduced for obtaining the solution for  $A^*$  under the assumption that the correct shock shape and position is Obtained when  $F^*$  is minimized.

The usual method (Mikhlin, 1971), for minimizing  $F$  and  $F^*$  involves the solution of equations

$$\begin{aligned}\frac{\partial F}{\partial A_\ell} &= 0, \quad \ell = 1, 2, \dots, N \\ \frac{\partial F^*}{\partial A_k^*} &= 0, \quad k = 1, 2, 3\end{aligned}\tag{4.9}$$

where the derivatives are replaced by numerical differentiation. If  $N$  is set to 27 in Eqs. (4.6), the boundary conditions, Eqs. (4.4) and (4.5) may be used to reduce  $N$  to 15. Providing a reasonable first guess for  $A$  and  $A^*$  is available, the solution to Eqs. (4.7) and (4.8) may be obtained by the two level minimization of  $F$  and  $F^*$  using some generalized Newton method (e.g., Newton-Kantorovich method; Mikhlin, 1971). The convergence of the above method, however, was found to be slow. An alternate technique was used to accomplish the minimization, and such a technique is described in Section 4.1.2.

The weighting factors  $w_k$  in Eqs. (4.7) are determined by using the assumption that the first guesses for  $A$  and  $A^*$  are good for at least small  $\Delta\theta$  (i.e., near axis) as follows:

- i) For the grid in Fig. 3.7 values for  $f_k(x_i, \tilde{Y})$  are evaluated with  $\Delta\theta = \Delta\theta/10$ .
- ii)  $w_k$  are then determined from the solution of the equations

$$\sum_{i=1, M} w_1^2 f_{1i}^2 = \sum_{i=1, M} w_2^2 f_{2i}^2 = \sum_{i=1, M} w_3^2 f_{3i}^2, \quad \sum_{k=1, 3} w_k^2 = 1 \tag{4.10}$$



### 4.1.2 Minimization of the Function of N-Variables

Minimization of the functionals  $F(A)$  and  $F^*(A^*)$  of Section 4.1.1 is described. Both the following algorithms have been developed for this study.

i) Minimization of  $F(A)$ . A more rapid convergence can be obtained if a better approximation to the minimized functional is available. This may be achieved by linearizing the functions  $f_k[x_i, \tilde{Y}(x_i, A)]$ ,  $k = 1, 2, 3$ ;  $i = 1, 2, \dots, M$ ; rather than linearizing the functions of  $\partial F / \partial A_\ell$ ;  $\ell = 1, 2, \dots, N$ ; in Eq. (4.7). This is performed by using the weighted non-linear least squares approach to solve the system of  $3M$  equations

$$f_k[x_i, \tilde{Y}(x_i, A)] = 0 \quad (4.11)$$

for  $A_1, A_2, \dots, A_N$ . This is accomplished by iterative improvements of a given first guess  $A^G$  through the solution of a linear least squares problem in the neighbourhood of  $A^G$ .

ii) Minimization of  $F^*(A^*)$ . The minimization of the second functional can be performed as follows:

a) in the neighbourhood of the first guess  $(A_1^*, A_2^*, A_3^*) \equiv (x_1^*, x_2^*, x_3^*)$ ,  $N^* > 10$  values of  $F^*$  are evaluated,

b)  $F^*$  is then approximated by the polynomial

$$\begin{aligned} F^* \approx F(a) = & a_1 x_1^2 + a_2 x_2^2 + a_3 x_3^2 + a_4 x_1 x_2 + a_5 x_1 x_3 + a_6 x_2 x_3 + a_7 x_1 \\ & + a_8 x_2 + a_9 x_3 + a_{10} \end{aligned} \quad (4.12)$$

c) if  $a_i > 0$  for  $i = 1, \dots, 6$  the next guess for  $(x_1^*, x_2^*, x_3^*)$  is





given by the solution of

$$\tilde{\partial F / \partial x_k} = 0 ; k = 1, 2, 3: \quad (4.13)$$

if  $a_i \leq 0$  for some  $i \in (1, \dots, 6)$ , the next guess can be determined using only first derivatives.

#### 4.1.3 Results and Comparison

The method described in the previous parts of Section 4.1 have been used to solve cases with specific heat ratio  $\gamma = 1.4$  ( $\sim$  air) and with Mach number  $M = 10$ . The chosen weighting functions were

$$w_1(y, \theta) = 0.15, w_2(y, \theta) = 0.61, w_3(y, \theta) = 0.77$$

i.e., only constants without iterative improvement, and three iterations of  $F^*(A^*)$  have been used,  $M = 2$ ,  $N = 15$ . The resulting shock wave was

$$r_{\text{SHOCK}} = 1.175 + 0.11 \theta^2 + 0.044 \theta^4 \quad (4.14)$$

The numerical results are compared with those obtained by the integral relation method, version III the so called method of transcendental equations; Belotserkovskii, 1966). Figures 4.1 to 4.3 indicate that the agreement is satisfactory.

The following conclusions can be drawn from the above analysis:

i) Detached shock wave problems can be solved using the least squares approach.



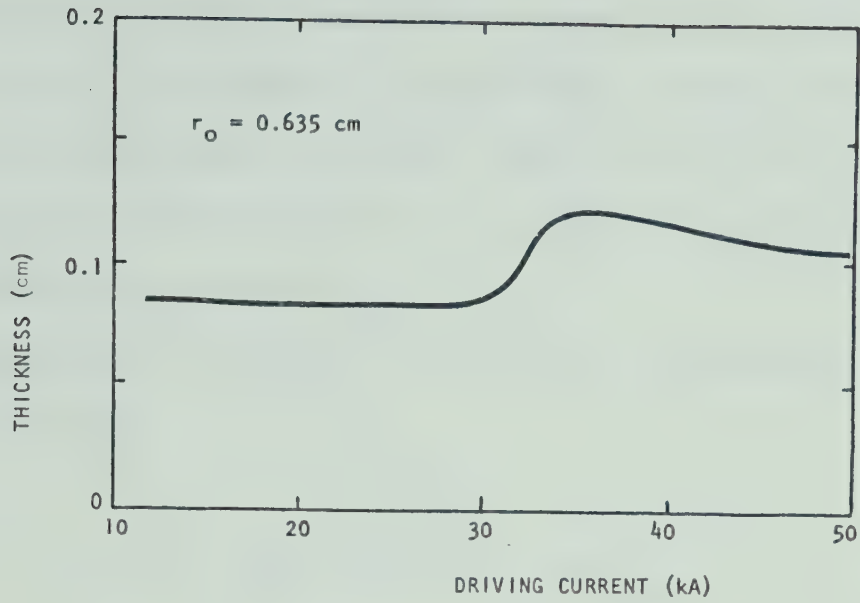


Fig.4.4 Initial condition calculation;  $\Delta(r_0 + \delta r)$  versus driving current; quasi-one-dimensional model.

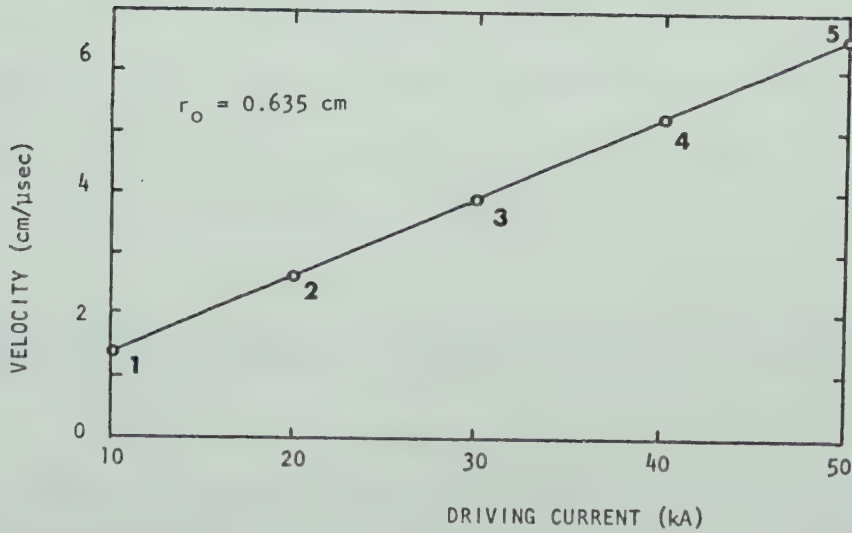


Fig.4.5 Ideal steady-state current sheet velocity versus driving current; points #1,...,#5 are of the same meaning as those in Figs. 4.7 to 4.14 .



ii) The calculation time is typically 2 minutes on IBM 360/67 for the case of a sphere in an ideal gas with the number of representing points  $M = 24$  (see Fig. 3.7); number of  $A$  coefficients, in Eqs. (4.6),  $N = 15$ ; and with three iterations for three  $A^*$  coefficients. This time may be improved by reducing the number of  $x_i$ ,  $A_j$ ,  $A_k^*$  used, or else using a faster minimization procedure.

iii) The solution is relatively insensitive to the values of weighting factors  $w_k$ , but for

$$w_1 = w_2 = w_3 = (1/3)^{1/2}$$

the procedure is unstable. Note that our polynomial approximations, Eqs. (4.6), are written for the whole region. Using the local polynomial approximation (spline functions, Greville, 1969) one may improve the stability.

iv) The resulting algorithm, only roughly described in Section 4.1 and by Jurak, Pert, and Capjack (1972) is rather complicated. The flow in a CPA, under more realistic conditions, will be attacked by using the quasi-one-dimensional simplification in Section 4.2.

## 4.2 RUNGE-KUTTA SOLUTION OF THE QUASI-ONE-DIMENSIONAL MODEL

One can easily see that the solution of the two-dimensional problem could be rather lengthy. The quasi-one-dimensional version, however, makes the situation much easier (Jurak and Offenberger, 1972). The model from Section 3.1 can be rewritten in form:





$$\frac{d\theta}{dr} = \frac{(a \cos\theta)/r_0^2 - a/(r^2 \cos\theta)}{\rho v^2 \Delta}, \quad a = \frac{I^2}{200\pi}$$

$$\frac{dv}{dr} = \frac{(a \sin\theta)/r_0^2 - (a v)/(v_0 r_0^2) - \Delta dp/dr}{\rho v \Delta} \quad (4.15)$$

$$\frac{dz}{dr} = \tan \theta, \quad \Delta = \frac{\rho_0 v_0}{\rho v} \frac{r^2 - r_0^2}{2r}$$

$$b(n + n_1 + 2n_2)T - p = 0$$

$$\frac{5}{2} \frac{p}{\rho} + p \frac{n_1 E_0 + n_2 (E_0 + E_1)}{\rho} - \frac{v_0^2 - v^2}{2} = 0$$

$$n_1(n_1 + 2n_2) - 2c(n - n_1 - n_2)T^{3/2} \exp(-E_0/T) = 0$$

$$n_2(n_1 + 2n_2) - c n_1 T^{3/2} \exp(-E_1/T) = 0 \quad (4.16)$$

where the pressure  $p = \frac{a}{2} \left( \frac{\cos^2 \theta}{r_0^2} + \frac{1}{r^2} \right)$  and the total number density  $n = \rho/m = n_0 + n_1 + n_2$ .

Comparing with Section 3.2 where mks units were used, here cgs are employed with the exception of temperature  $T$  and ionization potentials  $E_0$  and  $E_1$  which are in eV, and current  $I$  which is in A,  $b = 1.6 \times 10^{-12}$  erg/eV and  $c = 6.04 \times 10^{21} \text{ cm}^{-3} \text{ eV}^{-3/2}$  for helium.

Our problem is to solve a simultaneous set of three ordinary differential equations  $dY/dr = F_1(r, Y, P)$ , where  $Y = (\theta, v, z)$ , and  $P = (T, \rho, n_1, n_2)$  is given by the solution of the set of nonlinear equations  $F_2(P) = 0$ .



### 4.2.1 Initial Conditions

The initial value of  $v$  is given according to assumption AS9:

$$v(r_0) = 0$$

It is also assumed that

$$\theta(r_0) = 0 ,$$

$$z(r_0) = \Delta(r_0)/2 ,$$

where  $z$  is the coordinate of the middle of the shocked layer. Integration can not start from point  $r = r_0$ , because  $1/v(r_0) = \infty$  in Eqs.(4.15). The following approximations to the first two differential equations were made

$$\frac{d\theta}{dr} \approx \frac{\delta\theta}{\delta r} \approx \frac{\theta}{\delta r}$$

$$\frac{dv}{dr} \approx \frac{\delta v}{\delta r} \approx \frac{v}{\delta r}$$

which is "correct" only near  $r = r_0 + \delta r$ . Choosing sufficiently small  $\delta r$  (say  $\delta r = 0.01$ ), the complete set of model equations is now a set of nonlinear equations. Figure 4.4 shows one curve of this solution giving shocked layer thickness  $\Delta(r_0)$  as a function of the driving current  $I$ .

### 4.2.2 Integration of the Model

Knowing the initial conditions, we can use common Runge-Kutta procedures



for integration of the set of first order differential equations. The only difficulty was that for each integration substep the set of nonlinear equations had to be solved. An algorithm for nonlinear equations has been developed as a modification of the Seidel method (Ortega *et al.* 1970). Note that the problem of instability of the common Newton-Raphson method for equilibrium calculations (Taussig, 1966) has been overcome by using different (equivalent) forms of the same set of nonlinear equations for different regions of ionization. This algorithm was first verified by solving the problem of equilibrium ionization behind the plane shock wave in helium (Figs. 3.4 to 3.6).

Numerical stability of the latter procedure was verified by using a "very bad guess"; the incorrect solution of the same problem is also illustrated in Fig. 3.4, and the iterative improvement of the guess value to the correct value is shown in Fig. 4.6.

#### 4.2.3 Results and Comparison

Figures 4.7 to 4.14 show the results of the numerical solution of the model for helium at 1 Torr over a range of velocities which covers no ionization to doubly ionized. One important result of this model is (Fig. 4.13) that the shocked layer thickness does not go to zero at some radius as found by Butler *et al.* (1969). The model is very simple (less than 1 minute of computer time), so that extension to cases with different assumptions concerning ionization equilibrium or energy conservation are easily accomplished.

Our CPA, described in Chapter 5, was not operating in the required shock-tube regime, but there are available suitable experimental results



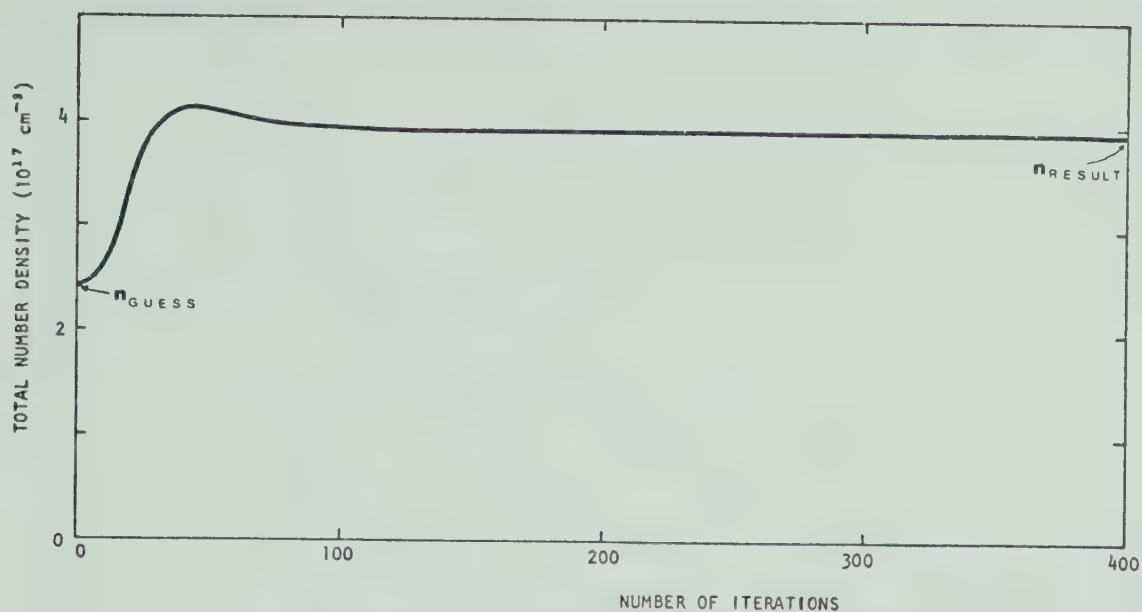


Fig.4.6 Iterative improvement of the guess value. The resulting value is one point on the  $n = n(v_0)$  curve of Fig.3.4 ( $v_0 = 4.5$  cm/sec).

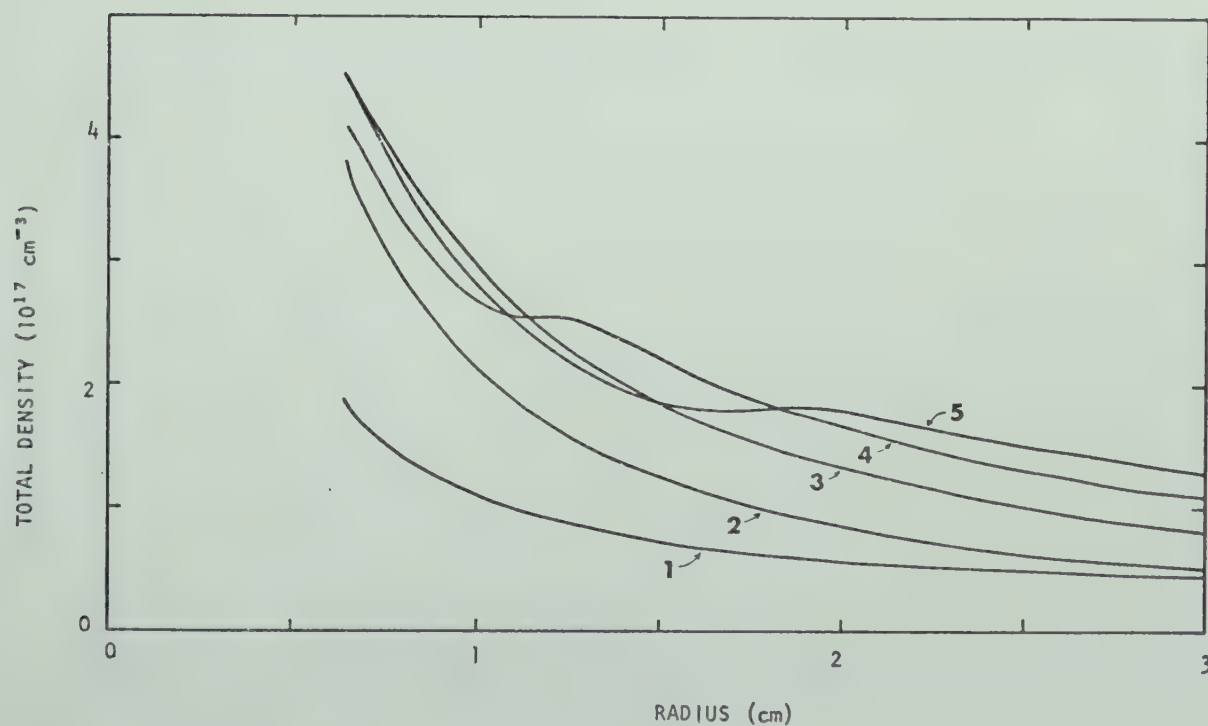


Fig.4.7 Calculated number density  $n = n_{\text{He}} + n_{\text{He}^+} + n_{\text{He}^{++}}$  versus radius; quasi-one-dimensional model. See also Fig.4.5 .





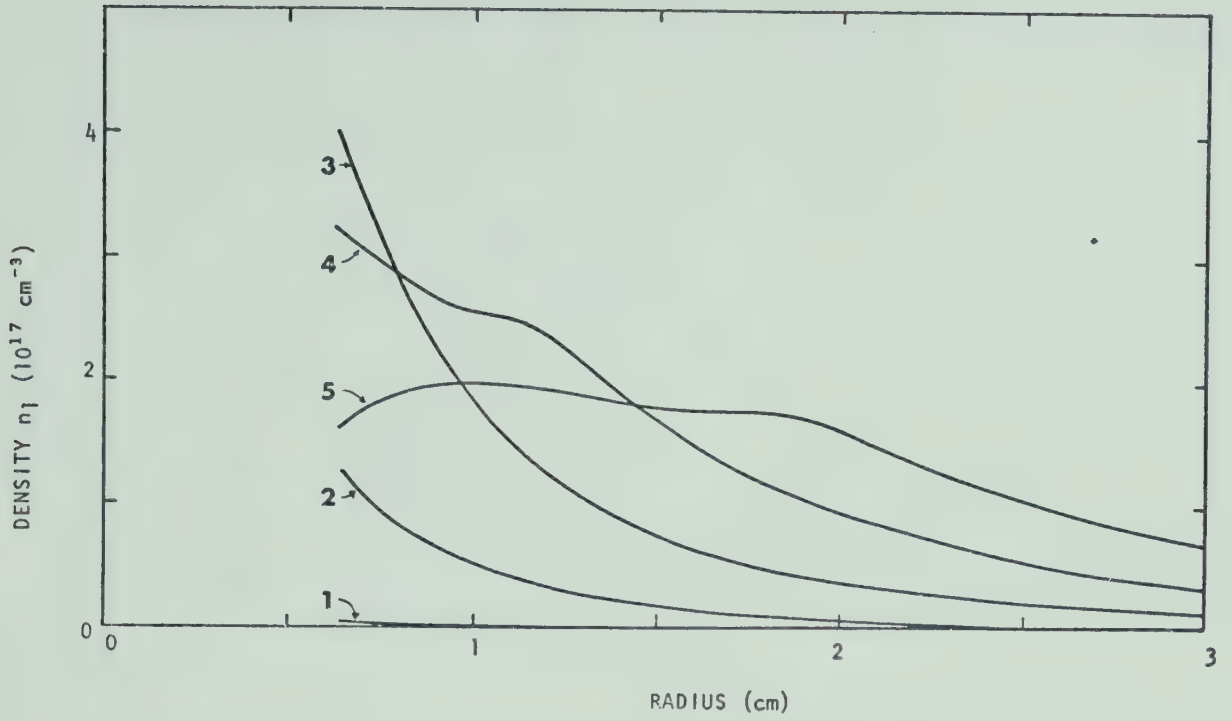


Fig.4.8 Calculated number density  $n_1 = n_{\text{He}^+}$  versus radius;quasi-one-dimensional-model.  
See also Fig.4.5

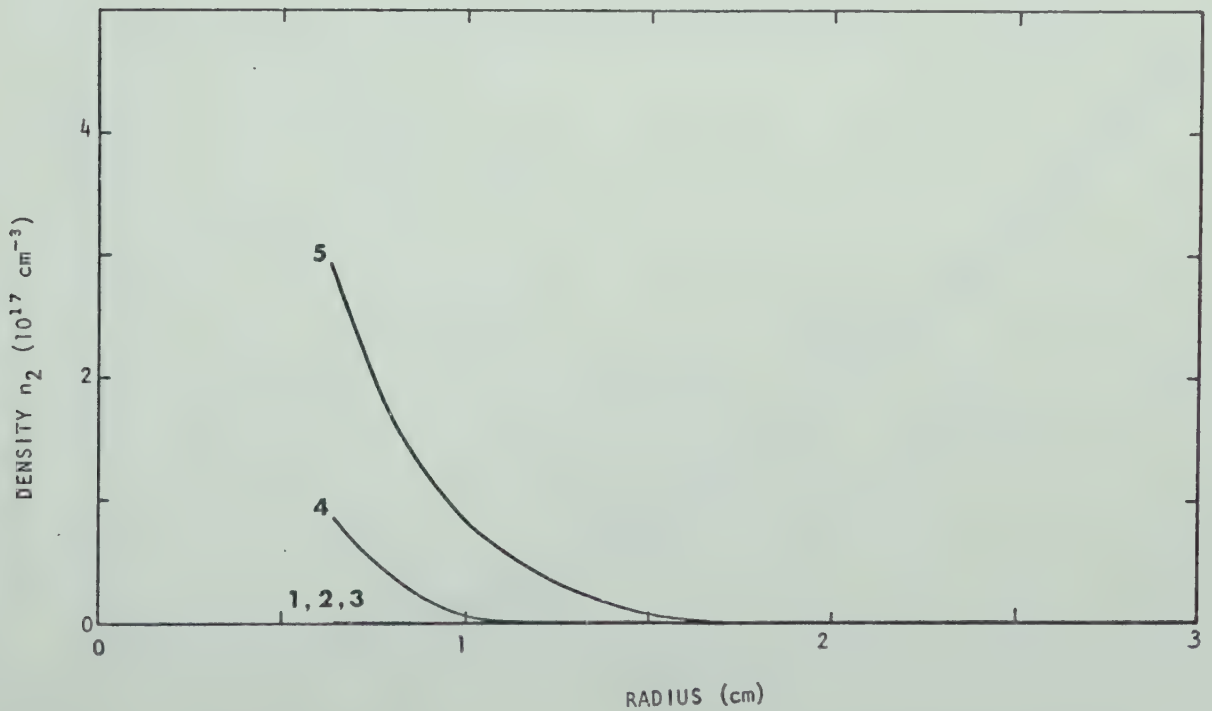


Fig.4.9 Calculated number density  $n_2 = n_{\text{He}^{++}}$  versus radius;quasi-one-dimensional model.  
See also Fig.4.5



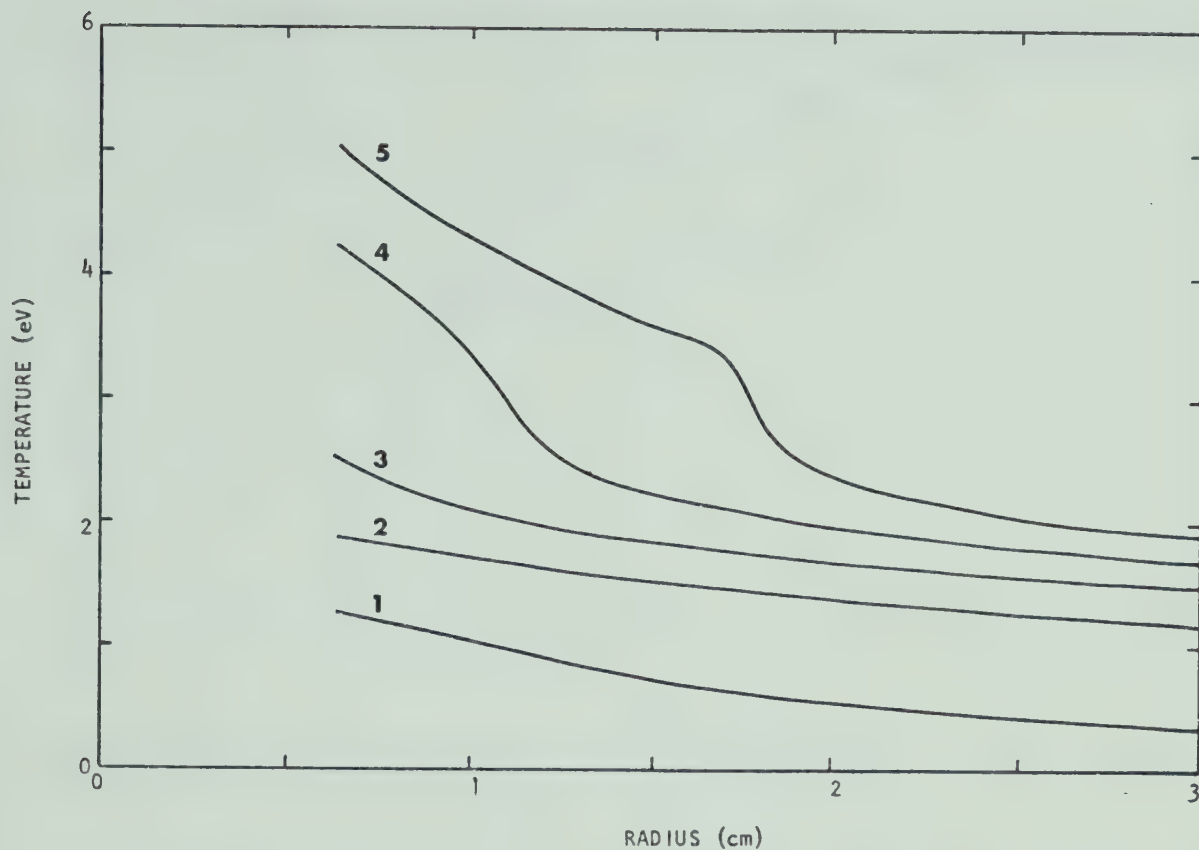


Fig.4.10 Calculated equilibrium temperature  $T$  versus radius; quasi-one-dimensional model. See also Fig.4.5

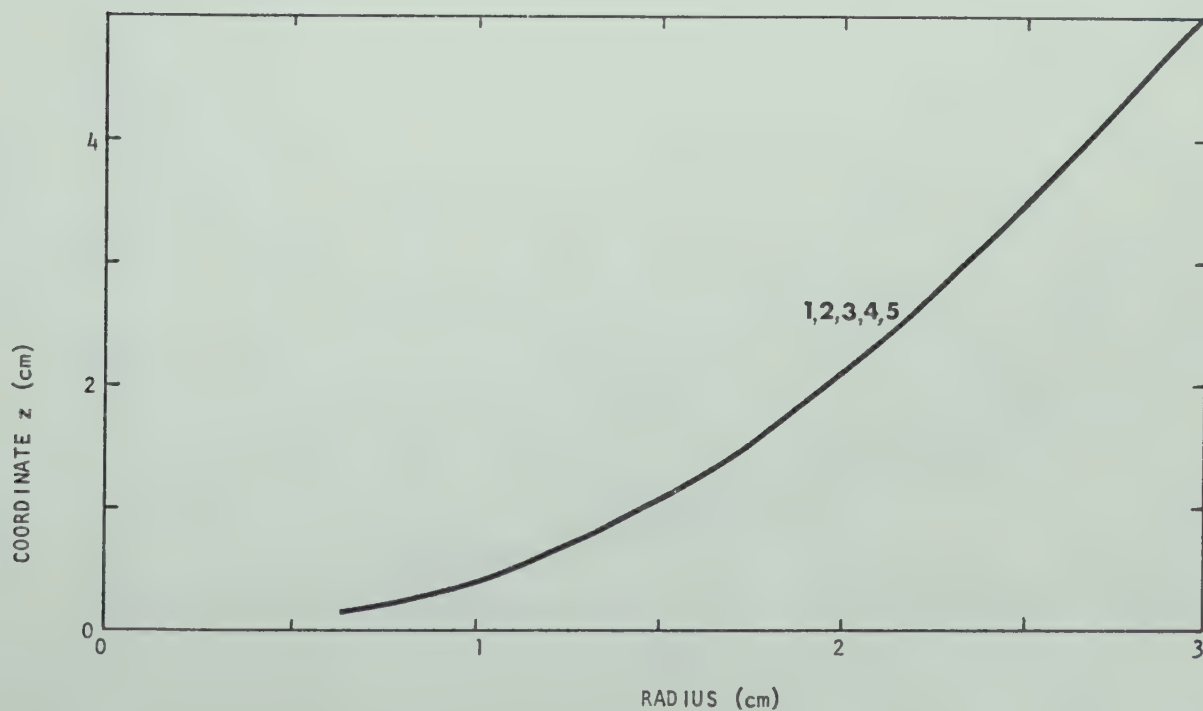


Fig.4.11 Calculated  $z$  coordinate of the middle of the shocked layer versus radius; quasi-one-dimensional model. See also Fig.4.5



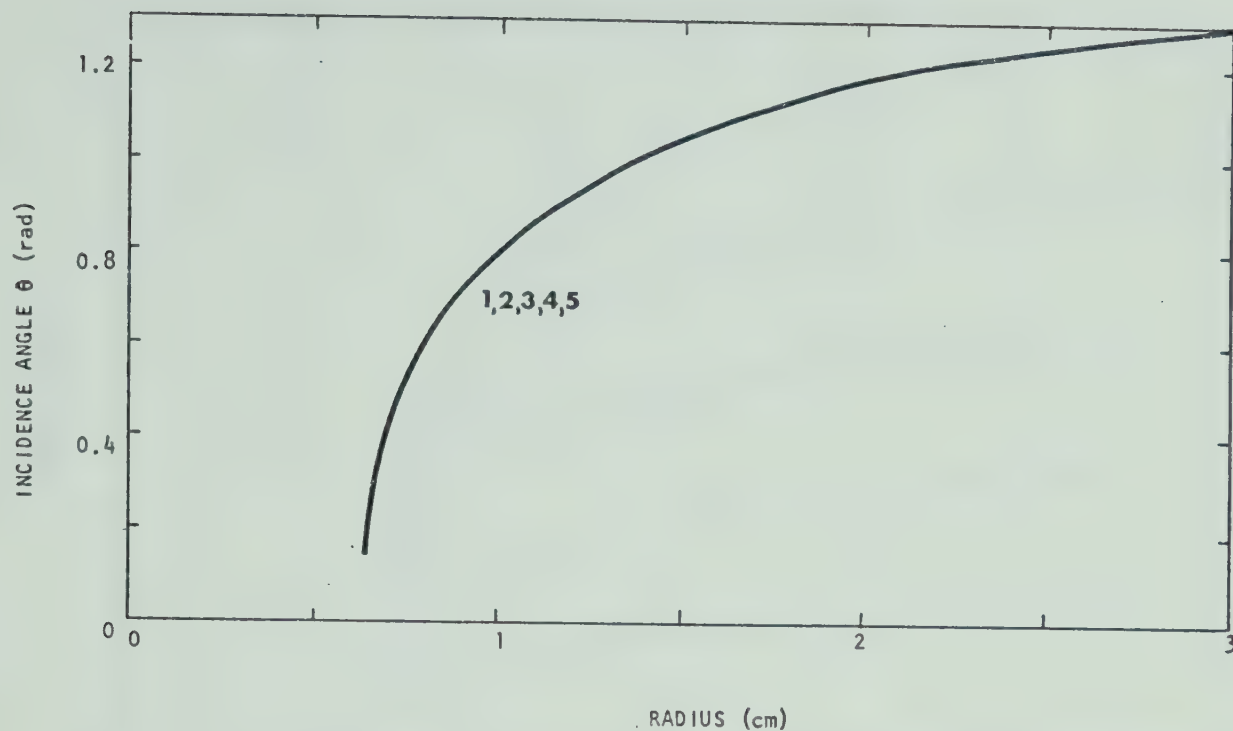


Fig.4.12 Calculated incidence angle  $\theta$  of the middle of the shocked layer versus radius; quasi-one-dimensional model. See also Fig.4.5

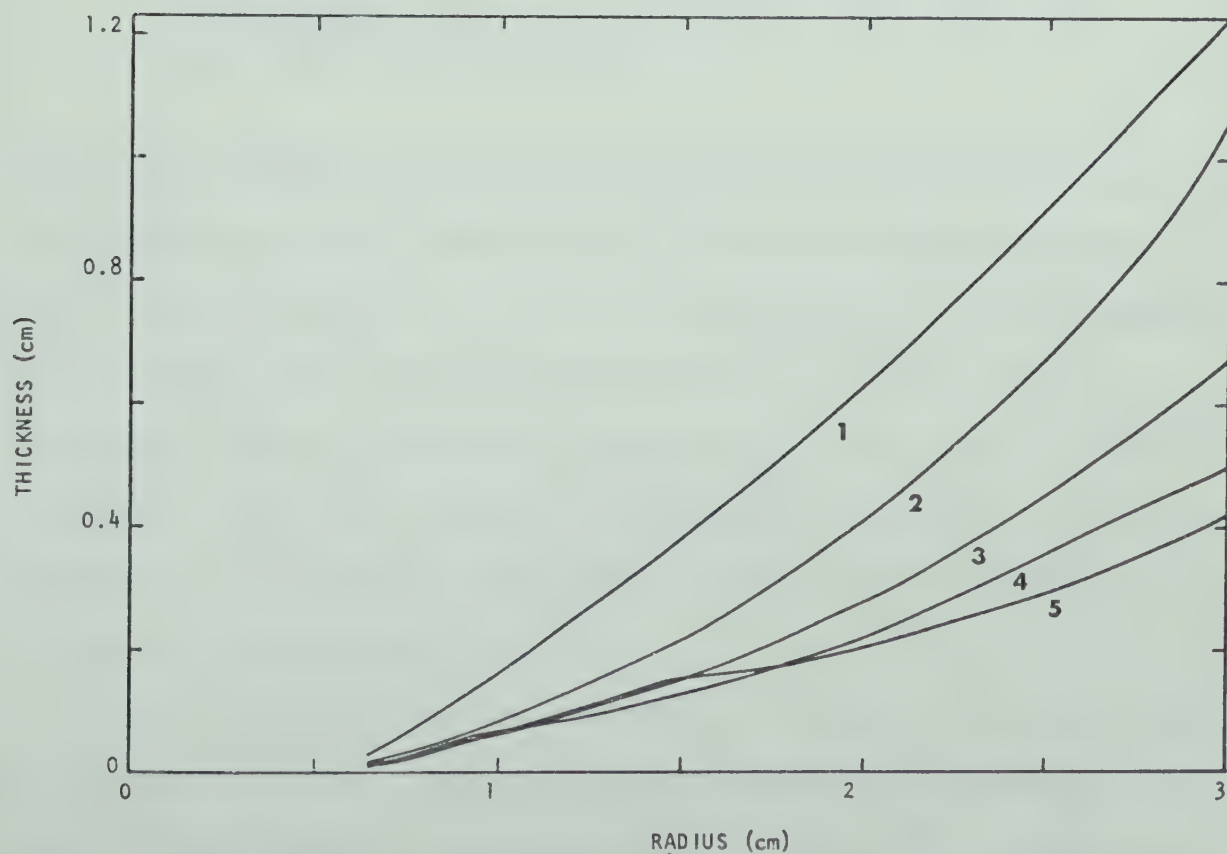


Fig.4.13 Calculated shocked layer thickness versus radius; quasi-one-dimensional model. See also Fig.4.5





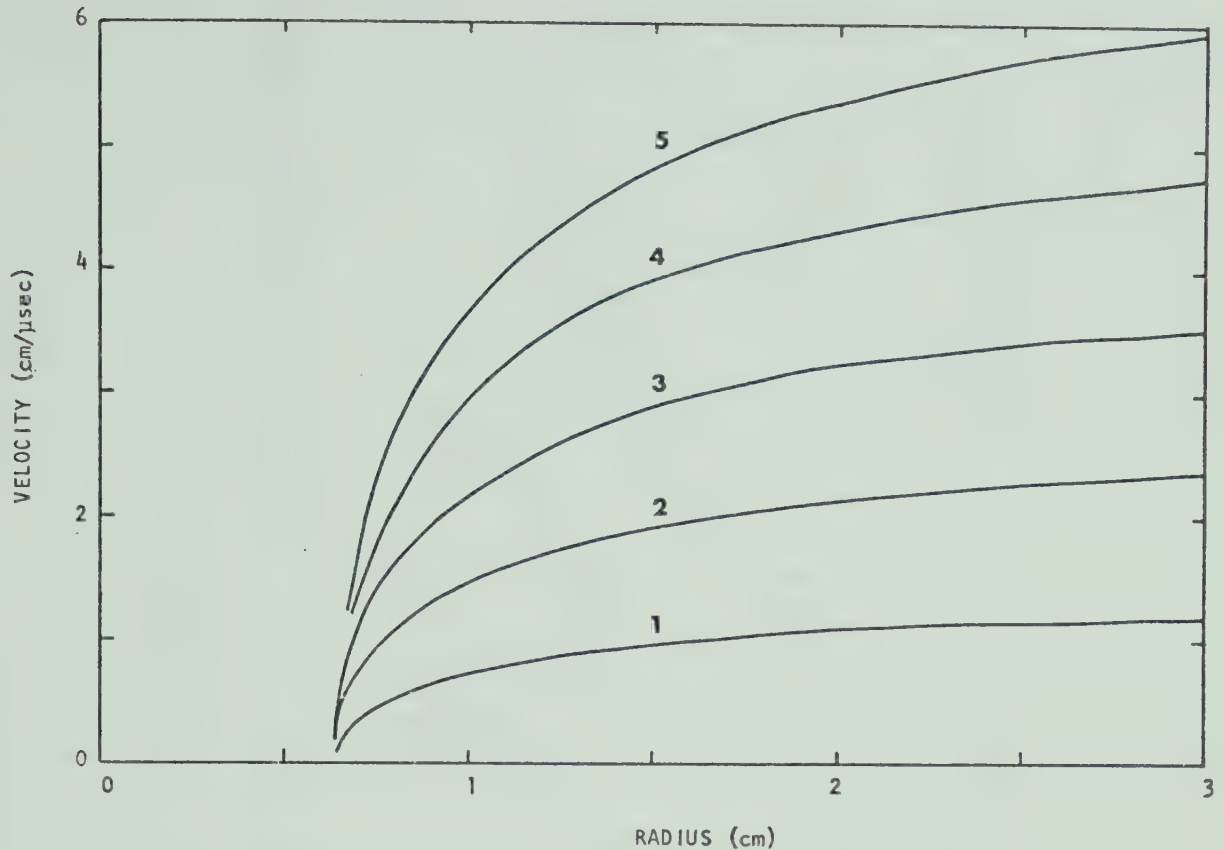


Fig.4.14 Calculated gas velocity along the current layer versus radius; quasi-one-dimensional model. See also Fig.4.5

of Lie *et al.* (1967). In this work the authors reported spectroscopic measurement of electron temperature and density for plasmas produced in a CPA filled with helium to a static pressure of .5 to 1 Torr. Luminous front velocities of  $\sim 6$  cm/ $\mu$ s were attained. Both spectroscopic measurements and our calculations depend on the local thermal equilibrium assumption. Lie *et al.* concluded, after careful discussion, that for the conditions of the experiment (and calculations) such an assumption is in fact a satisfactory approximation.

Figures 4.15 and 4.16 give comparison of the experimental data with the numerical solution. The experimental electron number density, for negative inner electrode, shows reasonable agreement with calculated  $n_e = n_1 + 2n_2$ . Note that the reported measurements were done with a plastic



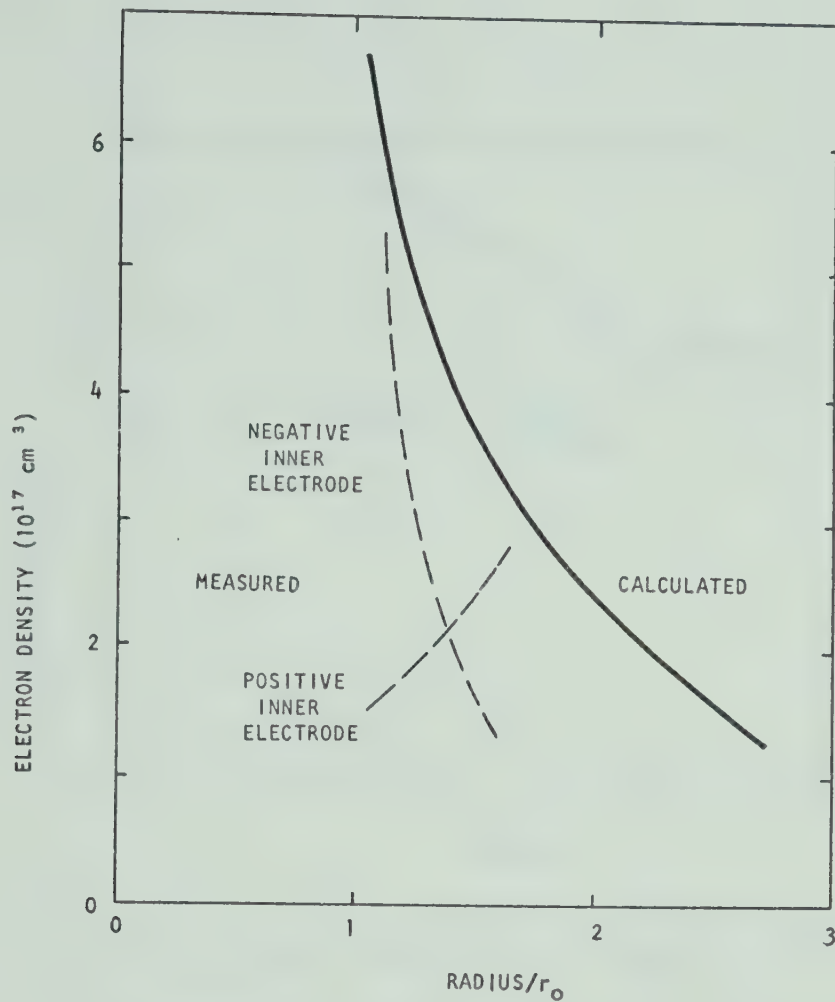


Fig.4.15 Calculated and experimental electron number densities;  $v_0 = 6 \text{ cm}/\mu\text{sec}$  ; experimental data of Lie *et al.* (1967).

(Acrylic) insulator and copper electrodes ( $r_{\text{inner}} = 1.5 \text{ cm}$ ,  $r_{\text{outer}} = 2.5 \text{ cm}$ ), and performed just behind the end of the outer electrode. The inner electrode was longer to prevent collapse of the sheet. This means that the electron density inside could be in even better agreement. The Calculated and measured equilibrium temperature, for negative inner electrode, are in excellent correlation. It is of interest that the comparison is done for velocity  $v_0 = 6 \text{ cm}/\mu\text{sec}$  where both degrees of ionization should be taken into account. There is no model in the available literature suitable for such a situation. The model of Pert (1969) requires some modifications and a numerical solution while the model of Butler *et al.*, (1969) gives only a very simplified ionization approximation.



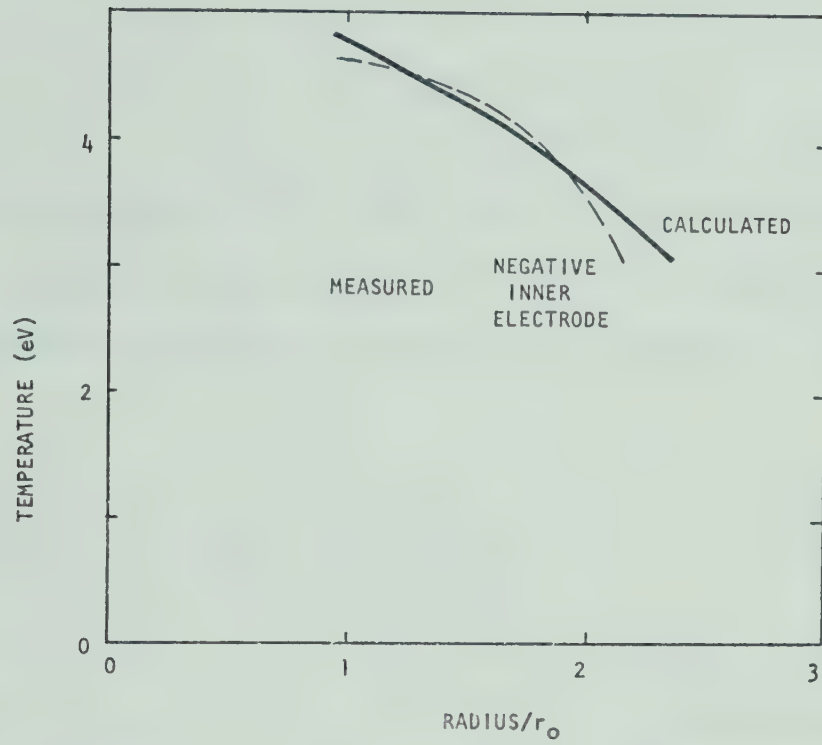


Fig.4.16 Calculated and experimental equilibrium temperature;  $v_0 = 6$  cm/ $\mu$ sec , experimental data of Lie et al.(1967).



## CHAPTER V APPARATUS

The experimental part of this study is devoted to an investigation of the acceleration regime of a CPA provided by a teflon insulator. A block diagram of the apparatus used for this study is in Fig. 5.1.

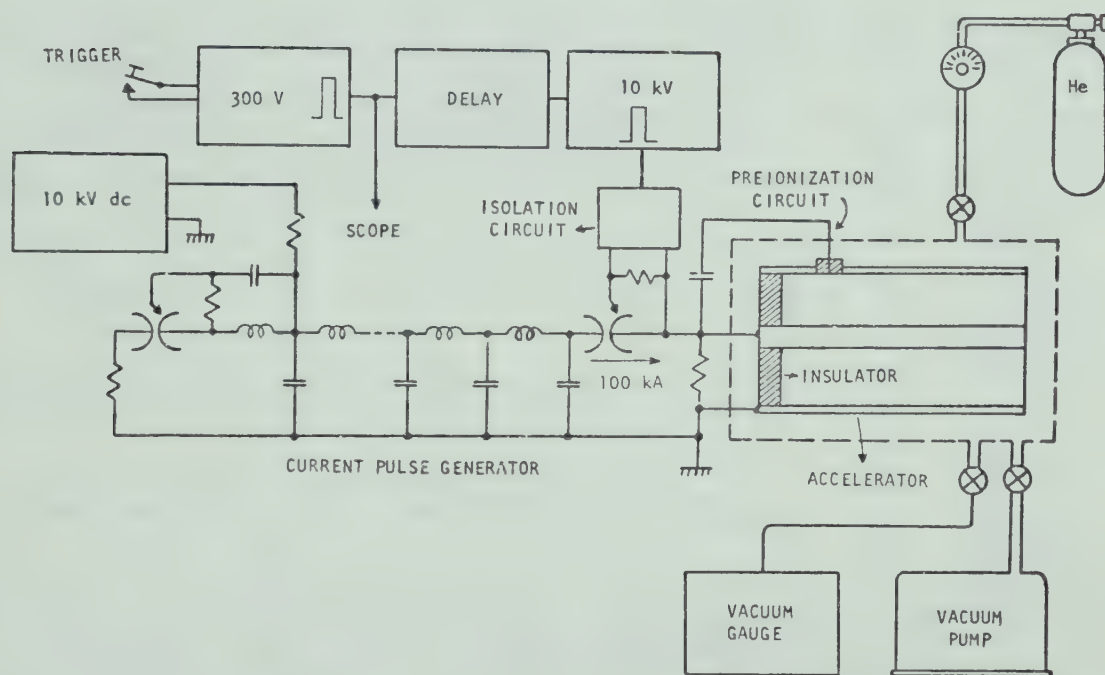


Fig.5.1 Schematic layout of the CPA apparatus.

Auxiliary devices are standard. Table 3 shows some details and parameters. Section 5.1 deals with the mechanical design of important parts of the apparatus.

Section 5.2 describes the design and operation of a current pulse forming network using two trigatrons for unipolar pulse generation. Only the first trigatron has external triggering. The resulting current

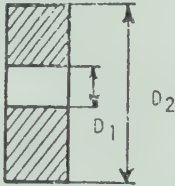
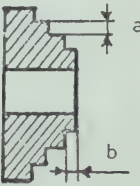




pulse is approximately 100 kA of 35  $\mu$ sec duration and has a shorter rise than fall-time. Calculated characteristics show good agreement with measured values.

Section 5.3 gives some details of diagnostics, infrared interferometry and luminosity, visible luminosity using photodiode, and magnetic probes.

Table 3 Description of the apparatus.

INNER ELECTRODE	COPPER, OUTER DIAMETER = 1.58 cm LENGTH = 60 cm	Fig.5.3
OUTER ELECTRODE	COPPER, INNER DIAMETER = 5.0 cm LENGTH = 60 cm	Fig.5.3
INSULATOR I	TEFLON; $D_1 = 1.59$ cm , $D_2 = 4.99$ cm	
INSULATOR II	TEFLON; $a = 6$ mm , $b = 4.3$ mm	
BASE PRESSURE	$10^{-2}$ Torr, EDWARDS ROTARY PUMP ED 150	
STATIC GAS PRESSURE	HELIUM AT PRESSURE 0.1 TO 10 Torr	
PREIONIZATION	SPARKS OVER THREE AUXILIARY TEFLON SURFACES; CAPACITORS : $3 \times 10$ nF / 15 kV	Fig.5.1 Fig.6.1
CURRENT PULSE GENERATOR	UNIPOLAR; 100 kA , 35 $\mu$ sec TEN CAPACITORS; 14.5 $\mu$ F / 20 kV , 50 nH	Fig.5.1 Fig.5.4
POWER SUPPLY	0 TO 10 kV dc CHARGING TIME $\sim$ 30 sec	Fig.5.1
TRIGGERING CIRCUITRY	THYRATRON; 300 V PULSE GENERATOR 300 V DELAY UNITS 10 kV PULSE AMPLIFIER	Fig.5.1
SWITCHING ELEMENTS	TRIGATRON; 10 cm DELRON CHAMBER, AIR 1 atm 2.5 cm COPPER ELECTRODES 2 mm COPPER TRIG. PIN PLACED INSIDE ONE ELECTRODE	Fig.5.1 Fig.6.1



## 5.1 MECHANICAL DESIGN OF THE ACCELERATOR

Arrangement of the apparatus is illustrated in Fig. 5.2, and the accelerator electrodes are shown in Fig. 5.3. The first version, GUN 1 had an outer electrode made of brass which was "transparent" to particles rotating in a magnetic field and for diagnostics. However, because of poor breakdown characteristics a second, GUN 2, was designed. This version had windows on one side only and the mechanical stability was improved. Finally, the third version, GUN 3, had two windows, but on both sides, i.e., the outer electrode allowed active optical diagnostics (external light source). The pyrex-glass cross (Fig. 5.3) with plate-glass windows was placed in the same axial position. For infrared diagnostics a NaCl window replaced the plate-glass.

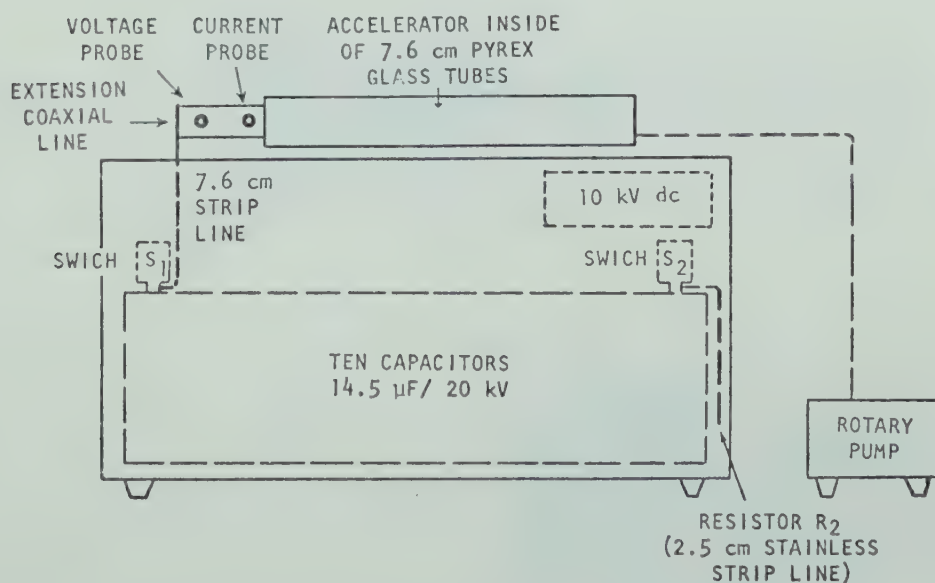


Fig.5.2 Sketch of the mechanical set-up. Notation according Fig.5.4



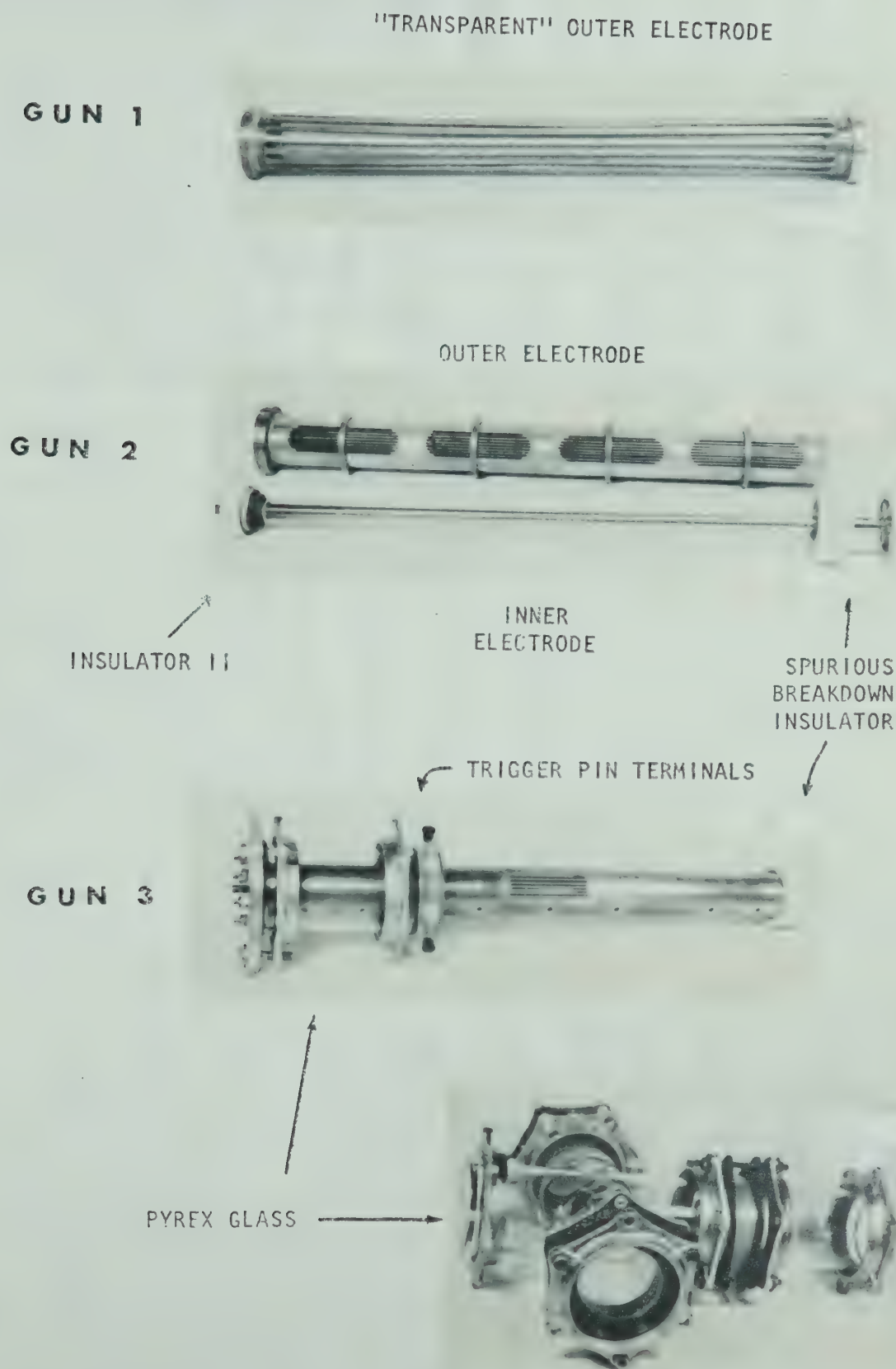


Fig.5.3 Three versions of the CPA.





## 5.2 ELECTRICAL DESIGN OF THE ACCELERATOR

For these studies a plasma accelerator with long electrodes is required, i.e., a high current (100 kA) pulse generator with known rise-time, long duration, unipolar behaviour and fall-time greater than rise-time. Unipolarity is important for creating only one current sheet per shot which avoids interaction between sheets. In addition, observation of electrode erosion is considerably simplified (Section 7.1) and one has the possibility of performing integrated spectral measurements.

Such a long unipolar current pulse has been generated by means of a charged LC delay line and three switches. This type of device, providing currents of a few kiloamperes, was built in CERN (Caris and Williams, 1969) for a different application. Each of the switches had a pulse generator for triggering and delay unit for time adjustment. For plasma accelerators, however, use of a matched delay line is complicated by the inductive character of the load (approximately few hundred nanohenries and few milliohms). The characteristic impedance  $Z_0$  of the delay line is of the order of 100 milliohms, which means that a matched delay line results in a considerably lower current.

A simple solution, for currents of a few amperes, can be obtained with a charged delay line approximately matched on the other end by a resistor in series with a reversed diode. This is not feasible, however, for high voltage (10 kV), high current (100 kA) applications as considered here. Another more complicated solution uses two sets of capacitors and switches (Mikoshiba *et al.* 1967), or one capacitor and time-varying resistance wire (Cheng, 1969).

The method discussed in this section is a mixture and extension of



the first and the third schemes mentioned (Jurak and Offenberger, 1972a). A charged delay line (ten capacitors) is discharged into the plasma accelerator and in the middle of the first half-wave a second switch is opened on the opposite side of the same line into approximately one half the characteristic impedance. This second switch is triggered by the wave generated on the active side of the line.

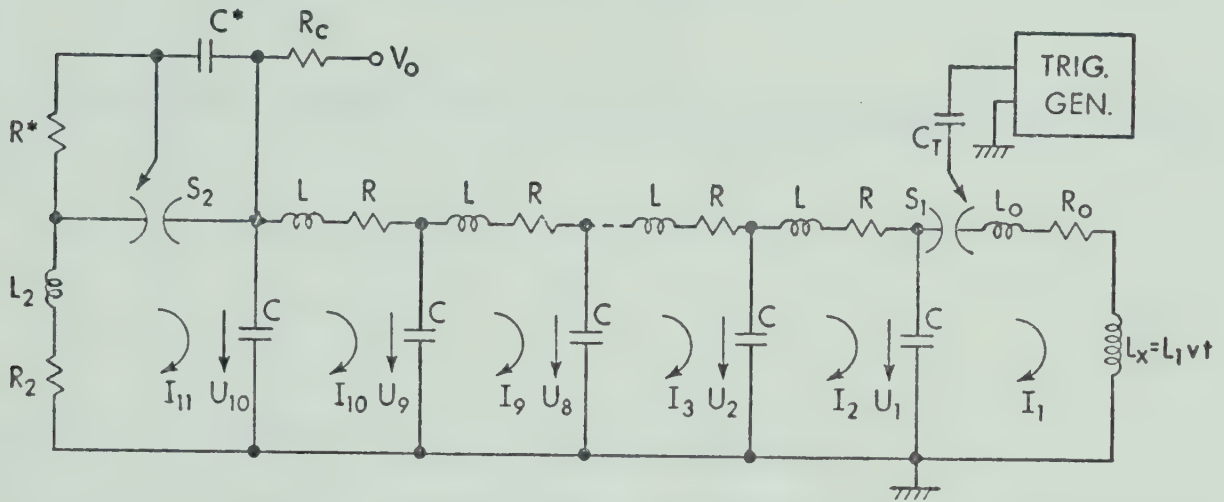


Fig.5.4 Circuit diagram of the pulse generator for a unipolar pulsed plasma accelerator. The plasma gun is approximated by an inductance  $L_x$ ;  $R^* = 1M\Omega$ ,  $C^* = 10$  nF,  $R_c = 10$  k $\Omega$ .

### 5.2.1 Circuit Analysis

Figure 5.4 shows a simplified diagram of the device. The circuit can be described by the following equations:

$$\dot{U}_\ell = (I_{\ell+1} - I_\ell)/C, \quad \ell = 1, \dots, 10$$

$$\dot{I}_1 = [U_1 - I_1(R_0 + L_1 v)]/(L_0 + L_1 v t)$$

$$\dot{I}_j = (U_j - U_{j-1} - I_j R)/L, \quad j = 2, \dots, 10 \quad (5.1)$$



$$i_{11} = \begin{cases} 0 & \text{for } t < t^* \\ (-U_{10} - I_{11} R_2)/L_2 & \text{for } t \geq t^* \end{cases}$$

and two relations:

$$t^* \approx 10. (LC)^{1/2}, \quad Z_0 \approx (L/C)^{1/2} \quad (5.2)$$

where the moving current sheet in the plasma accelerator is approximated by

$$L_x = L_1 v t \quad (5.3)$$

i.e., by an inductance varying linearly with time.

The first switch provides initial conditions of

$$U_\ell = V_0, \quad \ell = 1, \dots, 10$$

$$I_j = 0, \quad j = 1, \dots, 11 \quad (5.4)$$

and the second switch is simplified by means of the condition that the derivative of  $I_{11}$  is zero up to a time  $t^*$  (triggering time of the second switch).

### 5.2.2 Experimental Results

These equations were numerically integrated using the Runge-Kutta method, the results of which are shown in Fig. 5.5, for  $R_2 \gg Z_0$ . The



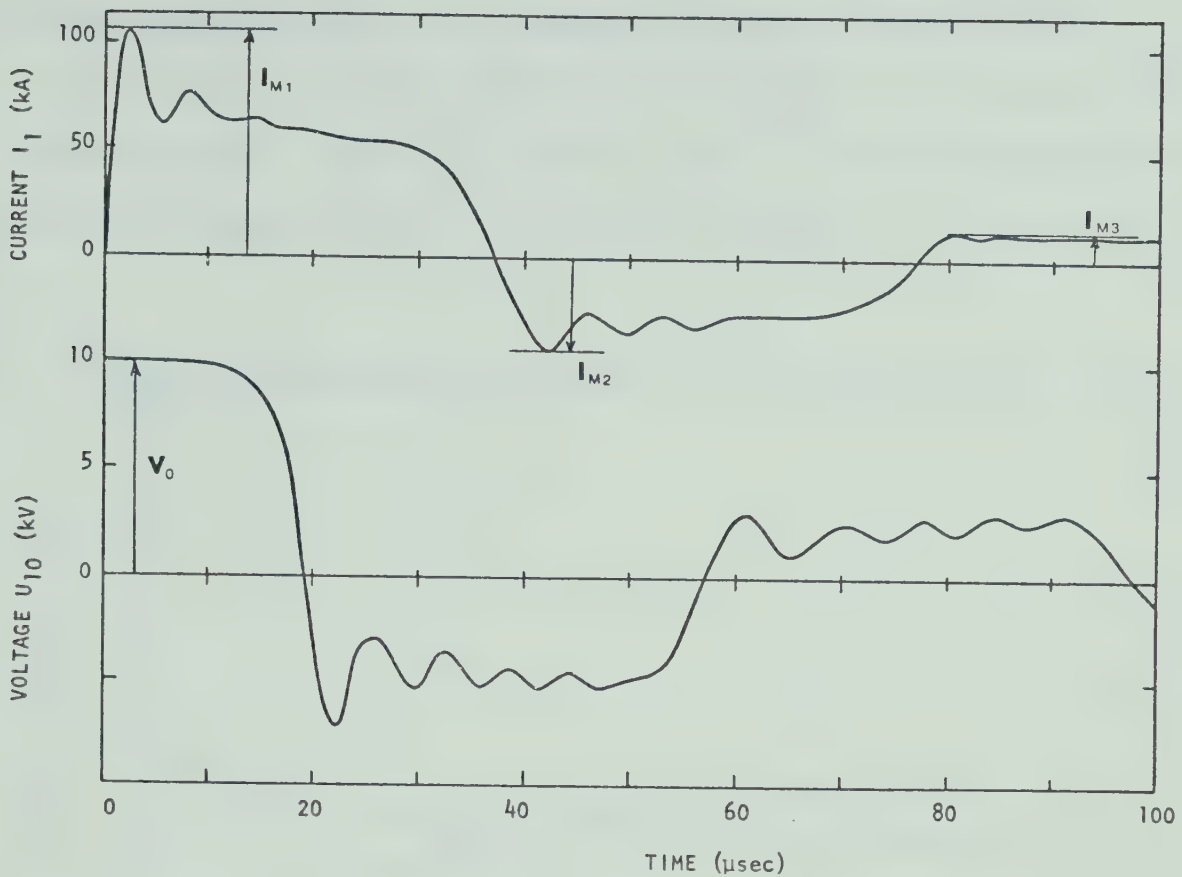


Fig.5.5 Calculated  $I_1$  and  $U_{10}$  for parameters  $L_1 v = 5.6 \text{ mH/sec}$ ,  $L = 196 \text{ nH}$ ,  $L_2 = 98 \text{ nH}$ ,  $L_0 = 111 \text{ nH}$ ,  $R = 8 \text{ m}\Omega$ ,  $R_2 \gg Z_0 = 118 \text{ m}\Omega$ ,  $C = 14.5 \text{ }\mu\text{F}$ ,  $V_0 = 10 \text{ kV}$  (in this case  $t^*$  has no influence on the results).

calculated current and voltage waveforms show good agreement with the experimentally measured waveforms of Figs. 5.7 and 5.8.

In addition, the dependence of currents  $I_{M1}$ ,  $I_{M2}$ ,  $I_{M3}$  on shorting impedance  $R_2$  is illustrated in Fig. 5.6, which shows that the ideal value of  $Z_0/R_2$  for optimum unipolar pulse generation is  $\approx 1.8$  for our given experimental parameters.

The experimentally observed current waveforms when a nearly correct value of  $Z_0/R_2$  was chosen are shown in Fig. 5.8. Though the discharge current waveform is not quite optimum, since the exact value of  $Z_0/R_2$  was not used, the result is nearly unipolar, which is adequate for some situations. A slightly different choice of parameters would have





provided better matching and consequently improved current pulse.

The results show in any event that the technique is simple and able to generate long unipolar high current pulses for plasma accelerators and can be easily modified for different applications.

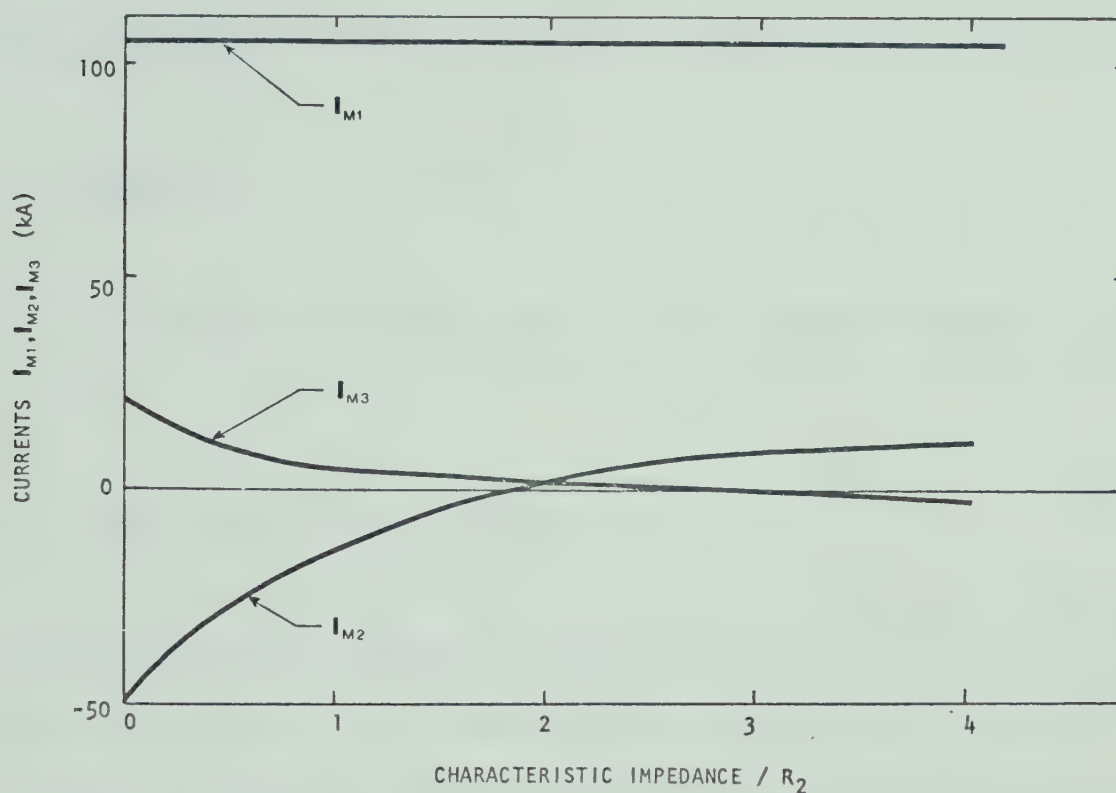


Fig.5.6 Variation of currents  $I_{M1}$ ,  $I_{M2}$ , and  $I_{M3}$  with  $Z_0/R_2$ , for experimental parameters as above. These currents are defined in Fig.5.5.

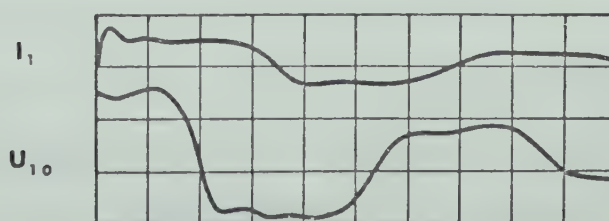


Fig.5.7 Oscilloscope of the current  $I_1$  and the voltage  $U_{10}$ ;  $R_2 \gg Z_0$ ,  $V_0 = +8$  kV,  $I_1$ : 100 kA/div,  $U_{10}$ : 5 kV/div, 10  $\mu$ sec/div.



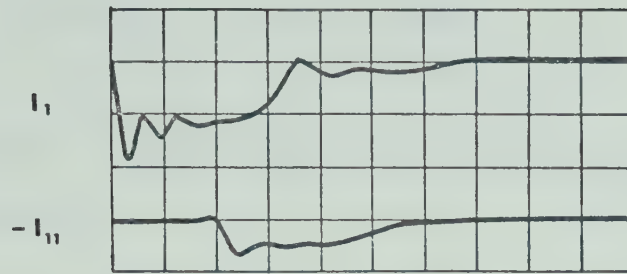


Fig.5.8 Oscillogram of the currents  $I_1$  and  $I_{11}$ ;  $R_2 \sim Z_0/1.8$ ,  $V_0 = -8$  kV,  $I_1: 50$  kA/div,  $I_{11}$  is not calibrated,  $10 \mu\text{sec/div}$ .

### 5.3 DIAGNOSTICS

This section describes the details of the diagnostic methods used in this study.

#### 5.3.1 Current and Voltage of the Discharge

Figure 5.9 shows a schematic of this measurement. The CPA is preceded by a 15 cm long coaxial line, where the high voltage probe (Tektronix P6015) has a special connector for safe and high frequency voltage pick-up. A Rogowski-coil, in classical toroidal form, is also built into the coaxial extension line. The signal from this coil is integrated to give a value proportional to the total discharge current.

Voltage is measured with a Tektronix probe. The current probe is calibrated by replacing the accelerator with a stainless steel strip-line resistor  $R$  of unknown value. One capacitor ( $C = 14.5 \mu\text{F}$ ) from the capacitor bank is used and charged to  $U_0 = 1$  kV and discharged into  $R$ . The voltage  $U_2$  (see Fig. 5.9) is proportional to the total current  $I$  which is given by



$$I = k U_2 = I_0 \exp(-t/T) \sin \omega t \quad (5.5)$$

where  $T = 2L/R$ ,  $\omega = (LC)^{-1/2}$ ,  $I_0 \approx U_0/\omega L$ . Determining the value of  $k$  is straightforward.

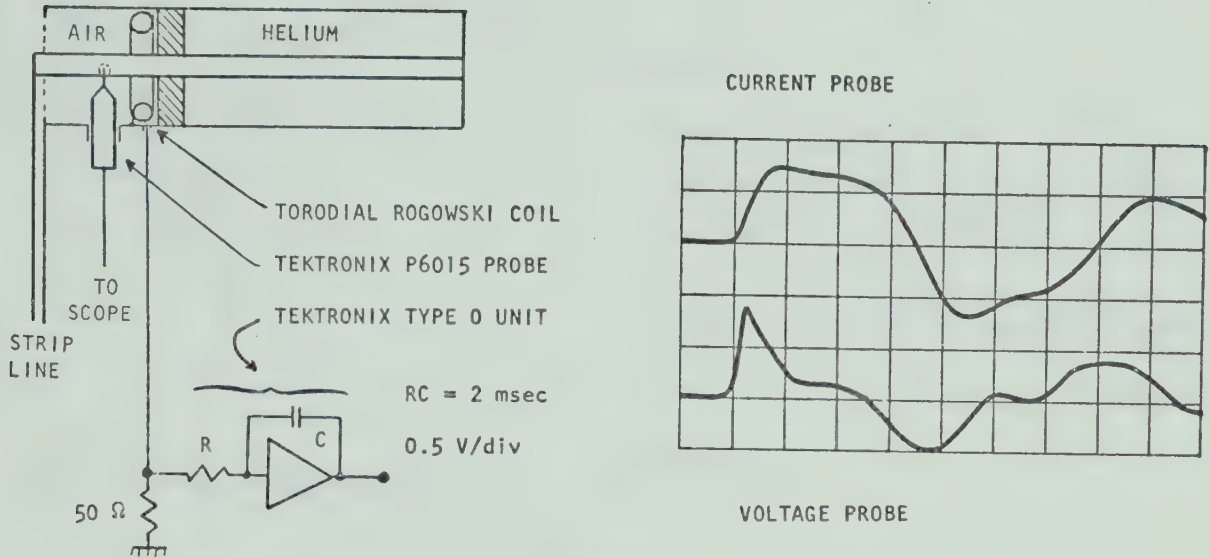


Fig.5.9 Schematic and typical oscillogram of the current and high-voltage probe. Five capacitors charged to 10 kV. Current: 50 kA/div, voltage: 2 kV/div. Horizontal scale: 5  $\mu$ sec/div. For the current probe calibration the accelerator was replaced by strip-line resistor and only one capacitor was used.

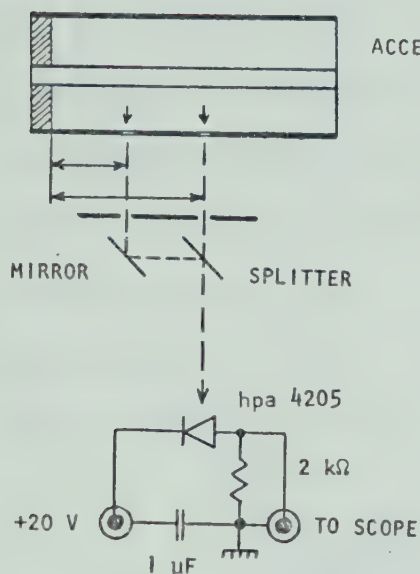
### 5.3.2 Luminous Front

The visible light from one spot to the inter-electrode gap is chosen by two distant iris diaphragms (3 mm diam) and picked-up by a semiconductor photo-diode (Fig. 5.10). Using different windows (holes) in the outer electrode, the diode axial position is changed for successive shots, and the resulting multiexposure of oscillograms (Fig. 5.10) gives the time development of the luminous front. This measurement yields high shot to shot reproducibility. Figure 5.11 illustrates modification of the previous method, where the latter assumption (reproducibility) is not required for

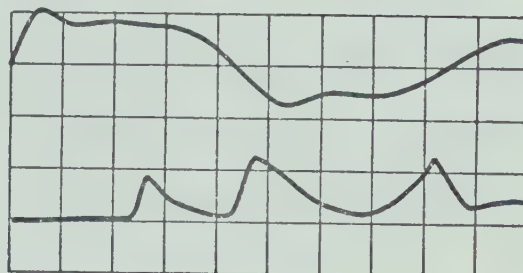


the velocity determination.

Using NaCl windows and a Ge:Au detector cooled by liquid nitrogen, we can also measure the infrared luminosity.

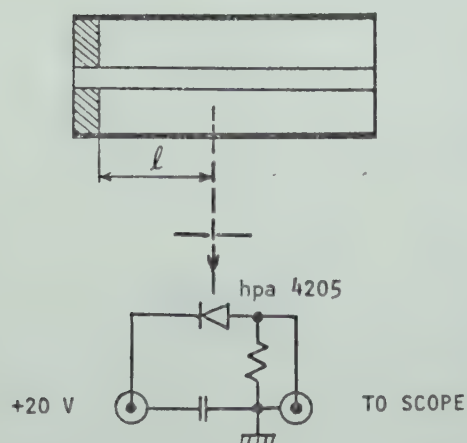


CURRENT PROBE



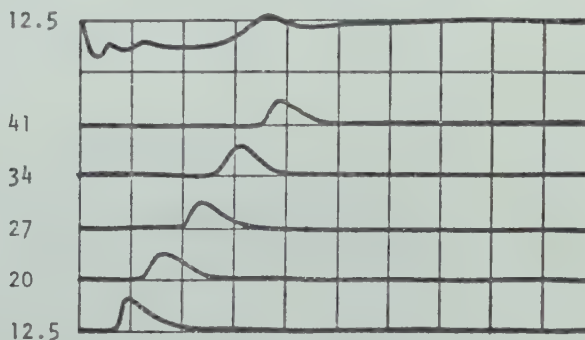
PHOTODIODE

Fig.5.10 Luminous layer position measurement; experimental set-up and typical oscillograms;  $V_0 = -10$  kV,  $I: 100$  kA/div, photodiode: 10 v/div, horizontal scale: 10 μsec/div. One photodiode and six exposures were used.



AXIAL POSITION (cm)

CURRENT PROBE



PHOTODIODE

Fig.5.11 Luminous layer velocity measurement; experimental set-up and typical oscillogram,  $I: 100$  kA/div, photodiode: 0.2 V/div, horizontal scale: 5 μsec/div.





### 5.3.3 Current Distribution

The velocity of the current front can be measured by one or more non-integrated magnetic probes (10 turns,  $1 \text{ mm}^2$  cross-section) placed in 4 mm pyrex-glass tubing (Fig. 5.12). The current distribution along the electrodes, or the current sheet profile, can be measured in the same way by using two opposite coils, 1 cm apart (Fig. 5.13). The latter version is sometimes called a differential magnetic probe and its theory is given by Belan *et al.* (1970). Note that even the classical magnetic probe is of interest for studying fast discharges. Pachner (1971) has recently completed a doctoral dissertation on this subject.

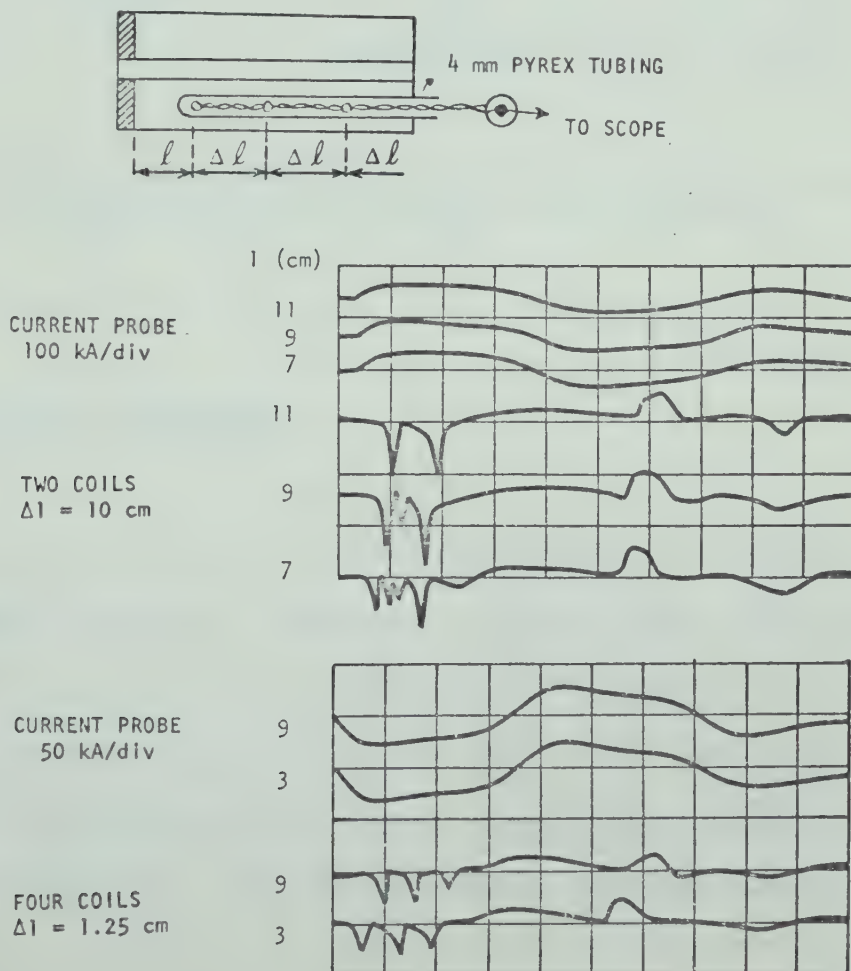
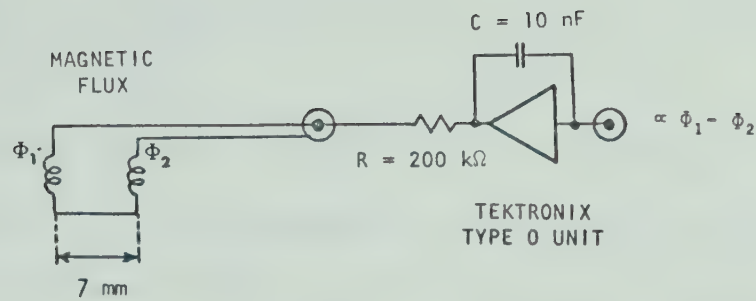


Fig.5.12 Current sheet velocity measurement; schematic and typical oscillograms for two and four coils nonintegrated magnetic probes (10 V/div); horizontal scale: 5  $\mu\text{sec/div}$ .





one coil: 10 turns, 1 mm diam

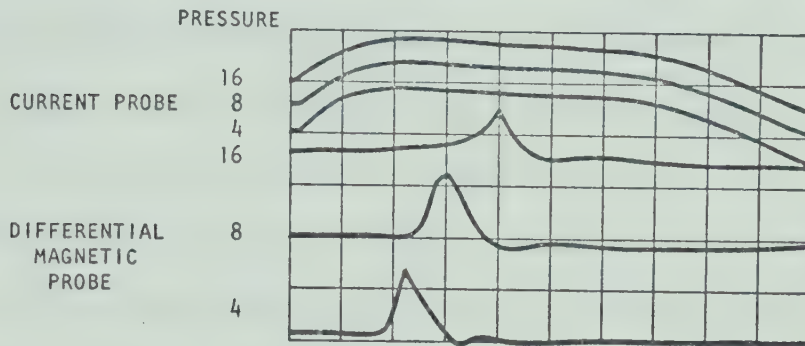


Fig.5.13 Schematic and typical oscillograms of the differential magnetic probe; I:100kA/div, magnetic probe:2 V/div, horizontal scale:2  $\mu\text{sec/div}$ , axial position:6 cm.

### 5.3.4 Infrared Diagnostics

Three types of infrared measurements will be discussed.  $\text{CO}_2$  LASER INTERFEROMETRY employs a Mach-Zehnder interferometer where the wavelength,  $\lambda$ , used is  $10.6 \mu\text{m}$ . The i r region requires special material for windows and beam splitters (usually NaCl and Ge). Since details are readily available for pulsed as well as c.w. measurements (Offenberger and Kerr, 1972 and Offenberger, Kerr and Smy, 1972), only pertinent relations are given.

The integrated optical path



$$\langle n_e \rangle = \int_0^{\ell} n_e(\ell) d\ell \quad (5.6)$$

to produce one fringe shift at  $\lambda = 10.6 \mu\text{m}$  is  $2.1 \times 10^{16} \text{ cm}^{-2}$ . A necessary condition for this measurement is that  $\omega$  of the radiation be greater than the plasma frequency  $\omega_p$ , i.e., the upper limit of electron density for  $\lambda = 10.6 \mu\text{m}$  is  $\text{cca}10^{19} \text{ cm}^{-3}$ .

The experimental arrangement is shown in Fig. 5.14. Splitters and windows are made of NaCl, and the mirrors are silvered-glass plates. An idealized output from the detector for a linear change in electron density  $n_e$  in time is illustrated in Fig. 5.15.

A schematic diagram of the nitrogen cooled Ge-Au detector is given in Fig. 5.16, where the cooled photoconductive detector has a nominal resistance of  $\approx 100 \text{ k}\Omega$ . Time response is limited mainly by stray capacitance since the intrinsic time constant is  $\approx 20 \text{ nsec}$ . The detector itself has a capacitance of  $10 \text{ pF}$ . The arrangement in Fig. 5.16 provides for three outputs with different source impedances. Here, the time response is limited by the connecting (coaxial) cable between output and oscilloscope.

Alignment of the interferometer requires that the narrow beams (diam  $\approx 3 \text{ mm}$ ) create beat signals on the oscilloscope, i.e., the small area of the detector ( $\approx 2 \text{ mm}^2$ ) has to pick-up only one fringe at a time.  $\text{CO}_2$  LASER ABSORPTION is based on  $10.6 \mu\text{m}$  radiation absorption via inverse bremsstrahlung (Offenberger and Kerr, 1972). The transmission  $T$  is related to the absorption coefficient  $\alpha$  by

$$T = \exp\left(-\int_0^{\ell} \alpha(\ell) d\ell\right) \quad (5.7)$$



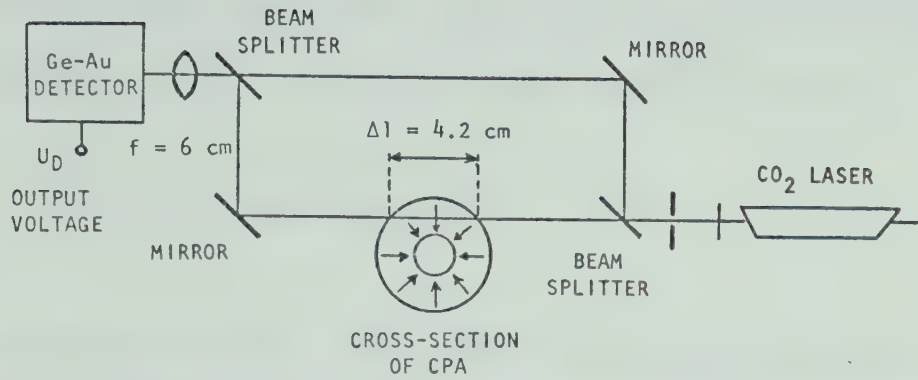


Fig.5.14 Mach-Zehnder interferometer arrangement.

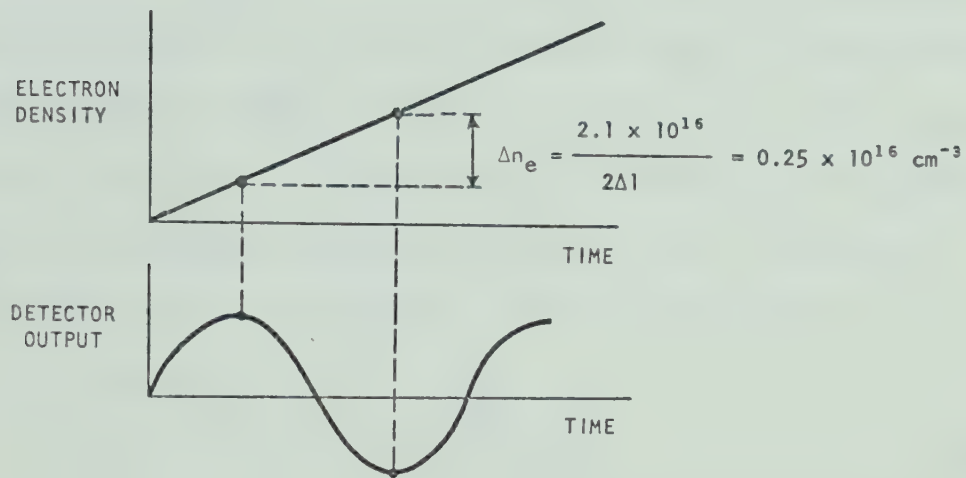


Fig.5.15 Evaluation of the interferogram for a linear electron density change and path  $\Delta l \sim 4.2$  cm. One fringe shift corresponds to  $2\Delta n_e$ .

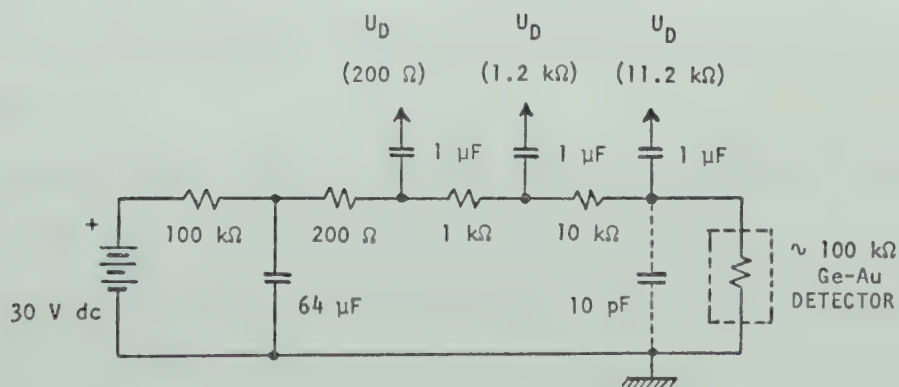


Fig.5.16 Schematic diagram of the Ge-Au detector.





where  $\lambda$  is the path length, and  $\alpha$  ( $\text{cm}^{-1}$ ) is related to the electron number density  $n_e$  ( $\text{cm}^{-3}$ ) and electron temperature  $T_e$  (eV) for  $\lambda = 10.6 \mu\text{m}$

$$\alpha = 1.8 \times 10^{-35} n_e T_e^{-3/2} \quad (5.8)$$

It has been assumed that  $h\nu \ll kT$ , where  $h\nu$  is the photon energy and  $kT$  is related to the mean thermal energy per particle. Note that for temperatures of a few eV, measurable absorption occurs for  $n_e \geq 5 \times 10^{16} \text{ cm}^{-3}$ . Optical components,  $\text{CO}_2$  laser, and detector are as in the previous method. BREMSSTRAHLUNG RADIATION EMISSION is a method opposite to the previous one (Managadze *et al.* 1968). According to theory, the emitted power,  $Qd\nu$  ( $\text{erg cm}^{-3} \text{ sec}^{-1}$ ) of ir bremsstrahlung radiation in a frequency interval  $d\nu$  is related to electron density  $n_e$  ( $\text{cm}^{-3}$ ), ion density  $n_i$  ( $\text{cm}^{-3}$ ), and electron temperature  $T_e$  ( $^{\circ}\text{K}$ ) by the relation

$$Qd\nu = 6.8 \times 10^{-38} z^2 g \frac{n_e n_i}{T_e} d\nu \quad (5.9)$$

where  $g$  is the Gaunt factor ( $\approx 3$ ) and  $z$  is the number of elementary charges of the ion. Again it is assumed that  $h\nu \ll kT$  and that the light has only a continuum spectrum in the region of interest (narrow ir filters are to be used).

This method can be used as an absolute (with necessary calibration) or relative measurement. For the relative measurements, the detector signal,  $U_D$ , resulting from radiation from volume  $\delta(\text{vol})$ , transmitted



through a filter with bandwidth  $\delta\nu$ , and assuming that  $n_e \approx n_i$ , is given by Eq. (5.9)

$$U_D = k n_e^2 T_e^{-1/2} \quad (5.10)$$

where  $k$  is a suitable scaling factor which can be evaluated on the basis of some other measurement (temperature calculated from plasma bulk electrical conductivity). Finally, assuming that  $n_e$  is already measured by some technique, by interferometry say, then

$$T_e = (k n_e^2 / U_D)^2 \quad (5.11)$$

This latter formulae will be used in Section 6.2.4.

### 5.3.5 Spot-Track-Pattern

The unipolar pulsed discharges leave spot track patterns on the surface of cathode and anode. Such pattern can be used as a source of information regarding discharge dynamics (Kvartskhava *et al.* 1966).

Investigation of these effects has the following steps:

- i) the accelerator is disassembled and the electrodes are polished,
- ii) the accelerator is assembled and fired  $n$ -times under the same conditions, and
- iii) then the gun is disassembled and enlarged pictures of the spot-tracks are taken.



A Graflec Camera and type 57 Polaroid film (5 x 4) are used for investigation of this effect as elaborated in Section 6.2.1 (Figs. 6.3.4 and 6.3.5).

Note that this method is very simple and cheap although rarely used.



## CHAPTER VI RESULTS OF THE MEASUREMENTS

A shock-tube model was formulated in Chapter 3, and its quasi-one-dimensional version solved numerically in Chapter 4. Reasonable agreement has been found between those calculations and detailed measurements of Lie *et al.* (1967). The aim of the experimental part was to perform measurements similar to Lie but make the comparison in more detail. During the course of the experimental work it has been found that the behaviour of our device is dominated by completely different mechanisms. Because investigation of these phenomena are of increased interest in current world-wide experimental effort, we decided to pursue these new aspects. The importance of this (insulator ablation) is given by the application of such devices as satellite thrusters and by the absence of a valid theoretical model.

Section 6.1 describes some details of the discharge-initiation regime in our device. Sections 6.2 and 6.3 are devoted to experiments with the CPA having two insulator geometries.

### 6.1 DISCHARGE-INITIATION REGIME

A general description of the discharge-initiation regime is given in Sections 2.1.1 and 2.2.1. For our arrangement, the "plasmoid" consists of the ionized ablated teflon, ionized helium, and ionized impurities from walls, gas, electrodes etc.





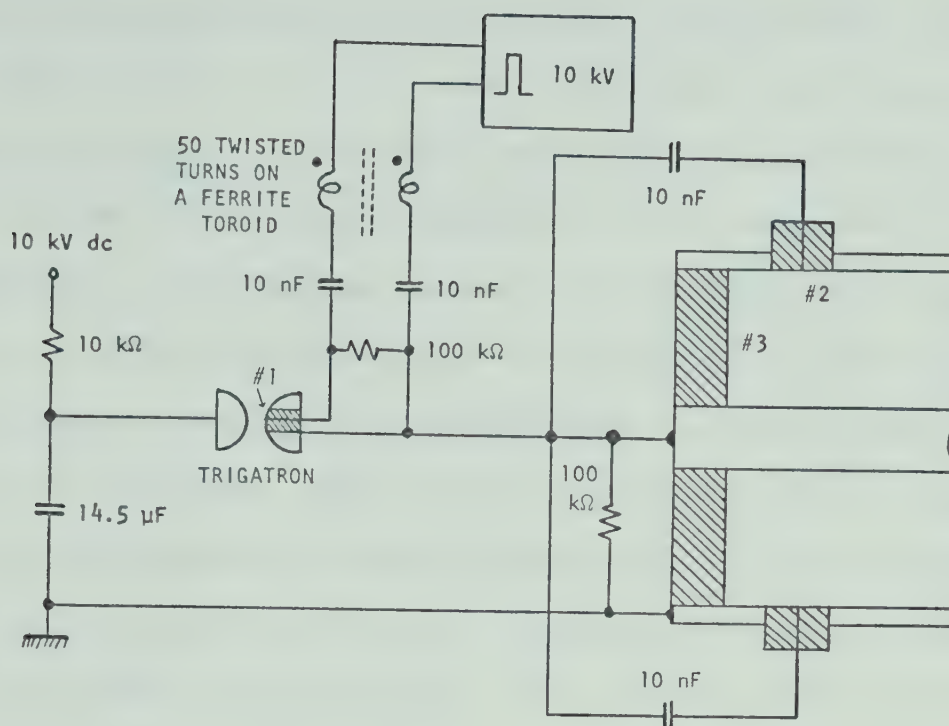


Fig.6.1 Schematic diagram of the apparatus for initial breakdown.

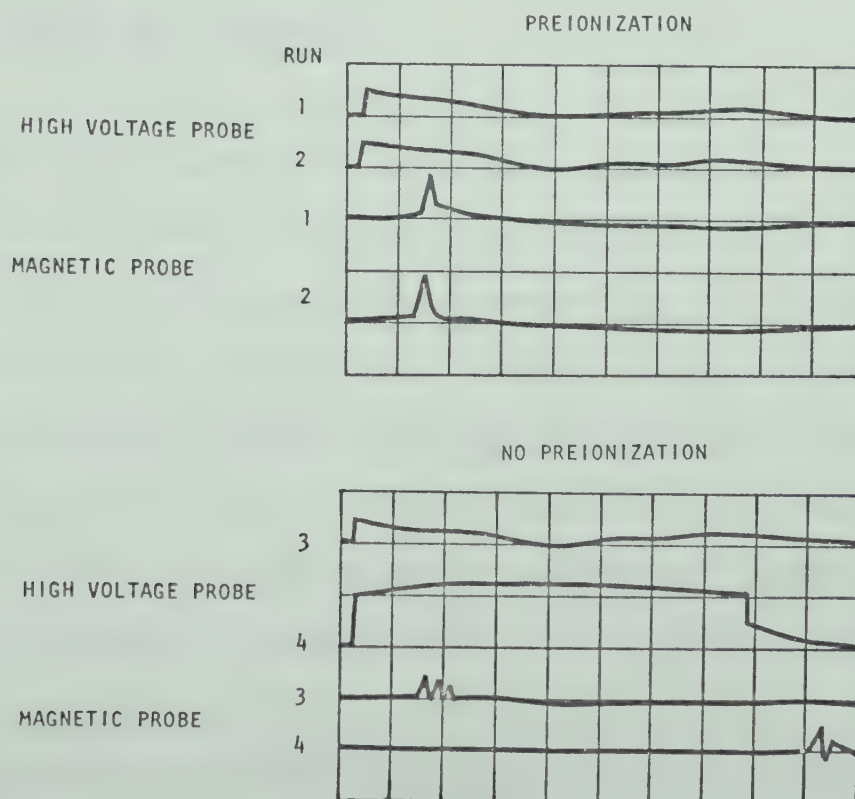


Fig.6.2 Verification of the preionization circuit; oscillograms of the HV-probe signals from four consecutive runs. HV: 2 kV/div, magnetic probe: 2 V/div, 1 μsec/div, axial location: 2 cm.



A simplified schematic of the apparatus, valid for the first microsecond is given in Fig. 6.1. One should mention the importance of the 100 k $\Omega$  resistors for this regime because they are connected in parallel to the teflon-surface-breakdown path and improve the jitter in breakdown time. The breakdown sequence is given by #1, #2, #3 as shown in Fig. 6.1. The original purpose of the trigger pins in the outer electrode was the creation of a current layer at this position. This, in fact, did not happen. Note that this unsuccessful effort is quite common for this particular problem (Popovic, 1969). On the other hand, Fig. 6.2 shows that the shot to shot reproducibility has been improved, even in our "poor" vacuum conditions. Many authors claim that high-purity gas conditions are required for good reproducibility (Pert, 1970b).

## 6.2 ACCELERATOR WITH INSULATOR I

Workman (1965) has treated analytically the insulator ablation model proposed by Keck (1964) and has shown that the ablation loss can be expressed with a single correlation parameter (see also Section 2.4). Lie (1970) also found a standing arc near the insulator surface (basic assumption of Workman's model), but after investigation the behaviour of the CPA having Vycor, Pyrex, Lucite, and Mylar insulators he concluded that further study was needed to develop a quantitative theory which combines the appropriate snow-plow model with the ablation model of Workman.

In the series of insulator types (glass→plastics), teflon is the most ablative material, but has not been systematically investigated. Such



detailed measurements are described in this Section.

### 6.2.1 Current Distribution

The slug and snow-plow models of the current sheet motion assume that the sheet is very narrow. Figure 6.3 shows the current distribution inside the CPA having Insulator I. Evidently completely different current distribution is obtained. The standing arc yields insulator ablation during the whole discharge time. Typical oscillograms of the differential magnetic probe and total current at an axial position of 22 cm are shown in Fig. 6.3.

From this oscillogram and others, taken at different axial positions we can calculate the current distribution along the electrodes for several different times. Results of such calculations are sketched in Fig. 6.4, where  $dI/dx$  is the current per unit length. The total current  $I$  is then given by

$$I = \int_0^{60 \text{ cm}} (dI/dx)dx \approx 70 \text{ kA} \quad (6.1)$$

The latter relation has been used for calibration of the differential magnetic probe.

Note that such a current distribution is completely dominated by the insulator ablation and only the term current front has any physical meaning. This type of behaviour has been reported by Belan *et al.* (1970) and Kalygin *et al.* (1971) but is "unknown" to most recent papers dealing



DIFFERENTIAL  
MAGNETIC  
PROBE

CURRENT PROBE

50 kA/div

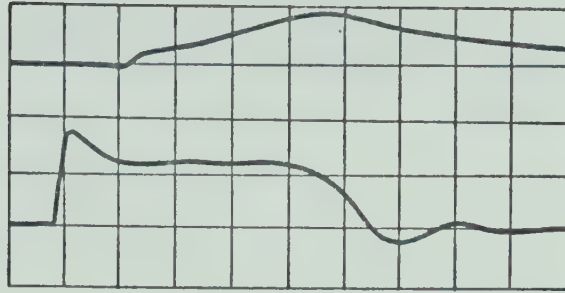


Fig.6.3 Current distribution for CPA with insulator I ; 5  $\mu\text{sec/div}$ ,  $V_0 = -10 \text{ kV}$ , axial position: 22 cm.

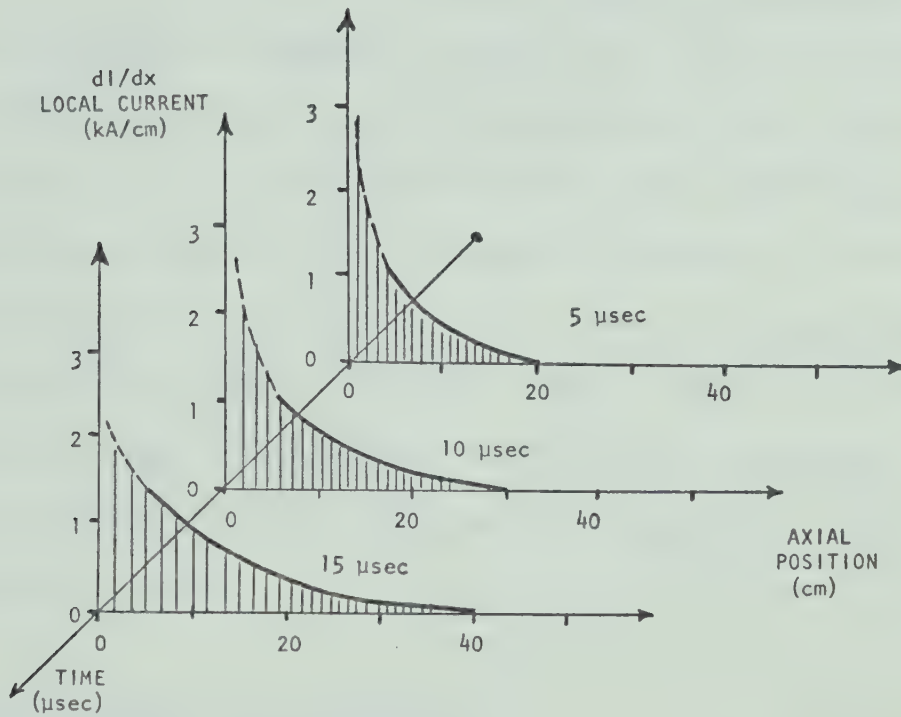


Fig.6.4 Typical time development of the discharge current inside CPA with Insulator I;  $P_0 = 1 \text{ Torr}$ .

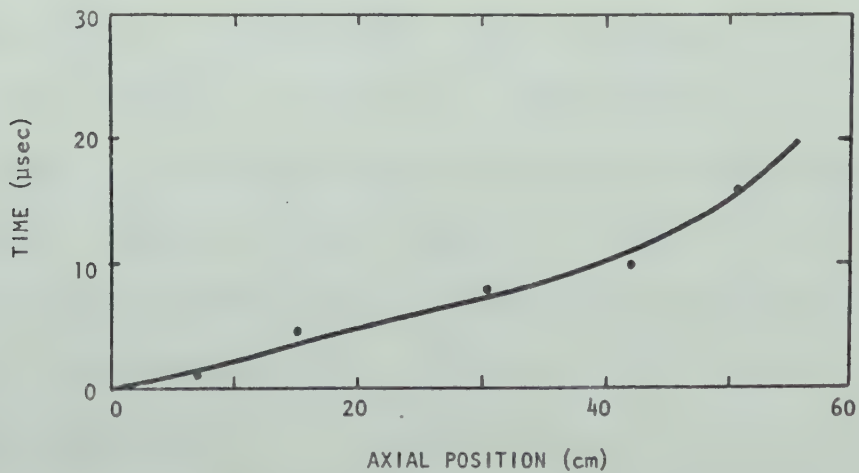


Fig.6.5 Current front position for CPA with Insulator I;  $p_0 = 0.02 \text{ to } 2.0 \text{ Torr}$ .





with the insulator ablation effect (Lie, 1970); Vondra *et al.* 1970). None of the latter has measured this "local current distribution" (Fig. 6.3).

### 6.2.2. Current-front Position

The velocity of the front of the distributed current can be easily measured by nonintegrated magnetic probes (Fig. 5.12), or assuming that this current front is identical with the luminosity front, one can use a photodiode (Fig. 5.10). The latter method has been used for the CPA having Insulator I and the result is shown as a function of time and pressure in Fig. 6.5. An important conclusion of this measurement is that a constant velocity of  $\approx 4$  cm/ $\mu$ sec does not depend on the helium pressure in the region .02 to 2 Torr and this can be explained simply by assuming that the insulator ablation process supplies a sufficient amount of working fluid.

### 6.2.3 Electron Density and Temperature

Electron density and temperature have been measured for CPA having Insulator I only using i r diagnostics. (Measurement of the case with Insulator II has an increased requirement for noise reduction and speed of detection). Figure 6.6 shows a typical oscillogram of the local current (diff-magnetic probe) and the fringe beats, measured with the Mach-Zehnder interferometer (Fig. 5.14) for  $\lambda = 10.6$   $\mu$ m and a plasma thickness  $\Delta l \approx 4.2$  cm.

The local currents can be calibrated by using Eq. (6.1). The electron density, calculated according to Fig. 5.15, is also shown in



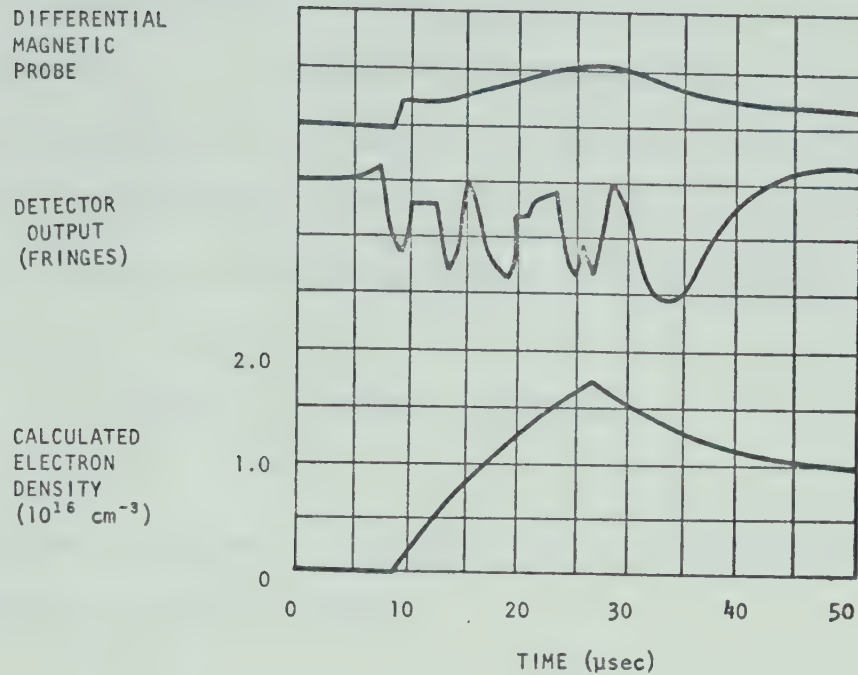


Fig.6.6 Typical traces of the local current and fringe beats and electron density (evaluated according Fig.5.15);  $p_0 = 1 \text{ Torr}$ ,  $V_0 = -10 \text{ kV}$ , axial position: 30 cm.

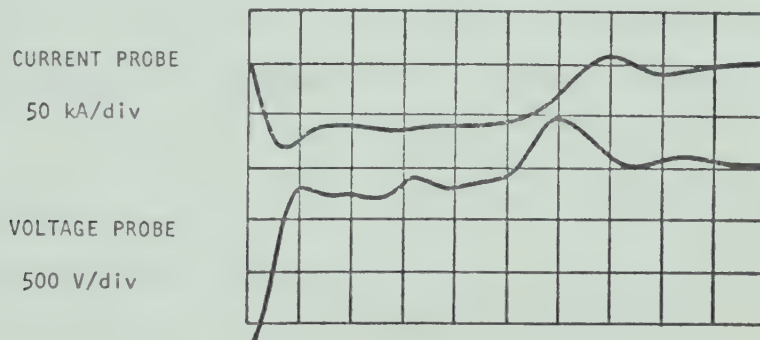


Fig.6.7 Current and voltage measurements;  $5 \mu\text{sec/div}$ ,  $V_0 = -10 \text{ kV}$ .

Fig. 6.6. This electron density has good time correlation with the local current measured at the same axial position.

The maximum average electron density is  $\approx 1.7 \times 10^{16} \text{ cm}^{-3}$  which is insufficient to produce measurable absorption (see Section 5.3.4). This conclusion was verified experimentally. The average (bulk) electron temperature can be evaluated from the average (bulk) electrical conductivity



$\sigma$ . For this purpose current and voltage oscillograms have been taken, and are shown in Fig. 6.7. From these oscillograms and Fig. 6.5, where the current front position  $x$  is shown we can calculate the bulk electrical conductivity in the middle layer of the CPA discharge. To approximately calculate the average conductivity for  $t = 10 \mu\text{sec}$ , read values

$$U \approx 200\text{V}, \quad I \approx 70 \text{ kA}, \quad x \approx 40 \text{ cm}$$

from which the calculated  $\sigma$  is  $\approx 1.5 \Omega^{-1} \text{ cm}^{-1}$ . Using Spitzer's relation for conductivity (Spitzer, 1968):

$$\sigma = \frac{T_e^{3/2}}{6.53 \times 10^3 \times \ln \Lambda} \quad (6.2)$$

where  $\ln \Lambda \approx 7.0$ ,  $\sigma$  is in  $\Omega^{-1} \text{ cm}^{-1}$ , and electron temperature  $T_e$  is in  $^\circ\text{K}$ . From Eq. (6.2) electron temperature at  $10 \mu\text{sec}$ , in the middle layer of CPA is

$$\langle T_e \rangle \approx 1.0 \times 10^3 \text{ } ^\circ\text{K} \quad (6.3)$$

which is an average value for a 40 cm long distributed current plasma.

The ir bremsstrahlung absorption is negligible but the emission is easily detectable. Figure 6.8 shows an oscillogram of the detected radiation and calculated electron temperature using Eq. (5.11) and where the scaling factor has been determined such that the averaged  $T_e$  should be equal to  $\langle T_e \rangle$  determined from the conductivity measurement. The resulting maximum temperature is  $\approx 0.6 \text{ eV}$  which is reasonable.



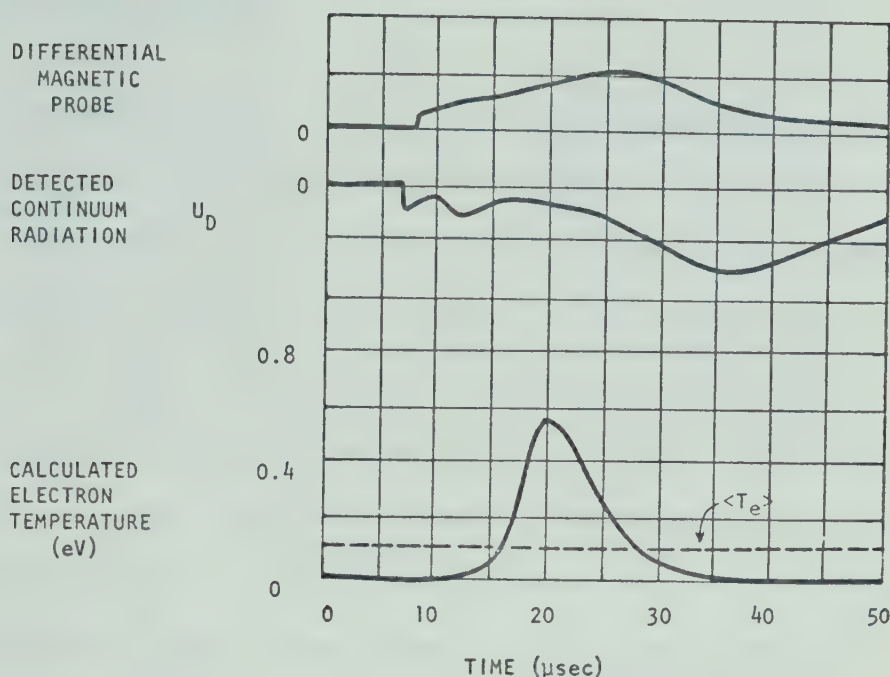


Fig.6.8 Oscillograms of local current, detected ir continuum radiation, and calculated electron temperature for known electron density (Fig.5.15) and known average temperature  $\langle T_e \rangle$ .

### 6.3. ACCELERATOR WITH INSULATOR II

The original aim of the experiments was to get a shock-tube behaviour, i.e., create a narrow current sheet. This can be approached by suppressing the standing arc at the insulator surface. Insulator II of Table 3 has such a suitable shape. Section 6.3 is devoted to the results of the experimental investigation of CPA having Insulator II.

One "old" but very effective method of investigation has been employed: the spot-track-pattern method, described in detail in Section 5.3.5 which is treated in Section 6.3.1. Only this simple static method has shown the geometry of the discharge-initiation regime, acceleration regime, and die-out (of the current sheet) regime.

Current distribution and current-front position are described in Sections 6.3.2 and 6.3.3. respectively.





### 6.3.1 Electrode Erosion

The electrode erosion mechanism is very important for the end-type PPA (Section 2.3.3), since the eroded material is the working medium. For coaxial and parallel-plate accelerators, however, this phenomenon is not desirable. Generally, for plasma accelerators having long electrodes and small inter-electrode gap, the plasma-metal interaction plays an important role. Tilt of the current sheet in a parallel-plate accelerator could possibly be explained in this way (Kvartskhava *et al.* 1967). For a CPA Having larger inter-electrode gap (our case), this phenomenon is over-ridden by the radial dependence of the magnetic pressure.

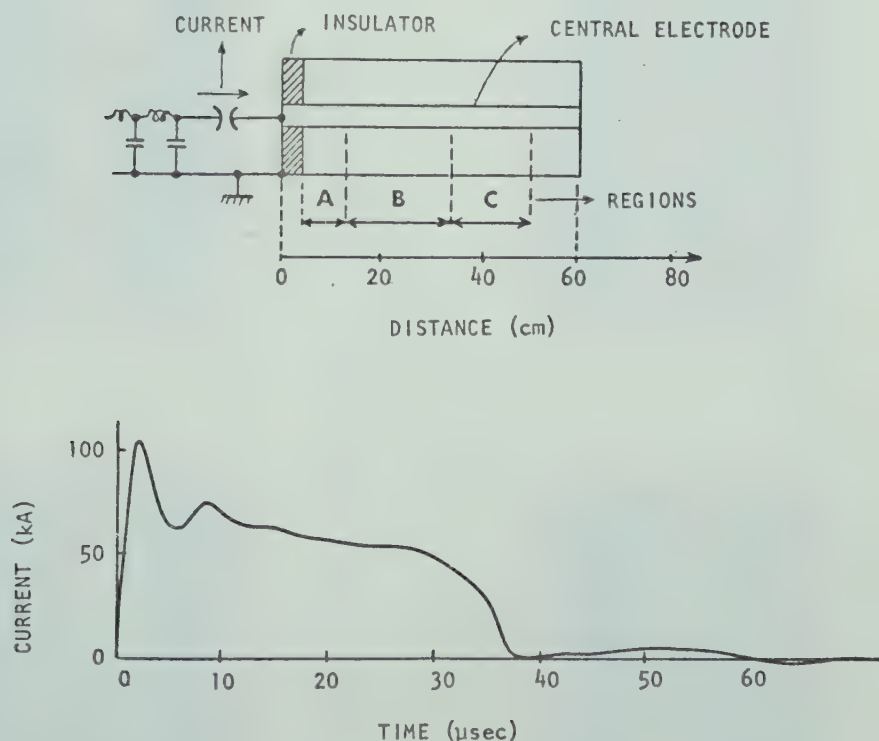


Fig.6.9 Region definition sketch for static photography of the spot-tracks on the central electrode (Fig.6.10) for  $p_0 = 0.6$  Torr; oscillogram of the discharge current for  $V_0 = 10$  kV. Region A corresponds to initial breakdown near the teflon insulator, region B to current sheet acceleration, and region C to stopping of the current sheet.



REGION A



REGION B



REGION C

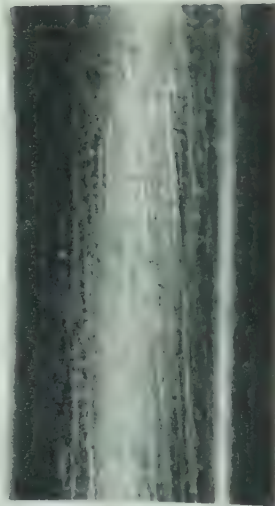


Fig.6.10 Photographs of anode-spot tracks on the central copper electrode(  $\times 3$  )after 20 discharges; $V_0 = +10$  kV, $p_0 = 0.6$  Torr.

REGION A



REGION B



REGION C

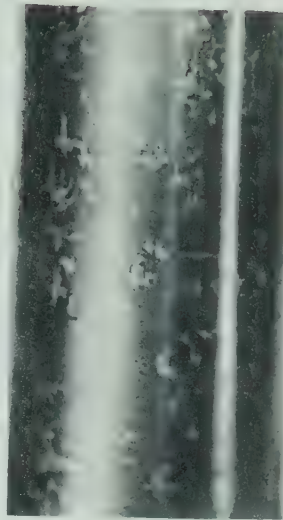


Fig.6.11 Photographs of cathode-spot-tracks of the central copper electrode(  $\times 3$  ) after 100 discharges; $V_0 = -10$  kV, $p_0 = 0.6$  Torr.



The moving discharge leaves certain characteristic spot-track-patterns. Assuming a unipolar current pulse generator is available, and "many" discharges are repeated, then the method described in Section 5.3.5 may be used.

This type of investigation has been performed for the CPA using Insulator II (see Table 3) and a static helium pressure of 0.6 T.

The anode-spot-track pattern developed on the positive electrode after 20 discharges, is shown in Fig. 6.10. This pattern features three typical regions along the electrode. The regions denoted A,B,C in Fig. 6.9, can be identified as:

- (A) initiation region,
- (B) acceleration region,
- (C) die-out region.

Note that Fig. 6.10 shows only a small part of each region. The shape of Insulator II is such that the standing arc near its surface is suppressed, i.e., region A shows the steady discharge before the acceleration could develop. Note that the trigger pins (Fig. 6.1), placed 6 cm from the insulator, have no influence on the region A position. The pattern of the middle region (B) shows that there is negligible anode erosion during acceleration. The pattern of the last region (C) proves that, under given conditions, the externally sustained plasma motion stops inside the gun (region C has deep anode spots of steady arc structure). The inertial-plasmoid motion could be expected to drive a shock wave.

The cathode-spot-track pattern, developed on the negative electrode after 100 discharges, is shown in Fig. 6.11, again for regions A,B, and C. The difference is in the shape of the individual anodic and cathodic spots. Note that acceleration region B has deep  $\sim 1$  cm long cathode-





tracks but almost invisible anode-tracks. The discontinuous form of these patterns has been known for a long time (Kvartskhava *et al.* 1966) and is in discrepancy with the usual "smooth" current sheet assumed in most available models.

### 6.3.2 Current Distribution

The technique used is the same as in Section 6.2.1. The CPA having Insulator II has narrower current sheet than that having Insulator I, but still it is not the required few millimeters thickness of the snow-plow models. Figure 6.12 shows measured local current distribution measured at a fixed axial position  $x = 10$  cm for helium pressures of 1, 2, and 4 Torr. Because the measured velocity is  $\approx 1$  cm/ $\mu$ sec for a pressure of 1 Torr (Section 6.3.3) then the layer thickness is roughly 2 cm.

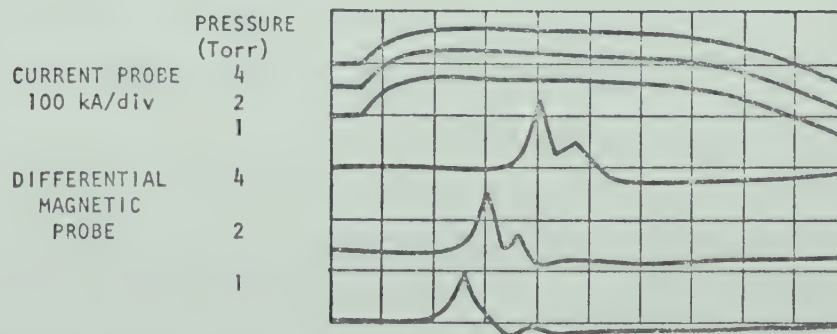


Fig.6.12 Current sheet distribution for CPA with Insulator II; 2  $\mu$ sec/cm,  $V_0 = +10$  kV.





### 6.3.3. Current front Position

The technique used for the front position determination is that illustrated in Fig. 5.10, i.e., the method uses one photodiode, two irises, and multiexposure of oscillograms. Results are in Fig. 6.13. In comparison to the CPA having Insulator I, these results show that gas pressure has a weak influence on the current front position, but the snow-plow velocities ( $\approx 6 \text{ cm}/\mu\text{sec}$ ) are still not reached.

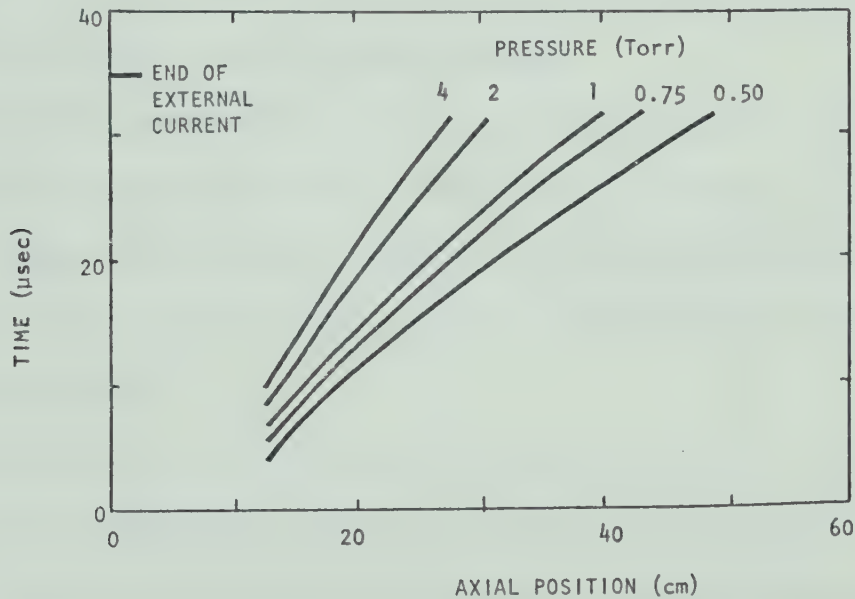


Fig.6.13 Current front position of CPA with Insulator II;  $V_0 = +10 \text{ kV}$ .



## CHAPTER VII RESUME AND CONCLUSIONS

Coaxial plasma accelerators have been described by introducing a set of regimes (kind of simple behaviour), regime models, and types (kind of accelerators). There is no such complete review available in the present literature.

A more detailed theoretical description was given to one type of formulation of the axisymmetric-steady-shock-tube regime, and two versions [ $Y(r,z)$  and  $Y(r,2(r))$ ] were developed.

The two-dimensional model,  $Y(r,z)$ , was approached in a very simplified version because of the complexity of the numerical methods involved. Verification of the resulting procedure was obtained but was found to be rather sophisticated, expensive, and parameter sensitive for the original purpose.

The quasi-one-dimensional model,  $Y(r,z(r))$ , leads to a simultaneous set of ordinary differential equations and nonlinear equations. Numerical procedures involved were found to be relatively simple and the solutions for helium (1 Torr, velocities 1 to 10 cm/ $\mu$ sec) was given. Comparison with available experimental data is reasonable.

Accelerators with two types of teflon insulator were investigated experimentally. The first type features a standing arc near its surface and the resulting acceleration regime is completely dominated by the insulator ablation process. Related velocities, electron densities and temperatures, and currents are measured. The second type of insulator



has a special shape for standing arc suppression and the related acceleration regime was found to be midway between the insulator-ablation and shock-tube regimes. The pure shock-tube regime has not been reached.

On the basis of this and other recent experimental work, the only available insulator ablation model (Workman, 1965) should be extended.

A unipolar current pulse generator (100 kA, 35  $\mu$ sec), developed for this study is of general applicability in pulsed plasma investigations.



## LIST OF REFERENCES

- AMSDEN, A.A. 1966. Los Alamos Report LA-3466.
- ARGYROPOULOS, G.S. and DEMETRIADES, S.T. 1969. J. Appl. Phys. 40, 4400.
- ARTMAN, J. 1963. Z. Physik 174, 376.
- ARTSIMOVICH, L.A. 1964. Controlled thermonuclear reactions (Gordon and Breach Science Publishers, New York).
- BECKER, E. 1968. Gas Dynamics (Academic Press, New York).
- BELAN, N.V., KIRIUSKO, V.I., MASHTYLEV, N.A. 1970. Sov. Phys.- Tech. Phys. 15, 118.
- BELOTSERKOVSKII O.M. (ed.) 1966. NASA TTF-453.
- BIRD, R.B. 1960. Transport phenomena (John Wiley, New York).
- BOSTICK, W.H., GRUNBERGER, L., NARDI, V., and PRIOR, W. 1969. Proc. 9th Intern. Conf. on Phenomena in Ionized Gases, 66.
- BOSTICK, W.H., PRIOR, W., and FARBER, E. 1965, Phys. Fluids 8, 745.
- BURTON, L.R. 1968. Phys. Fluids 11, 2284.
- BUTLER, T.D., HENIS, I., JAHODA, F.C., MARSHALL, J., and MORSE R.L. 1969. Phys. Fluids 12, 1904.
- CARIS, L. and WILLIAMS, E.M. 1969. CERN 69-13.
- CHANG, C.T. 1970. Nucl. Fusion - Special Suppl. 29.
- CHANG, C.T. and KOFOED-HANSEN, O. 1968. Plasma Phys. 10, 137.
- CHENG, D.Y. 1969. Rev. Sci. Instrum. 40, 1153.
- DRAWIN, H.W. 1971. in Reactions under plasma conditions, ed. Venugopalan, M. (New York: Wiley Interscience).
- FEARN, D.G. 1968. Phys. Letters 28A, 157.
- FUCKS, W. and ARTMAN, J. 1963. Z. Physik 172, 118.





- GENTRY, R.A. 1966. J. Comput. Phys. 1, 87.
- GREVILLE, T.N.E. 1969. Theory and applications of plane functions (Academic Press, New York).
- GRYZINSKI, M and NOWIKOWSKI, J. 1968. Nukleonika 13, 719.
- HAYES, W.D. and PROBSTEN, R.F. 1966. Hypersonic flow theory (Acad. Press, New York).
- HOFFMAN, A.L. 1967. J. Plasma Phys. 1, 193.
- HORTON, T.E. and MENARD, W.A. 1969. NASA-CR-99337.
- HOYAUX, M.F. 1968. Arc physics (Springer-Verlag, New York Inc.).
- ITT Co. 1969. Reference data for radio engineering. (Howard W. Sam and Co. Inc, New York).
- JAHN, R.G. and VON JASKOWSKY, W. 1968. Physics of electric propulsion (McGraw-Hill, New York).
- JURAK, K. and OFFENBERGER, A.A. 1972a, Rev. Sci. Instrum. 43, 48.  
 ----- 1972b, to be published, Phys. Fluids.
- JURAK, K., PERT, G.J., and CAPJACK, C.E. 1972. to be published, J. Comput. Phys.
- KALYGYN, A.E. and KOZLOV, N.P. 1971. Sov. Phys. - Tech. Phys. 15, 928.
- KECK, J.C. 1964. Phys. Fluids, 7, S16.
- KHIZHNYAK, N.A. 1970. Sov. Phys. - Tech. Phys. 14, 1534.
- KHIZHNYAK, N.A. Sov. Phys. - Tech. Phys. 15, 1828.
- KHIZHNYAK, N.A. and KALMYKOV, A.A. 1967. Sov. Phys. - Tech. Phys. 11, 1199.
- KOLESNIKOV, P.M. and STOLOVICH, N.N. 1970. Sov. Phys. - Tech. Phys. 15, 922.
- KULINSKI, S. 1966. Plasma Phys. 8, 493.
- KVARTSKHAVA, I.F. and KATVEEV, Y.V. 1966. Sov. Phys. - Tech. Phys. 11, 561.  
 ----- 1965. Nucl. Fusion 5, 181.



- LAPWORTH, K.C. 1969. J. Phys. A 2, 415.
- LIE, T.N. 1970. AIAA J. 8, 206.
- LIE, T.N., RHEE, M.J., MCLEAN, E.A. 1970. Phys. Fluids 13, 2492.
- LIE, T.N., ALI, A.W., MCLEAN, E.A. and KOLB, A.C. 1967. Phys. Fluids 10 1545.
- LOVEBERG, R.H. and GRIEM, H.R. 1971. Plasma Physics, Part B (Acad. Press, New York).
- LUBIN, M.J. 1966. Seventh Symposium on engineering aspects of magnetodynamics (McCosh Hall, Princeton).
- MANAGADZE, G.G. and PODGORNYYI, I.M. 1968 in Diagnostika plazmy (Atomizdat, Moscow).
- MIKHLIN, G.S. 1971. The numerical performance of variational methods (Wolters-Noordhoff).
- MIKOSHIBA, S. 1967. Rev. Sci. Instrum. 38, 1544.
- MORSE, T.F. 1962, Phys. Fluids 5, 596.
- MUNTENBRUCH, H. 1969. Phys. Fluids 12, 111.
- OFFENBERGER, A.A. and KERR, R.D. 1972. J. Appl. Phys. 43, 354.
- OFFENBERGER, A.A., KERR, R.D. and SMY, P.R. 1972. J. Appl. Phys. 43, 574.
- ORTEGA, J.M. and REINOLDT, W.C. 1970. Iterative solution of nonlinear equations in several variables (Acad. Pres, New York).
- PACHNER, J. 1971. Thesis. The Univ. of British Columbia.
- PERT, G.J. 1970a, J. Phys. A, 3, 421.
- , 1970b, Can. J. Phys. 48, 1769.
- , 1970c, Phys. Fluids 13, 2185.
- , 1970d, Can. J. Phys. 48, 1769.
- , 1969, J. Phys. D, 2, 429.



- , 1968, J. Phys. D, 1, 1487.
- POPOVIC, M. 1969. Danish AEC, Risö Report No. 206.
- RICHTMYER, R.D. 1967. Difference methods for initial-value problems  
(Interscience Publishers, New York).
- SADOWSKI, M. and SKLADNIK-SADOWSKA, E. 1968. Nukleonika 13, 257.
- SHARAH, A. 1969. Thesis, Carleton University.
- TAUSSIG, R.T. 1966. Phys. Fluids 9, 421.
- VAN TUYL, A.H. 1971. AIAA J. 9, 1431.
- VAN LEER, B. 1969. J. Comput. Phys. 3, 473.
- UTAH, R.D. Co., 1970. NASA-CR-108495.
- VALKOV, Y.A. and ZBRAILOVA, N.L. 1970. Sov. Phys. - Tech. Phys. 15, 599.
- VONDRA, R.J., THOMASSEN, K., and SOLBES, A. 1970. J. Spacecraft 7, 1402.
- WEYMAN, H.D. 1969. Phys. Fluids. 12, 1193.
- WORKMAN, J.B. 1965. Phys. Fluids 8, 2162.
- ZELDOVICH, Y.A. and RAIZER, Y.P. 1966 and 1967 (Vols. 1 and 2). Physics  
of shock waves and high temperature hydrodynamic phenomena (Acad.  
Press, New York).
- ZOLOTOTRUBOV, I.M. 1966. Sov. Phys. - Tech. Phys. 11, 766.
- , 1965, in Study of Plasmoids (Naukova Dumka, Kiev).

















**B30040**